Title
Crystallographic preferred orientation and deformation of deep Earth minerals

Author
Kaercher, Pamela Michelle

Publication Date
2014

Peer reviewed|Thesis/dissertation

Crystallographic preferred orientation and deformation of deep Earth minerals

by

Pamela Michelle Kaercher

A dissertation submitted in partial satisfaction of the

Requirements for the degree of

Doctor of Philosophy

in

Earth and Planetary Science

in the

GRADUATE DIVISION

of the

UNIVERSITY OF CALIFORNIA, BERKELEY

Committee in charge:
Professor Hans-Rudolf Wenk, Chair
Professor Burkhard Militzer
Professor Ronald Gronsky

Spring 2014

Crystallographic preferred orientation and deformation of deep Earth minerals

by

Pamela Michelle Kaercher

Abstract

Crystallographic preferred orientation and deformation of deep Earth minerals

by

Pamela Michelle Kaercher

Doctor of Philosophy in Earth and Planetary Science

University of California, Berkeley

Professor Hans-Rudolf Wenk, Chair

Large scale deformation in the Earth linked to mantle convection and plate tectonics causes plastic deformation of minerals in the lower crust and the mantle. During plastic deformation dislocation slip may occur, causing crystallographic planes to reorient. Observations of seismic anisotropy have been linked to crystallographic preferred orientation, but many questions and details remain unresolved.

Mineral physics aims to better constrain composition and evolution of the interior of the Earth with deformation experiments of Earth materials at high pressure and temperature. This thesis aims to provide further insight into crystallographic preferred orientation (CPO) and deformation mechanisms active at high pressure. Preferred orientation of iron-rich magnesiowustite (Mg,Fe)O, a major mantle mineral phase, stishovite (SiO_2), the high pressure polymorph of quartz that is likely present in the lower crust and mantle, and in $NaMgF_3$ + NaCl, an analog system to lower mantle minerals $MgSiO_3$ + MgO, have been examined with synchrotron X-ray diffraction while at high pressure in either a diamond anvil cell or a multianvil press.

Magnesiowüstite, $(Mg_{0.08}Fe_{0.88})O$, and wüstite, $Fe_{0.94}O$, were compressed up to 37 GPa at ambient temperature in diamond anvil cells (DAC) at the Advanced Light Source (ALS). X-ray diffraction patterns were taken *in situ* in radial geometry in order to study the evolution of CPO through the cubic-to-rhombohedral phase transition. Under uniaxial stress in the DAC, cubic texture developed (i.e. $\{100\}_c$ planes aligned perpendicular to the compression direction). Variant selection of preferred orientation was observed immediately following the transition to the rhombohedral phase. Specifically, the $\{100\}_c$ in cubic

became $\{01\bar{1}2\}_r$ in rhombohedral and remained aligned perpendicular to the compression direction. However, the $\{101\}_c$ and $\{111\}_c$ planes in the cubic phase split into $\{10\bar{1}4\}_r$ and $\{11\bar{2}0\}_r$, and $(0001)_r$ and $\{10\bar{1}1\}_r$, respectively, in the rhombohedral phase. The $\{11\bar{2}0\}_r$ planes preferentially aligned perpendicular to the compression direction while $\{10\bar{1}4\}_r$ oriented at a low angle to the compression direction. Similarly, $\{10\bar{1}1\}_r$ showed a slight preference to align more closely perpendicular to the compression direction than $(0001)_r$. This variant selection may occur because the $<10\bar{1}4>_r$ and $[0001]_r$ directions are the softer of the two sets of directions. The rhombohedral texture distortion may also be due to subsequent deformation. Indeed, polycrystal plasticity simulations indicate that for preferred $\{10\bar{1}4\}<1\bar{2}10>_r$ and $\{11\bar{2}0\}<\bar{1}101>_r$ slip and slightly less active $\{10\bar{1}1\}<\bar{1}2\bar{1}0>_r$ slip, the observed texture pattern can be obtained. Upon decompression in the DAC, FeO reverted back to cubic symmetry and the cubic texture reappeared, demonstrating that the transition is reversible and has texture memory.

The crystal structure of the high pressure SiO_2 polymorph stishovite has been studied in detail, but little is known about texture development during deformation, which provides information for understanding subduction of quartz-bearing crustal rocks into the mantle. Radial DAC experiments were done at the ALS and the Advanced Photon Source (APS) while collecting X-ray diffraction patterns in radial geometry to examine *in situ* development of CPO. Starting pressure in the sample chamber was still in the quartz stability field, and compression of quartz produced a weak texture, likely due to Dauphiné twinning. Following compression of quartz into the stishovite stability field, near 13-16 GPa, the sample was laser heated to activate kinetics and transition to stishovite. Stishovite nucleated with (001) planes preferentially aligned perpendicular to compression. Increased preferred orientation during further compression up to 38 GPa is attributed to slip. Slip systems responsible were inferred from visco-plastic self-consistent modeling and are most likely basal and pyramidal slip at experimental conditions.

While much is known about preferred orientation in single phase rocks, deformation of polyphase rocks is largely unexplored. Nearly all of the Earth is composed of polymineralic aggregates, including the lower mantle, which is of critical importance for understanding the geodynamic evolution of the planet. Geodynamic models predict large strains due to convection in the mantle, and polycrystal plasticity simulations suggest strong preferred orientation. However, these models ignore interaction among phases, which is important for the lower mantle, estimated to be composed of ~25% soft magnesiowüstite (Mg,Fe)O and ~70% harder Mg-perovskite ($MgSiO_3$). How much preferred orientation develops as a result of large strains in the lower mantle depends on the volume percent ratios and arrangement of the two phases. If grains of the softer

phase, MgO, become interconnected, they may act as a lubricant between grains of the harder phase, thereby absorbing most of the deformation. Alternatively, the soft phase may sit in pockets in between harder $MgSiO_3$ grains, and thus not be interconnected, leaving $MgSiO_3$ to bear the load. In the former case, MgO will control the deformation, and in the later, $MgSiO_3$, and the development of CPO in these two cases may greatly differ.

To study CPO development in a two-phase system, deformation experiments were performed in the deformation-DIA (D-DIA, DIA being shortening of "diamond") at the APS while collecting X-ray diffraction patterns *in situ*. While the D-DIA offers more control over deformation conditions and temperature and can deform larger samples, resulting in better counting statistics than for DAC samples, it cannot reach pressures beyond 12 GPa or temperatures higher than 2000K. Thus neighborite ($NaMgF_3$) and halite (NaCl), which have the same structures and relative strengths as mantle minerals silicate-magnesium pervoskite ($MgSiO_3$) and periclase (MgO) but deform more easily, were chosen as analogs. Information on grain structure and distribution before and after deformation was collected using X-ray microtomography, both at the APS and the ALS.

Results from D-DIA experiments show that when present in as little as 15%, the soft phase absorbs much of the deformation, greatly reducing CPO of the harder phase. Conversely, CPO in NaCl is highest for the sample with highest NaCl content. This suggests that CPO develops and evolves best in rocks largely composed of one mineral phase, and the presence of a second phase greatly hinders CPO, even at high strain, likely due to greater activity of deformation mechanisms which do not produce CPO. In addition, microtomography data shows that soft NaCl is largely connected and surrounds the harder grains of $NaMgF_3$. Deformation of $NaMgF_3$ and NaCl was simulated with both a self-consistent polycrystal plasticity model and with another polycrystal plasticity model which uses fast Fourier transform that takes into account interactions among grains and is better suited to study deformation in two-phase materials. Implications for the lower mantle are discussed.

To my parents, Peggy Knox and James Kaercher, and my brothers, Matt and Dan.

Table of Contents

Crystallographic notations

(hkl)	Miller indices for a crystallographic plane that intercepts the crystallographic axes $\boldsymbol{a}$, $\boldsymbol{b}$, and $\boldsymbol{c}$ at $\boldsymbol{a} = 1/h$, $\boldsymbol{b} = 1/k$, and $\boldsymbol{c} = 1/l$
$\{hkl\}$	the set of all crystallographic planes equivalent to (hkl) by symmetry
$[hkl]$	Miller indices for a crystallographic direction $h\boldsymbol{a} + k\boldsymbol{b} + l\boldsymbol{c}$ where $\boldsymbol{a}$, $\boldsymbol{b}$, and $\boldsymbol{c}$ are the crystallographic axes
$<hkl>$	set of crystallographic directions equivalent to $[hkl]$ by symmetry
$(hkl)[hkl]$	slip of dislocations in the (hkl) plane, propagating in the $[hkl]$ direction
$\overline{h}$	$-h$
$hkil$	indices used for hexagonal, trigonal, and rhombohedral crystals, which have a unique $\boldsymbol{c}$ axes and three equivalent axes, $\boldsymbol{a}_1$, $\boldsymbol{a}_2$, and $\boldsymbol{a}_3$, with $i = -(h+k)$

Acknowledgements

Foremost, I would like to thank my adviser Rudy Wenk for being supportive and pushing me when I needed it. Your energy and excitement for research are contagious, and you are a wonderful example of a research scientist and professor – you have accomplished SO much, yet are still humble. I am lucky to have had you for my adviser. I would also like to thank my secondary adviser, Burkhard Militzer, who gave me valuable experience with calculations and coding. I also learned a lot and had fun while GSIing for you for The Planets. Thank you also to committee members Professor Ronald Gronsky and Professor Paul Renne, both whom I took classes from and learned a lot from, including during my qualifying exam.

Of course I would have no data without the use of beamlines 8.3.2 and 12.2.2 of the Advanced Light Source of Lawrence Berkeley National Laboratory and beamlines 2-BM-B, 13-BM-D, 13-ID-D, and 16-ID-B of the Advanced Photon Source at the Argonne National Laboratory and the invaluable staff who work long hours to maintain these facilities and assist users. Thank you Dilworth Parkinson for teaching me how to use and analyze tomography data at beamline 8.3.2, Jason Knight for setting up before experiments at 12.2.2, machining parts, and staying late into the night to help, and Alastair MacDowell for overseeing beamlines 8.3.2 and 12.2.2 and for helpful feedback. A big thanks to Francesco De Carlo, who collected tomography data at 2-BM-B, and Vitali Prakapenka, who kindly collected stishovite diffraction patterns at 13-ID-D to make up for lost beamtime. Yanbin Wang and Julien Gasc maintain and assist users with the D-DIA at 13-BM-D and helped me for more experiments than I can count. Thanks also to Stanislav Sinogeikin of 13-ID-D for helping with set-up at 13-ID-D and Jesse Smith, with set-up and assistance laser heating at 16-ID-B.

Many provided samples and helped with sample preparation. FeO samples were provided by Luke Daemon, Yingwei Fei via Ho-kwang Mao, and Steven Jacobsen. David Martin provided a beautiful neighborite sample. Thanks to James Wu of the Material Science Division of the Lawrence Berkeley National Laboratory for assistance and the use of his vacuum heater to produce more neighborite.

I would also like to thank collaborators. A special thanks to Lowell Miyagi for being a great role model, making most of the 2-phase samples, and helping me learn how to analyze diffraction patterns. A big thanks to Jane Kanitpanyacharoen who sat through numerous beamtimes with me and helped me load samples. Thank you Eloisa Zepeda Alarcon for making beamtimes so much fun! Mulder and Scully forever! I appreciate assistance from collaborators Sergio Speziale and Sebastian Merkel who collected FeO diffraction patterns. Sergio, you were also great to work with on the FeO paper! I also appreciate help from Hauke Marquardt who sat with me through the night at one of my first beamtimes collecting FeO diffraction patterns. Thank you Jung-Fu Lin for the use of diamond anvil cells, advice on loading samples, and a productive trip to Austin. For polycrystalline plasticity modeling, Carlos Tomé developed the viscoplastic self-consistent code used to determine slip systems, and Ricardo Lebensohn developed the code that uses fast Fourier transform and Green functions to model deformation of different microstructures of halite and neighborite. I also appreciate feedback from research group members Martin Kunz, Roman Vasin, Marie Jackson, John Grimsich, and Paulo Monteiro.

I am grateful to the Carnegie/Department of Energy Alliance Center (CDAC), the National Science Foundation, and the Francis J. Turner Fellowship for financial support.

Additionally, I would like to thank the staff of Earth and Planetary Science. A special thanks to Tim Teague for maintenance and help with the XRD and scanning electron microscope in McCone, use of the press and the heater to make neighborite, and assistance with sample preparation of SiO_2 samples, 2-phase samples, and 16 thin sections of quartzites. Charley Paffenbarger who helps with computers and printers, and Stephen Thompson who maintains the Baribu cluster, thank you. And Margie Winn, thanks for being a friend and teaching me that John Wayne is not an African American rapper like Lil' John or Lil' Wayne.

I will miss Berkeley and the wonderful people I have met here. Mong-Han Huang, thanks for always being a great friend, and especially for helping me bury my cat when she died. Thank you Ian, Dave, Sanne, and Zack for being weird and fun and smart. All the game playing, camping, backpacking, drinking, eating, dancing, and talking we did helped make this a great five years. Carolina, I'm glad I get to enjoy the Saturday life with you! Thank you to Daniella for being generous and supportive when bad things happened.

Thank you to non-geology friends Alice, Mary, Megan, and Eric. Thanks to Wayne for always being awesome and ridiculous.

Lastly, my family has been very supportive. Mom and Greg, I'm lucky to have such generous, warm parents. Dad, you're a badass, and it's nice to know you're proud of me, too. Thanks Dan and Michelle for living in Central Valley for a while and feeding me and letting me take a break from student life. Thanks, Eva, for brushing my hair, and Caleb and Ryland, for playing race cars with me. You were always great to visit! Matt, Erica, Ava, and Brynn were also fun to visit! Thanks, Matt, for all the camping equipment that I used extensively here in California. And thanks to Erica for delicious food, and to Ava for all the lovely drawings. Betsy Campen, thank you for being like a second mother to me in grade school when we lived in Echo Canyon and for introducing me to geology.

Chapter 1

Introduction

The massive amount of heat, roughly 44TW, which radiates from Earth's interior is largely transported through the core and the mantle via convection. Mantle convection has long been thought to be coupled to the motion of tectonic plates (e.g. Turcotte and Oxburgh 1967, Lay and Garnero 2004), and in fact seismic tomography has imaged hot upwelling plumes and downgoing cold crustal slabs (Garnero and McNamara 2008) extending all the way to the bottom of the mantle (e.g. Grand et al. 1997, van der Hilst et al. 1997) that are part of this convective process. Large strains result from mantle convection (e.g. predicted by geophysical models, McNamara et al. 2002, McNamara et al. 2003, Wenk et al. 2006) and from plate motions, causing large scale deformation of mantle and crustal minerals. Earthquakes near the surface of the Earth lead to brittle fracturing of rocks, but deep earthquakes and mantle convection take place beneath the brittle ductile transition zone at roughly 13-18 km depth (e.g. Griggs 1936, Byerlee 1968) where rocks deform plastically due to the higher pressure and higher temperatures.

Plastic flow of rocks in the deep Earth is important because it influences geodynamical processes such as melt production above subduction zones (e.g Lev and Hager 2011), post-glacial rebound (e.g. Christensen 1987), mountain-building (e.g. Vauchez and Nicolas 1991), Rayleigh-Taylor instabilities in the lithosphere (e.g. Conrad and Molnar 1997), and plate motion (e.g. Vauchez et al. 1998).

Rocks in the deep Earth deform plastically by a number of dislocation creep or diffusion creep mechanisms. Which deformation mechanism dominates depends on factors such as strain rate, temperature, stress, grain size, and mineralogy. A form of the general creep equation relating these variables to strain rate $\dot{\varepsilon}$ is:

$$\dot{\varepsilon} = A\sigma^n d^{-p} \exp\left(-\frac{Q}{RT}\right)$$

where A is a material constant, σ is the stress, n in the stress exponent, d is grain size, $-p$ is the grain size exponent, Q is the activation energy, R is the gas constant, and T is temperature (e.g. Barber 1990). Effects of pressure and deformation history are not explicitly included in the above equation as separate terms but would affect material parameters A and Q. Water content has been shown to effect deformation, particularly in quartz (e.g. Kronenberg and Tullis 1984, Hobbs 1984, Koch and Christie 1989) and olivine

(e.g. Jung and Karato 2001), and an oxygen fugacity term $f_{O_2}^{q}$ is sometimes included in creep equations.

Creep, either by diffusional flow or dislocation flow, is a time-dependent deformation process that occurs in materials deforming at constant or near constant strain rate, so at high enough temperatures (typically >30% of the melting temperature) such that diffusive mechanisms maintain a zero net effect of strain hardening or work hardening (e.g. Barber 1990). Both diffusion creep and dislocation creep become more active at higher temperature, however diffusion creep tends to dominate over dislocation creep at higher temperatures and lower stress. Materials deforming in the diffusion creep regime behave as Newtonian fluids whose strain rate is directly proportional to stress ($n = 1$ in the above equation). Mechanisms of diffusion creep (e.g. coble creep, Nabarro-Herring creep, bulk diffusion) are grain-size dependent, and typically $-p = 2$ or 3. Conversely, deformation by dislocation creep highly depends on stress, and for minerals typically $n = 3 - 10$ (e.g. Barber 1990, Wenk et al. 1986, Chen et al. 2002). Mechanisms in this regime (e.g. dislocation slip, dynamic recrystallization) are controlled by recovery mechanisms such as dislocation climb and partial annihilation of dislocations and are largely grain size independent (i.e. $p = 0$). Grain boundary sliding, mentioned again in Chapter 4, must be accommodated by other mechanisms in either the diffusion creep or dislocation creep regimes. It is both grain size dependent ($-p \geq 1$) and stress dependent ($n > 1$).

An important effect of dislocation activity is the rotation of crystallographic lattice planes toward a preferred orientation during slip. This thesis focuses on plastic deformation by slip in the deep Earth and the resulting crystallographic preferred orientation and anisotropy.

Dislocation slip in response to non-hydrostatic stress on a crystal causes crystallographic planes to reorient. Stress introduces dislocations in the lattice, and with further applied stress, they begin to propagate, i.e. "slip" or "glide," on different slip systems, defined by sets of (hkl) crystallographic planes and [uvw] directions. Slip occurs more easily on slip systems that require lower resolved shear stress to initiate slip, called the critical resolved shear stress (CRSS). The resolved shear stress on a slip system is related to its orientation relative to the major stress component for axial compression by Schmid's law $\tau = \sigma\cos\theta\cos\lambda$ where τ is the shear stress, σ is the applied compressive stress, θ is the angle between the compression direction and slip plane normal, and λ is the angle between the compression direction and the slip direction (Schmid and Boas 1935). Crystals develop a preferred orientation dependent on the relative CRSS and activities of its slip systems and also on the orientation of slip systems relative to the major stress component.

Many models exist for predicting crystallographic preferred orientation (CPO), from relative CRSSs. The models proposed by Taylor (Taylor 1938) and Bishop and Hill (Bishop and Hill 1951) assume that strain in each grain is uniform throughout a polycrystal, and thus equal to the macroscopic plastic strain. It is a Full Constraints (FC) approach that imposes the same deformation to every grain. While it satisfies full compatibility, it does not satisfy equilibrium at grain boundaries and ignores any deviation from the average grain deformation due to relative anisotropies, i.e. it does not allow grains in "hard" orientations to deform more slowly than grains in "soft" orientations. So while Taylor-Bishop-Hill theory can accurately predict deformation in mostly isotropic minerals, it does not do well with very anisotropic material or minerals that do not satisfy the von Mises criterion. These minerals, such as olivine (Mg_2SiO_4), have too few slip systems (less than five) for homogeneous deformation, (e.g. Wenk et al. 1991). On the other hand, the Relaxed Constraint (RC) formulation (e.g. Kocks and Canova 1981, Honneff and Mecking 1981) allows for variation of strain among grains, based on grain shape and stress continuity. However, it still does not consider relative stiffness among grains. In contrast to imposing strain equilibrium, a model proposed by Sachs (1928) imposes stress equilibrium, deforming isolated grains in a homogenous stress field. This approach more accurately predicts texture for minerals with fewer than five slip systems, but strain compatibility is not maintained, causing extreme strain concentrated in a few grains, which leads to inaccurate texture predictions.

Another approach is plastic compromise between compatibility and equilibrium. Viscoplastic self-consistent (VPSC) modeling (Molinari et al. 1987) considers a grain inside of an anisotropic medium with the average characteristics of the aggregate, called a homogenous equivalent medium (Lebensohn and Tomé 1993) based on the Eshelby inclusion formulation (Eshelby 1957). The model is described as self-consistent, because the stress and strain rate over all the grains must be equal to the equivalent macroscopic magnitudes of the equivalent medium. Soft slip systems are more active, and grains with optimal orientations and shapes relative to the major stress component deform more quickly. VPSC has been used to accurately predict deformation in more anisotropic materials such as quartz (e.g. Takeshita et al. 1999) or olivine (e.g. Tommasi et al. 2000).

Crystallographic preferred orientation (CPO), or "texture," is of interest, because it can lead to seismic anisotropy, i.e. when seismic waves travel faster in some directions than in others. Wave velocities depend on many factors, including density, temperature, elastic properties of material, and texture. Akin to medical imaging, seismic tomography uses wave velocities to map density changes with depth, large structural anomalies, and anisotropy throughout the Earth. Layers of the Earth and corresponding pressures and temperatures have been inferred from discontinuities in seismic velocities with depth (e.g. Bullen 1947, Birch 1952, Dziewonski and Anderson 1981). Since, the Earth's interior has

been mapped in 3D in greater detail, and large hot piles of material below Africa and the Pacific Ocean (e.g. Hofmann 1997, Kellogg et al. 1999, Cottaar and Romanowicz 2012) have been detected, and subducted crustal slabs have been imaged in the mantle (e.g. Steinberger 2000). In addition, the difference in arrival times of compression waves (*P*-waves) traveling in different directions and of orthogonally polarized transverse waves (shear or *S*-waves) allows detection of anisotropy. Seismology has found the upper mantle to be anisotropic, likely due to CPO in olivine (e.g. Hess 1964, Zhang and Karato 1995, Dawson and Wenk 2000). However, the lower mantle is largely isotropic except at the top of the lower mantle near the transition zone (Wookey et al. 2002, Wookey and Kendall 2004, Faccenda 2014), near locations of downgoing slabs (Wookey and Kendall 2004) and upwelling plumes (e.g. Kawai and Geller 2010, Cottaar and Romanowicz 2013), and at the bottom of the lower mantle in the D'' layer (e.g. Kendall and Silver 1996, Lay et al. 1998, Panning and Romanowicz 2004). Isotropy in the lower mantle may be due to deformation mechanisms which do not produce CPO (Meade et al. 1995), such as grain boundary migration or diffusion creep (Karato et al. 1995).

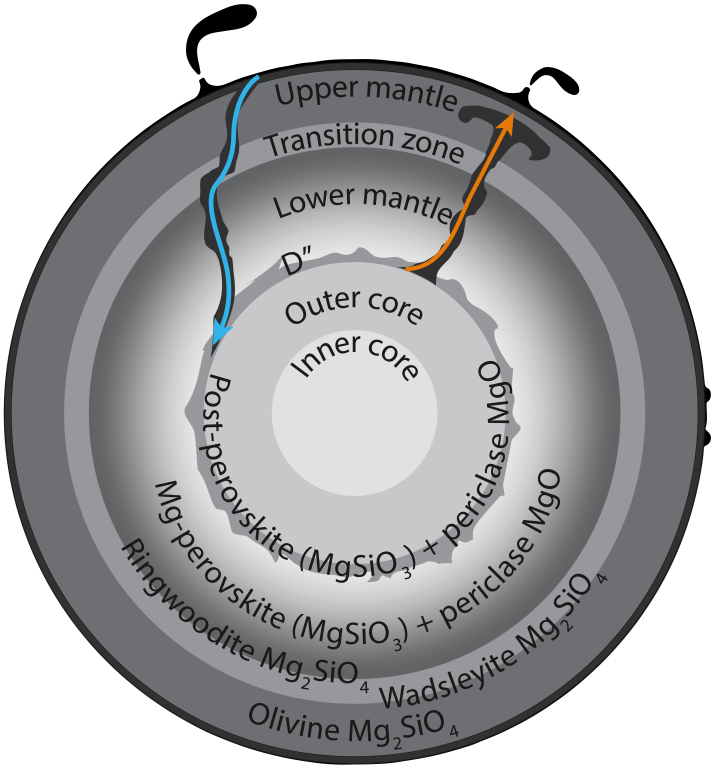

Figure 1. A cartoon depicting the layers of the Earth (labeled in top half) with a cold downgoing slab elucidated with a blue arrow, and a hot upwelling plume, with an orange arrow. The series of transitions of Mg_2SiO_4 that occur with depth are labeled in the bottom half.

Composition of the deep Earth, where no direct observations can be made, is inferred from comparison of these seismic observations to the behavior of minerals subjected to deep Earth conditions in experiments (e.g. Bovolo 2005). Seismic anisotropy is often linked to CPO. Development of CPO during deformation in minerals at conditions similar to the deep Earth can be examined with X-ray diffraction in a high pressure apparatus such as a diamond anvil cell (DAC) (e.g. Wenk et al. 2006) or a multianvil press (e.g. Karato and Weidner 2008), such as the Deformation-DIA (D-DIA) (Wang et al. 2003). In both these apparatuses, pressures and temperatures in the deep Earth are simulated by advancing anvils to apply hydrostatic stress while the sample is being heated either internally by coupling a laser with the sample to reach temperatures of up to 6000 K (e.g. Boehler 2000) (more common in DAC) or with an external resistive heater, which can reach temperatures up to 2000 K (e.g. Duffy 2005) but with better control and uniformity than laser heating (more common in multianvil press). In addition, the sample is subjected to axial, differential stress causing it to deform elastically and plastically, with the latter possibly leading to CPO. While samples are being deformed at high pressure and high temperature, X-ray diffraction images can be collected which are most interesting if the X-ray beam path is perpendicular to the compression direction. This allows all orientations of crystallographic planes relative to compression (from parallel to compression to perpendicular to it) to be observed as Debye rings on a detector placed behind the sample. Orientations that are preferred will produce a higher intensity spot on the detector, creating intensity variations along Debye rings.

DAC and D-DIA experiments allow examination of deformation *in situ* which is important for documenting texture evolution in minerals as stress is applied. It is especially useful for examining phase transitions as they occur at high pressure and/or temperature, and observing textural evolution in phases that only exist at high pressure and high temperature.

In Chapter 2, results from compression experiments of polycrystalline magnesiowüstite, $(Mg_{0.08}Fe_{0.88})O$, and wüstite, $Fe_{0.94}O$, as they undergo a phase transition from cubic symmetry to rhombohedral symmetry are presented and discussed. At ambient conditions, (Mg,Fe)O has cubic rocksalt crystal structure. At ~18 GPa, (Mg,Fe)O with at least 80% iron content (Jacobsen et al. 2004, Kondo et al. 2004, Kantor et al. 2006) undergoes a displacive, martensitic phase transition to rhombohedral crystal structure via lengthening of one body diagonal (e.g. 111), and shortening of the other three. Deformation of the body diagonals is due to extreme softening of the corresponding elastic constant C_{44} with pressure (Jackson et al. 1990, Mao et al. 1996). Since the transition to a rhombohedral phase is only seen in magnesiowüstite with high iron content, some suggest that softening of C_{44} is due to the paramagnetic-to-antiferromagnetic transition in wüstite near 5 GPa (Jackson et al. 1990, Mao et al. 1996,

2002, Koči et al. 2007, Yagi et al. 1985), yet others disagree (Kantor et al. 2004a, 2004b, 2007; Ding et al. 2005).

To further investigate the cubic-to-rhombohedral phase transition, X-ray diffraction patterns were collected during compression in a DAC in radial geometry to observe evolution of CPO through the phase transition and up to 37 GPa. Polycrystal plasticity simulations are used to infer likely slip systems. Portions of this chapter have been previously published in Kaercher et al. (2012). I am the first author on this paper, and contributions from others are duly noted in the Acknowledgements.

For a displacive phase transition such as the cubic to rhombohedral phase transition in FeO, bond lengths change but bonds do not break, and the crystallographic structures and corresponding textures of the two phases are directly related. Such phase transitions occur for many other materials and commonly in metals, for example the bcc-fcc-hcp transition in iron (e.g. Miyagi et al. 2008) or the alpha-omega transition in zirconium (e.g. Wenk et al. 2013). However, not all transitions are displacive. The second most abundant mineral in the Earth's crust, quartz, undergoes a reconstructive phase transition to coesite followed by another transition to stishovite with increasing pressure. Neither a structural nor textural relationship can be drawn among quartz and its high pressure polymorphs because bonds are broken and reformed.

In Chapter 3 texture in quartz and one of its higher pressure polymorph stishovite are examined. Stishovite has the same crystal structure is rutile (TiO_2) with octahedral coordination of Si and has been studied in detail (e.g. Stishov and Belov 1962, Sinclair and Ringwood 1978, Ross et al. 1990). Yet little is known about texture development during deformation. Stishovite in diamond inclusions suggest its existence in the upper mantle where it was likely transported in subducting crustal slabs (e.g. Kesson et al. 1994) and may contribute to observed mantle anomalies (Vinnik et al. 2001, Asahara et al. 2013). However, no direct measurements of CPO in stishovite which would provide insight into the anisotropic character of possible anomalies have been made. Thus information about texture development in stishovite was collected during laser heated DAC experiments at pressures up to 38 GPa. Results are discussed and likely slip systems inferred from VPSC are compared to earlier microstructural studies done with transmission electron microscopy.

Chapters 2 and 3 examine preferred orientation in single-mineral polycrystalline samples. However most of the Earth is comprised of multi-mineral rocks. The addition of a second phase is known to affect deformation regime, and so may also affect slip and thus preferred orientation. However not many experimental studies examine polymineral deformation. This is the content of Chapter 4.

The lower mantle, estimated to be ~25% magnesiowüstite (Mg,Fe)O and ~70% Mg-perovskite ($MgSiO_3$) from seismic data, mineral physics, and primitive meteorites and solar nebula composition (e.g. McDonough and Sun 1995), presents an interesting and relevant system in which to study two-phase deformation. The lower mantle may appear to be mostly isotropic if anisotropic features are smaller than what can be resolved by seismic tomography (e.g. Panning and Romanowicz 2004, 2006; Wenk et al. 2006a; Kustowski et al. 2008). Alternatively, the lower mantle may truly be isotropic if dominant deformation mechanisms in the lower mantle do not produce CPO (Meade et al. 1995, Karato et al. 1995). Several studies suggest the latter may be true by demonstrating that the softer phase, (Mg,Fe)O in this case, in a two-phase aggregate controls the mode of deformation (e.g. Tullis and Wenk 1994, Herwegh et al. 2011) and greatly reduces CPO by promoting other deformation mechanisms over slip. In order for the softer phase to control deformation, it is likely interconnected and acting as a lubricant between grains of the harder phase. Some studies find that this may not be the case, and that the harder phase controls the deformation (e.g. Madi et al. 2005, Yoshino et al. 2008).

Because the deformation regime depends on many variables, in order to constrain the effects of a second phase, the stress state and temperature should be well controlled, and grain size and microstructure should be well characterized. It is difficult to control the stress state in the DAC, which imposes both hydrostatic and non-hydrostatic stress in a sample in a confining gasket as the anvils are advanced. Neither can a constant strain rate be maintained since pressure membranes commonly used in DAC experiments apply pressure incrementally. In addition, laser heating, which is commonly used in DAC experiments, is unstable and leads to considerable temperature gradients (e.g. Manga and Jeanloz 1996, Boehler 2000). Grain size cannot be reliably determined in samples under high stress from X-ray diffraction patterns, necessitating *ex situ* examination of microstructure using electron microscopy or tomography. Although recovery of deformed samples from the DAC is possible, samples often become encrusted on a diamond and cannot be removed. Alternatively, deformation in a multianvil press allows hydrostatic and non-hydrostatic stress to be applied separately and for controlled resistive heating up to 2000 K. Deformed samples can easily be recovered for examination with electron microscopy or microtomography. However, pressures in a multianvil press such as a Deformation-DIA cannot exceed ~12 GPa.

Since D-DIA cannot reach pressures of the lower mantle, analog minerals halite (NaCl) and neighborite ($NaMgF_3$), which have the same structures and similar relative strengths as the original mantle minerals, were chosen. Reasons for choosing these analogs and evaluation of their success in predicting deformation in minerals MgO and $MgSiO_3$ perovskite are discussed in Chapter 4. Sintered cylinders with various volume fractions of NaCl and $NaMgF_3$ were deformed at moderate temperatures in the D-DIA while X-ray

diffraction patterns were collected *in situ*. Information on grain structure and distribution before and after deformation was collected using X-ray microtomography. The effects of phase volume fraction and microstructure on development of CPO are discussed and compared with results from polycrystal plasticity models.

Chapter 2

Crystallographic preferred orientation in wüstite (FeO)

2.1 Introduction

As one of the major lower-mantle mineral phases along with (Mg,Fe)SiO_3 perovskite, the mechanical properties of $(Mg_xFe_{1-x})O$ [hereafter referred to as (Mg,Fe)O] at high pressure have implications for the rheology and composition of the lower mantle (Jeanloz and Thompson 1983). For instance, preferred orientation of (Mg,Fe)O crystals due to differential stress may contribute to localized areas of seismic anisotropy in down-going slabs and upwelling plumes in the convecting lower mantle. This is because large strain from mantle convection is at least partially accommodated by propagation of dislocations along slip planes (Wenk et al. 2011). In turn, this leads to lattice rotation and ultimately crystallographic preferred orientation (texture) which causes seismic waves to travel faster in some directions than in others. Comparison of seismic data with mineral physics helps constrain the composition of the lower mantle.

Magnetic properties of (Mg,Fe)O at depth are also important, and hence the effect of pressure on the electronic structure of Fe in (Mg,Fe)O has been the subject of intense research (Lin et al. 2013). At ambient conditions (Mg,Fe)O crystallizes in a face-centered cubic (B1) structure consisting of a close-packed O-sublattice with Mg and Fe occupying octahedral interstices. Due to such a simple structure based on one single coordination polyhedron for the cation species, even subtle changes at the Fe-site have a visible effect on the properties of the whole material, sometimes at moderately low Fe contents. Changes in the electronic structure of Fe at high pressure can affect the magnetic properties of (Mg,Fe)O (e.g. Pasternak et al. 1997, Badro et al. 1999), for example, a spin collapse crossover at pressures above 40 GPa, depending on Fe content (Gramsch et al. 2003, Speziale et al. 2005, Fei et al. 2007, Lin et al. 2003, 2005a, 2005b, Mao et al. 2011). Compositions with greater Fe content remain in the high spin state to higher pressure, implying partitioning of Fe from (Mg,Fe)SiO_3 to (Mg,Fe)O with depth, which may (Cohen et al. 1997, Badro et al. 2003) or may not (Irifune et al. 2010) result in a

seismically stratified lower mantle. In addition, the outer core may also be seismically stratified due to magnetic collapse of Fe^{2+} dissolved in Fe-rich liquid (Cohen et al. 1997). Furthermore, it was recently discovered that a metallic cubic phase of FeO exists at pressures and temperatures corresponding to the core-mantle-boundary which would affect the way the magnetic field is propagated to Earth's surface (Ohta et al. 2012). Electronic changes in Fe can also affect the elastic constants at high pressure (Crowhurst et al. 2008, Marquardt et al. 2009, Antonangeli et al. 2011). Lin et al. (2009) observed no change in preferred orientation in polycrystalline $(Mg_{0.83}Fe_{0.17})O$ as pressure increased through the spin transition, suggesting that magnetic changes do not cause changes in deformation mechanisms in Fe-rich compositions of the MgO-FeO solid-solution series.

Several structural changes in FeO occur at pressure. Recent X-ray diffraction experiments suggest a transition from a B1 (NaCl) to a B2 (CsCl) structure at outer core conditions (above 230 GPa and 2500-5000 K) (Ozawa et al. 2011). A more established phase transition to a B8 (NiAs), an anti-B8 structure, or a polytypical combination of the two occurs at pressures above 70 GPa (Jackson and Ringwood 1981, Fei and Mao 1994, Mazin et al. 1998, Murakami et al. 2004). At much lower pressure near 10-20 GPa, another well-studied phase transition from cubic to rhombohedral symmetry in magnesiowüstite (Mg,Fe)O has been observed in the diamond anvil cell (DAC) (Zou et al. 1980, Mao et al. 1996, Shu et al. 1998). The rhombohedral distortion occurs via extension of one cube body diagonal and shortening of the other three (Fig. 1) at a pressure that depends on the degree of non-hydrostaticity in the sample chamber (Zou et al. 1980; Jeanloz and Sato-Sorensen 1986; Dubrovinsky et al. 2000), and Fe content of the sample (Lin et al. 2003, Kondo et al. 2004; Kantor et al. 2006; Zhuravlev et al. 2010). In fact, it is debatable whether the cubic-to-rhombohedral transition even occurs for compositions with Fe $\leq$ 20% (Jacobsen et al. 2004, Kondo et al. 2004, Kantor et al. 2006), and it has never been found to occur in pure periclase (MgO) (Duffy et al. 1995). The absence of a rhombohedral phase in MgO points to electronic changes in Fe as the driving mechanism for the transition in (Mg,Fe)O. Indeed, experimental studies have found a paramagnetic-to-antiferromagnetic transition in wüstite near 5 GPa (Zou et al. 1980, Kantor et al. 2004a, 2004b). Some studies propose that this magnetic transition causes the extreme softening of C_{44} found both with experiments (Jackson et al. 1990, Mao et al. 1996, 2002) and *ab initio* calculations (Koči et al. 2007) and thus is ultimately responsible for the structural phase transition (Yagi et al. 1985, Jackson et al. 1990). Others suggest that they do not correlate (Kantor et al. 2004a, 2004b, 2007; Ding et al. 2005).

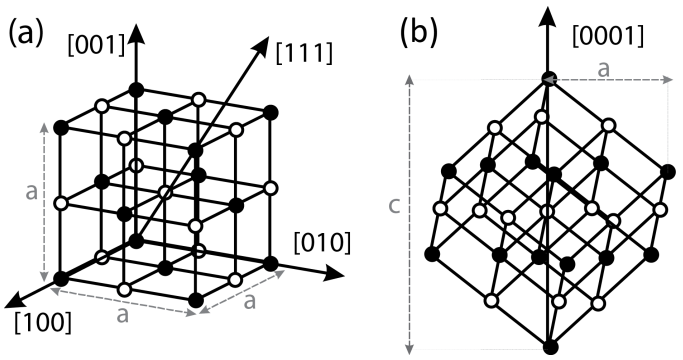

Figure 1. Structure of FeO in (a) cubic and (b) hexagonal reference frames. The $[111]_c$ direction in cubic becomes the $[0001]_r$ hexagonal crystallographic axis.

Despite the number of studies examining the physical changes in (Mg,Fe)O with pressure and temperature, this is the first study to investigate changes in preferred orientation through the cubic-to-rhombohedral phase transition. Synchrotron X-ray diffraction experiments were performed *in situ* in radial DAC experiments. Slip systems activities leading to the observed texture were investigated using viscoplastic self-consistent (VPSC) modeling in order to gain further insight into the transition.

2.2 Experiments

Synthesized powders of magnesiowüstite $(Mg_{0.08}Fe_{0.88})O$ and wüstite $(Fe_{0.94}O)$ were compressed up to 37 GPa in the DAC in X-ray diffraction experiments at beamline 12.2.2 of the Advanced Light Source at Lawrence Berkeley National Laboratory. Experiments were performed in radial geometry (Fig. 2)(Wenk et al. 2006) rather than in axial geometry in order to see variations in diffraction intensities as a function of the azimuthal angle η on Debye rings (the angle with respect to the diamond anvil culets) which indicates preferred orientation of the lattice in the crystal aggregate. No pressure medium was used in order to impose deviatoric stress in addition to hydrostatic pressure.

2.2.1 Magnesiowüstite $(Mg_{0.08}Fe_{0.88})O$

A powder sample of $(Mg_{0.08}Fe_{0.88})O$, the same as sample 10–1 in Bonczar and Graham (1982), also used in Speziale et al. (2005), (2007), was prepared by sintering a mixture of MgO, Fe_2O_3, and Fe at ~1000°C as described in Bonczar and Graham (1982). Chemical composition was quantified with wet chemical analysis. The sample was loaded into an X-ray-transparent boron-epoxy gasket inside of a kapton sheet. The sample chamber was ~80 μm in diameter and ~50 μm deep. A ~5μm-thick gold flake ~15 μm in diameter was placed in the sample chamber and used as a pressure calibrant, applying the equation of state (EOS) for Au (Shim et al. 2002). The diamond culets were 300 μm in

diameter. A modified Mao-Bell DAC with large lateral openings for radial diffraction was loaded into a holding frame where pressure was increased with a lever arm operated by a single screw. The sample was placed ~129 mm from the detector, and a monochromatic X-ray of wavelength 0.354241 Å was collimated to a beamsize of 10 μm ×10 μm and focused onto the sample. Diffraction images were collected for 20 seconds on a Bruker PT200 charge-coupled device (CCD). Instrument parameters, such as sample-to-detector distance, beam center, and detector tilt, were calibrated using a LaB_6 standard.

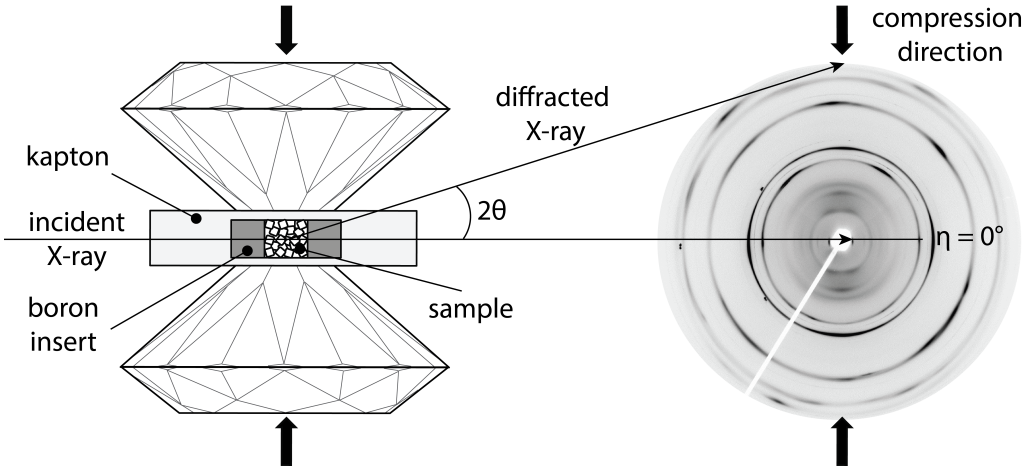

Figure 2. Illustration of a diamond anvil cell in radial geometry

2.2.2 Wüstite ($Fe_{0.94}O$)

A similar experiment was performed with $Fe_{0.94}O$ powder prepared by heated Fe_2O_3 to 1473K in a CO-CO_2 mixing furnace to control oxygen fugacity as described in Fei (1996). Fei (1996) characterized sample non-stoichiometry by measuring the lattice parameter with X-ray diffraction and found a = 4.307(1) corresponding to a ~5% iron vacancy (Hazen 1981). Iron-rich compositions in the MgO-FeO solid solution have complex defect structures and are invariably non-stoichiometric (Jeanloz and Sato-Sorensen 1986). To help account for this non-stoichiometry in the analysis of the data, I used the elastic constants for a sample with similar iron vacancy, $Fe_{0.945}O$ (Jackson et al. 1990). An X-ray-transparent kapton/boron-epoxy gasket with a sample chamber 80 μm in diameter and 50 μm deep was used. A small flake of Pt (Alfa Aesar foil ~20 μm in diameter and 5 μm thick) was embedded in the sample and used as a pressure indicator using the EOS for Pt (Menéndez-Proupin & Singh 2007). Diamond culet diameter was again 300 μm. A nitrogen gas pressure membrane was used to apply pressure and uniaxial

stress to the sample inside of a Mao-Bell DAC. The sample was placed ~345 mm from a MAR345 image plate detector, and diffraction patterns were collected for 120 seconds with a 0.49594 Å wavelength X-ray beam 10 μm in diameter. A LaB_6 powder standard was used to calibrate instrument parameters.

2.3 Data Analysis

Rietveld refinement (Rietveld 1969), a least squares method, was implemented in the software package MAUD (Lutterotti et al. 1997) to find a calculated fit to experimentally collected diffraction patterns. By calculating the best fit to hydrostatic peak position, i.e. at azimuthal angle $\eta = 54.7°$ from the compression direction (Singh et al. 1998; Merkel et al. 2009), cell parameters are determined, and thus the volume of the unit cell. In addition, peak width, sinusoidal variations of peak position in 2θ, and regular changes in peak intensity (Fig. 3) were fit in order to find the crystallite size and root mean square (r.m.s.) microstrain, differential stress, and preferred orientation, respectively.

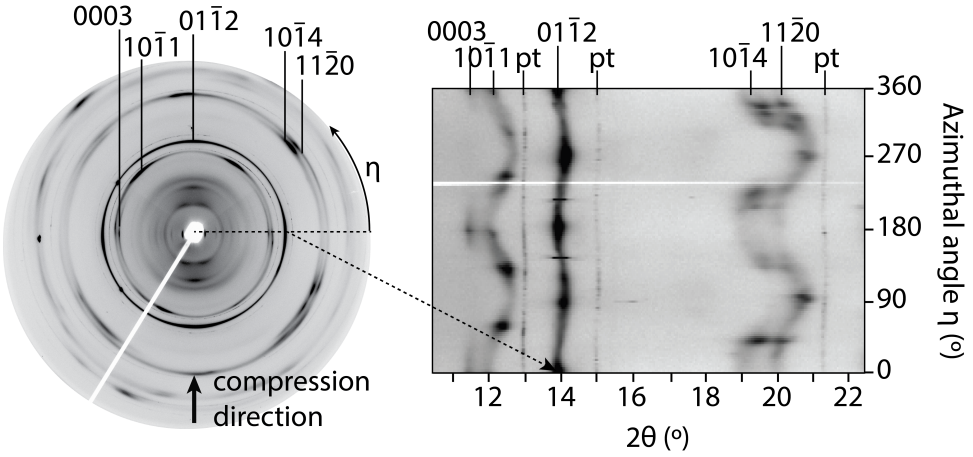

Figure 3. (a) Diffraction image of $Fe_{0.94}O$ collected at 36 GPa in the rhombohedral phase. The diffraction rings are labeled with hexagonal *hkil* indices. The solid curved arrow shows the direction of increasing angle η. Compression direction is vertical (arrow). (b) Image in (a) has been unrolled. Dashed arrows show corresponding areas of maximum intensity of the $01\bar{1}2_r$ Debye ring/peak. The white horizontal streak is from the beamstop.

Crystallite size and r.m.s. microstrain were both calculated assuming an isotropic grain size. The r.m.s. microstrain (hereafter referred to as microstrain), the average lattice

distortion due to plastic strain in a crystal, was calculated from the width of the Gaussian component of the Voigt function that was used to fit our diffraction peaks (Lutterotti and Scardi 1990).

Periodic variations in both peak position and intensity are best seen by unrolling Debye rings. This was done in Fit2D (Hammersley et al. 1996), and diffraction intensity was integrated every 5° in η for a total of 72 spectra (Fig. 3). Integrated 2D plots (Fig. 4) with experimental diffraction patterns (bottom) and the calculated fit (top) are shown for the cubic (a) and rhombohedral phases (b).

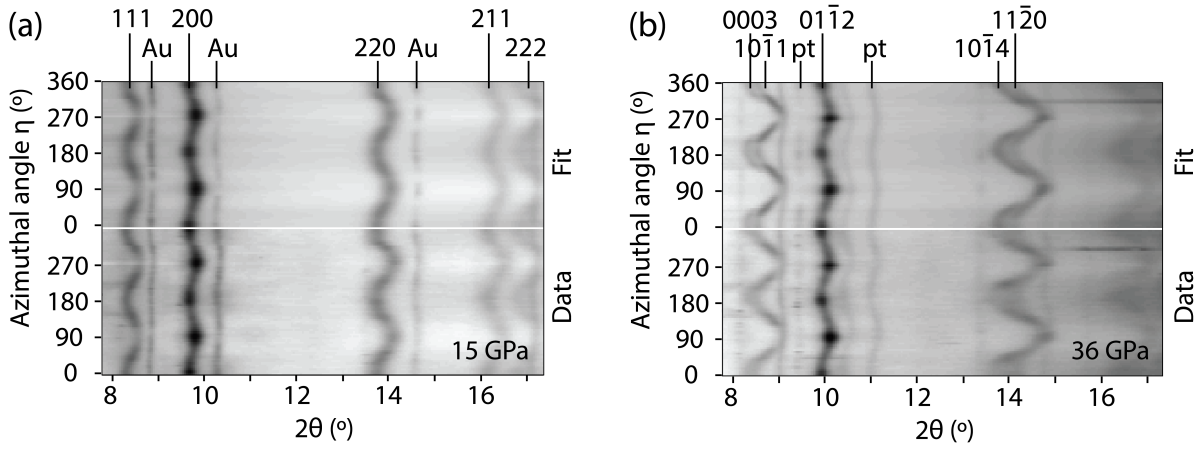

Figure 4. Unrolled diffraction images for (a) $(Mg_{0.08}Fe_{0.88})O$ at 15 GPa, and (b) 36 GPa. The phase transition from face-centered cubic to rhombohedral is marked by splitting of both the 111_c and the 220_c peaks, but not the 200_c peak. The bottom half of each pattern is the experimental data and the top is the calculated fit. Small cubic peaks, diffracted from sample which spilled outside the sample chamber, are present in the rhombohedral phase but are not labeled in the 36 GPa spectra. Notice the strong texture of the 0003_r peak, making it visible only at angles η near 0° and 180°.

2.3.1 Stress

The diamond anvils and gasket imposed both hydrostatic pressure and uniaxial stress on the sample. The hydrostatic stress component is determined as a function of volume change (i.e. peak position in the diffraction pattern) of Au and Pt which were used as calibrants. Here I used the EOS of the calibrants rather than the sample itself since the EOS of the rhombohedral phase for any composition of (Mg,Fe)O is unknown.

Because no pressure medium is used, the sample is subject to non-hydrostatic conditions. Sinusoidal variations in peak positions with respect to the compression direction (Fig. 4b) indicate that deviatoric stress imposed by the DAC has caused the sample to strain elastically. Elastic strain, unlike plastic strain is reversible deformation in which bonds are stretched but not broken. Deviatoric stress, the stress experienced in different crystallographic directions, can be calculated from the non-isotropic elastic strain and the single crystal elastic constants. Since the latter are yet unknown for the rhombohedral phase, deviatoric stress could only be determined for the cubic phase.

Differential stress t in the cubic phase was calculated from the principal stresses σ_{11}, σ_{22}, and σ_{33}. The stress distribution is assumed to be cylindrically symmetric about the compression axis x_3 such that the least compressive stress, σ_{11} and σ_{22}, are equal. Differential stress is then defined as $t = \sigma_{33} - \sigma_{11}$ (Singh et al. 1998). Principal stresses σ_{11} and σ_{33} for the cubic phase were found using the Moment Pole Stress model (Matthies et al. 2001) implemented in MAUD which uses the elastic constants of $Fe_{0.945}O$ as a function of pressure (Jackson et al. 1990) as input and the BulkPathGeo stress/strain model (Matthies et al. 2001) to fit the strain (exhibited as waviness in peaks). Deviatoric stress can then be calculated from the differential stress t:

$$\delta\sigma_{ij} = \begin{bmatrix} -t/3 & 0 & 0 \\ 0 & -t/3 & 0 \\ 0 & 0 & 2t/3 \end{bmatrix}$$

where the uniaxial stress is applied in the x_3 direction (corresponding to the compression axis in the DAC), and. In this study the standard convention of defining compressive stresses as negative and extensional stresses as positive is used.

Because elastic constants are not known for the rhombohedral phase, the Radial Diffraction in the DAC approach of Singh et al. (1993, 1998), as implemented in MAUD, was used to fit elastic strain. As seen in Fig. 4, some peaks exhibited much higher lattice strain than others (e.g. $10\bar{1}1$), and Singh's model is able to fit the strain in each peak individually by refining the parameter $Q(hkl)$ (defined in Singh et al. 1998). The parameter $Q(hkl)$ is related to the change in d-spacings produced from deviatoric stress by

$$d_m(hkl) = d_p(hkl)[1 + (1 - 3\cos\psi^2)\, Q\,(hkl)]$$

where $Q\,(hkl) = \frac{t}{3}\left(\frac{\alpha}{2G_R^X(hkl)} + \frac{1-\alpha}{2G_V}\right)$, d_m are the measured lattice d-spacings, d_p are the lattice d-spacings under hydrostatic pressure, α is a weighting factor between 0 and 1, $G_R^X(hkl)$ is the aggregate shear modulus (limited to the crystallites that contribute to the

recorded diffraction effect) calculated under the Reuss (iso-stress) condition, and G_V is the shear modulus under the Voigt (iso-strain) condition. Differential stress t can be determined from $Q(hkl)$ if the elastic anisotropy of the phase is known (Singh et al. 1998, Merkel et al. 2002).

2.3.2 Texture

Systematic variations in peak intensity with azimuth η (seen in Fig. 4) indicate crystallographic preferred orientation, or texture. Crystallographic texture was fit using E-WIMV, a tomographic algorithm similar to WIMV (Matthies & Vinel 1982a,b) but able to compensate for irregular pole figure coverage. Pole densities in the pole figures were roughly symmetric about the compression direction as expected for DAC geometry, thus I imposed cylindrical symmetry. The orientation distribution was calculated with a 15° resolution and subsequently smoothed with a 7.5° Gauss filter before calculating pole figures and inverse pole figures with the software BEARTEX (Wenk, et al. 1998).

2.4 Results

Lattice parameters, microstrain and differential stresses were determined at various pressures between 0 and 37 GPa for both $(Mg_{0.08}Fe_{0.88})O$ and $Fe_{0.94}O$. The results are summarized in Table 1. Our measured unit cell parameter at ambient conditions for $(Mg_{0.08}Fe_{0.88})O$ was 4.2952(1) Å, in excellent agreement with 4.2954(5) Å as measured by Bonczar and Graham (1982). The starting cell parameter for $Fe_{0.94}O$ was 4.2940 Å, 0.3% smaller than that measured by Fei (1996). The difference is likely due to a small amount of stress applied when closing the DAC.

The phase transition from cubic ($Fm\bar{3}m$) to rhombohedral ($R\bar{3}m$) occurred near 19 GPa in both experiments, in good agreement with Yagi et al. (1985), Mao et al. (1996), Mao et al. (2002), and Murakami et al. (2004). The rhombohedral distortion occurs via extension of one cube body diagonal and shortening of the other three (Fig. 1). This is evidenced in the subtle change in d-spacing from cubic $d_{(111)}$ = 2.43 to rhombohedral $d_{(0001)}$ = 2.44 and $d_{\{10\bar{1}1\}}$ = 2.39. The extended body diagonal becomes the c-axis in the rhombohedral phase where a hexagonal coordinate system is used to describe the structure.

Table 1. A summary of cell parameters, c/a ratios, microstrain, differential stress (t), and texture sharpness given in m.r.d. as a function of pressure and temperature in cubic (C) and rhombohedral (R) phases. Minimum and maximum m.r.d. for IPFs in Fig. 8 are listed in the right-most column. Numbers in parentheses are standard deviations.

Exp.	Phase	P (GPa)	a (Å)	c (Å)	c/a	Micro-strain	t (GPa)	Pole dens.(m.r.d.) min	Pole dens.(m.r.d.) max
$(Mg_{0.08}Fe_{0.88})O$	C	0.6	4.2952(1)	--	--	0.00428(9)	-0.02	0.67	1.80
	C	7.4	4.2467(2)	--	--	0.00638(5)	-1.63	0.51	3.08
	C	13.7	4.2020(1)	--	--	0.00779(7)	-2.14	0.39	3.28
	C	18.7	4.141(3)	--	--	0.009(1)	-3.14	0.09	2.22
	R	18.7	2.9229(1)	7.3167(7)	2.5032	0.00642(3)	--	0.23	3.94
	R	27.4	2.8635(1)	7.2492(8)	2.5316	0.00536(4)	--	0.14	4.15
	R	36.6	2.8430(2)	7.1895(9)	2.5288	0.00634(5)	--	0.00	6.48
	C	1.8	4.276(1)	--	--	0.0054(1)	-0.01	0.71	2.50
$Fe_{0.94}O$	C	0.2	4.2940(4)	--	--	0.0033(2)	-0.42	0.64	1.84
	C	10.6	4.21783(8)	--	--	0.00541(3)	-2.21	0.31	2.69
	C	14.5	4.19488(9)	--	--	0.00644(3)	-2.58	0.31	3.15
	C	18.8	4.1720(7)	--	--	0.0040(1)	-3.25	0.19	2.64
	R	18.8	2.9184(2)	7.3659(9)	2.5240	0.00439(3)	--	0.31	2.82
	R	24.9	2.8938(1)	7.3210(5)	2.5485	0.00478(2)	--	0.26	2.93
	R	36.2	2.8278(2)	7.311(1)	2.5855	0.00600(5)	--	0.28	2.90
	C	9.1	4.2301(4)	--	--	0.00638(4)	-2.15	0.18	7.28

Table 2. Values for the parameter $Q(hkl)$ for five crystallographic directions in the rhombohedral phase.

Exp.	P(GPa)	$Q(0001)$	$Q(10\bar{1}1)$	$Q(01\bar{1}2)$	$Q(10\bar{1}4)$	$Q(11\bar{2}0)$
$(Mg_{0.08}Fe_{0.88})O$	18.7	0.0049(2)	0.00980(7)	0.00444(2)	0.0085(1)	0.00897(6)
	27.4	0.0154(3)	0.0184(1)	0.00644(3)	0.0160(1)	0.01442(8)
	36.6	0.0177(3)	0.01841(9)	0.00596(3)	0.0171(2)	0.01454(7)
$Fe_{0.94}O$	18.8	0.0078(3)	0.0151(1)	0.00404(3)	0.0138(2)	0.0123(1)
	24.9	0.0152(2)	0.01504(5)	0.00417(2)	0.01533(9)	0.01385(5)
	36.2	0.0199(3)	0.0170(1)	0.00500(3)	0.0280(2)	0.0159(1)

At 19 GPa, the c/a ratio in both samples was already higher than the ideal cubic c/a ratio ($\sqrt{6} = 2.4495$), where c is a body diagonal in the cubic phase) and increased

continuously to 2.5228 at 36.6 GPa in $(Mg_{0.08}Fe_{0.88})O$, and 2.5855 at 36.2 GPa in $Fe_{0.94}O$ (Table 1). The latter is similar to $c/a = 2.603$ at 38.9 GPa reported by Zou et al. (1980) for FeO. Overall c/a ratios for $Fe_{0.94}O$ were consistently higher than for $(Mg_{0.08}Fe_{0.88})O$.

2.4.1 Microstructure and stress

Microstrain increased with pressure in the cubic phase of $(Mg_{0.08}Fe_{0.88})O$ from 0.00428(9) at 0.6 GPa to 0.00779(7) at 13.7 GPa, then decreased across the phase transition to 0.00536(4) at 27.4 GPa and increased again with pressure in the rhombohedral phase until the load was reduced. Microstrain increased in a similar fashion in $Fe_{0.94}O$. Microstrain was relieved by the rhombohedral distortion in both experiments, suggesting that some strain imposed by the anvils was accommodated by the displacive transition.

During compression, differential stress t decreased from -0.02 GPa at 0.6 GPa to -3.14 GPa at 18.7 GPa in cubic $(Mg_{0.08}Fe_{0.88})O$ and from -0.42 at 0.2 GPa to -3.25 at 18.8 GPa in cubic $Fe_{0.94}O$, which corresponds to increasing compression, as expected. Because elastic constants of rhombohedral FeO are unknown, values for the parameter $Q(hkl)$ are instead listed for five crystallographic directions: $[0001]_r$, $<10\bar{1}1>_r$, $<01\bar{1}2>_r$, $<10\bar{1}4>_r$, and $<11\bar{2}0>_r$ (Table 2). The $Q(hkl)$ values increase with pressure, indicating increasing elastic strain with pressure, as expected. After decompression back to 1.8 GPa with the $(Mg_{0.08}Fe_{0.88})O$ sample, differential stress increased to -0.01 GPa, nearly the starting value as anticipated for elastic strain. No image was taken near ambient pressure following decompression for $Fe_{0.94}O$ because the beam shut off.

2.4.2 Texture

The three-dimensional orientation distribution that describes the orientations of crystals in a polycrystalline sample may be displayed in two-dimensional pole figures or inverse pole figures . Pole figures (PFs) describe lattice plane poles relative to sample coordinates, and inverse pole figures (IPFs) display the orientation of the sample symmetry axis (in this case, the compression direction) relative to crystal coordinates. Although PFs are somewhat more intuitive to read than IPFs, IPFs are more efficient for representing texture for axially symmetric textures. Here I show both and provide instructions on how to interpret each. Both are represented in equal area projection.

2.4.2.1 Pole figures and cubic texture

Some PFs showing preferred orientation in the cubic phase of $(Mg_{0.08}Fe_{0.88})O$ at 13.7 GPa are presented in Fig. 5 (top row). Contour lines separate areas with different pole densities. Angles η in the PFs with the highest pole densities, measured in multiples of random distribution (m.r.d.), directly correlate with angles of maximum intensity in the unrolled diffraction pattern (Fig. 4b) for the corresponding peak *hkl*. A PF with m.r.d. = 1 shows random orientation while a pole figure with a maximum m.r.d. = 3 has crystals that are three times more likely found in that orientation. The compression direction is in the center of each pole figure (at η = 90°).

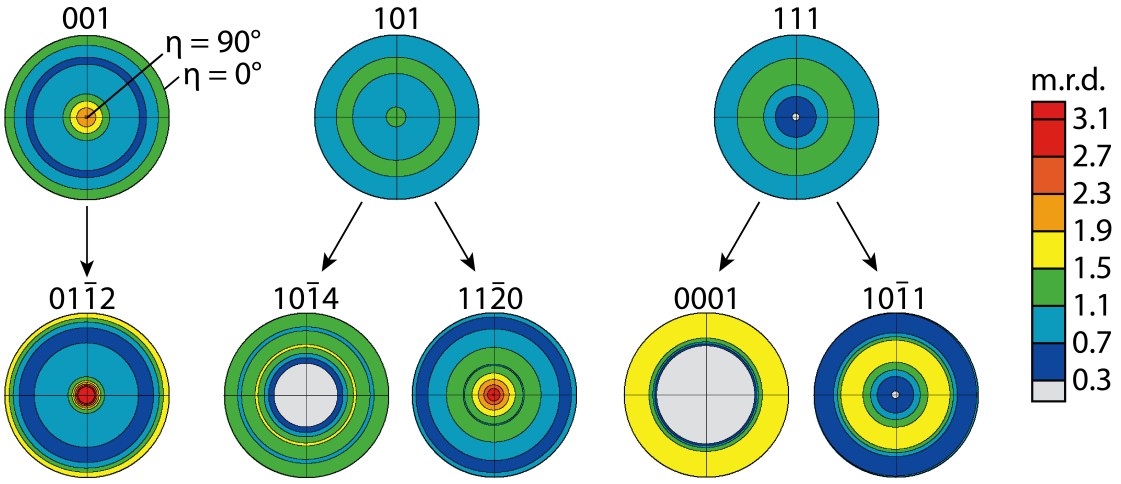

Figure 5. Pole figures showing texture of cubic $(Mg_{0.08}Fe_{0.88})O$ at 13.7 GPa and room temperature (top row) and at 36.6 GPa and room temperature (bottom row). The crystallographic lattice plane normals being viewed are indicated above each pole figure. The compression direction (η = 90°) lies in the center of each pole figure while the axis perpendicular to the compression direction (η = 0°) lies in the peripheral. An m.r.d. = 1 indicates no preferred orientation is present. A value with an m.r.d = 3 indicates that the crystal face being viewed is three times more likely to align in that direction than if the crystals were randomly oriented. Equal area projection.

The 001_c PF (Fig. 5) for $(Mg_{0.08}Fe_{0.88})O$ has two maxima: one located in the center of the PF, and a weaker concentration at η = 0°; 101_c has two concentrations, one in the compression direction, and another as a girdle at η = 45°; 111_c has only a single concentration at η = 37.5°. This is consistent with cubic symmetry. Thus $\{001\}_c$ planes in cubic $(Mg_{0.08}Fe_{0.88})O$ are preferentially aligned perpendicular to the compression

direction at pressure. The same was true for $Fe_{0.94}O$. Initially both samples were nearly randomly oriented and developed the texture shown in Fig. 5 upon compression in the DAC (texture evolution is discussed in greater detail below).

Near 19 GPa, the 111_c and the 220_c diffraction peaks in the cubic phase split, whereas the 200_c peak did not (Fig. 4b), indicating the lowering of crystal symmetry from cubic-to-rhombohedral. In other words, the $\{111\}_c$ planes are no longer symmetrically equivalent to each other and neither are the $\{101\}_c$ planes; however, $\{001\}_c$ remain equivalent and become $\{01\bar{1}2\}_r$.

2.4.2.2 Pole figures and rhombohedral texture

PFs in Fig. 5 (bottom row) show that the $\{01\bar{1}2\}_r$ lattice planes of the rhombohedral phase remain preferentially oriented perpendicular to the compression direction. The $\{101\}_c$ planes give rise to two families of rhombohedral planes $\{10\bar{1}4\}_r$ and $\{11\bar{2}0\}_r$, and the $\{111\}_c$ planes, to $(0001)_r$ and $\{10\bar{1}4\}_r$. While the parent $\{101\}_c$ planes do not strongly align perpendicular or parallel to the compression direction, one of its daughters, $\{11\bar{2}0\}_r$, orients perpendicular to the compression direction, and the other, $\{10\bar{1}4\}_r$, aligns at a lower angle to the compression direction. A similar case of variant selection occurs for $\{111\}_c$, with $\{10\bar{1}1\}_r$ orienting more closely perpendicular to the compression direction than $(0001)_r$.

2.4.2.3 Inverse pole figures and textural evolution

To help illustrate how to read IPF's, two stereographs of equal-area projection depict the orientation of a single crystal in the cubic (Fig. 6a) and the rhombohedral (Fig. 6b) reference frames. Labels denote the location at which (*hkl*) poles and [*uvw*] directions would intersect a hemisphere placed above the crystal (represented by the stereographs). Note that the poles perpendicular to planes $(10\bar{1}1)_r$ and $(10\bar{1}4)_r$ are no longer parallel to vectors $[10\bar{1}1]_r$ and $[10\bar{1}4]_r$, respectively, in the rhombohedral phase. Except in the case of cubic symmetry, it is rare for lattice plane normals (*hkl*) to coincide with the directions of the same indices such that [*u*=*h*, *v*=*k*, *w*=*l*].

Fig. 7 shows IPFs for the compression direction (top) and for an axis perpendicular to the compression direction (bottom). The first set of IPFs in Fig. 7 (a) show preferred orientation of cubic $(Mg_{0.08}Fe_{0.88})O$ as viewed down the $[001]_c$ lattice vector. In the second set of IPFs (Fig. 7 b), the projection of the cubic texture has been rotated first around $[1\bar{1}0]_c$ by 54.7° clockwise (if looking in the $[1\bar{1}0]_c$ direction) to bring $(111)_c$ into

the center, then around $[111]_c$ by 150° clockwise. Cubic texture is shown as viewed down $[111]_c$ to show the relationship between cubic (Fig. 7 b) and rhombohedral texture (Fig. 7 c). Maxima seen in (a) and (b) are equal but rotated, but texture maxima in (b) and (c) differ. Specifically, the pole densities at $\{10\bar{1}4\}_r$ and $\{11\bar{2}0\}_r$ are no longer equal, and neither are the pole densities at $(0001)_r$ and $\{10\bar{1}1\}_r$. IPFs for the axis perpendicular to the compression direction (Fig. 7 a,b,c) show the same trend: $\{10\bar{1}4\}_r$ and $\{11\bar{2}0\}_r$ no longer have the same pole densities in (c), and neither do $(0001)_r$ and $\{10\bar{1}1\}_r$.

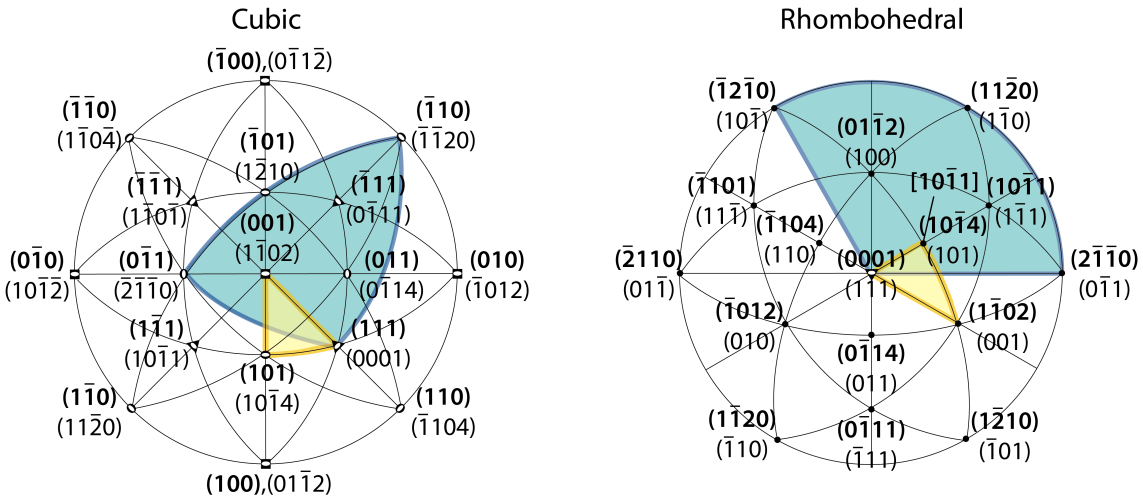

Figure 6. Stereonets for the cubic reference frame (left) and the rhombohedral reference frame (right). Bolded coordinates pertain to the stereonet they are located in, and equivalent coordinates are shown in plain text. Squares denote poles with 4-fold symmetry, triangles denote 3-fold symmetry, black ovals, 2-fold symmetry, and white ovals, inversion points. The area covered by the cubic IPF is denoted with dotted texture while the area covered by the rhombohedral IPF is shown in lighter grey. Indices for lattice plane normals are in rounded parentheses, those for lattice directions in square brackets. Equal area projections.

The entire IPF (360°) is usually not shown as crystal symmetry makes it redundant. It is standard to instead show only the areas contained within the dotted lines in Fig. 7, and this is what is displayed in Fig. 8. The starting textures in Fig. 8 are weak; however, there is already a maximum of 1.84 m.r.d. at 0.2 GPa at $\{001\}_c$ in $Fe_{0.94}O$ likely due to the fact that differential stress was already -0.42 at 0.2 GPa. As mentioned earlier, some stress may have been applied to the sample when closing the DAC. Texture sharpness increased with pressure in the cubic phase (here "texture sharpness" refers to the maximum pole density in the PFs and IPFs) at $\{001\}_c$ from 1.80 m.r.d. to 3.28 m.r.d in

$(Mg_{0.08}Fe_{0.88})O$ and from 1.84 m.r.d. to 3.15 m.r.d. in $Fe_{0.94}O$; it also increased at $\{101\}_c$ in $(Mg_{0.08}Fe_{0.88})O$.

Near the phase transition at 19 GPa both the cubic and the rhombohedral phase were present. The maximum at $\{001\}_c$ in the cubic phase disappeared, and a maximum at $\{01\bar{1}2\}_r$ appeared in the rhombohedral phase. In the rhombohedral phase texture sharpness increased with pressure, much more so in the $(Mg_{0.08}Fe_{0.88})O$ sample (from 3.94 m.r.d. to 6.48 m.r.d.) than the $Fe_{0.94}O$ sample (from 2.82 m.r.d. to 2.90 m.r.d). Pole densities increased specifically at $\{01\bar{1}2\}_r$ and $\{11\bar{2}0\}_r$ in both samples.

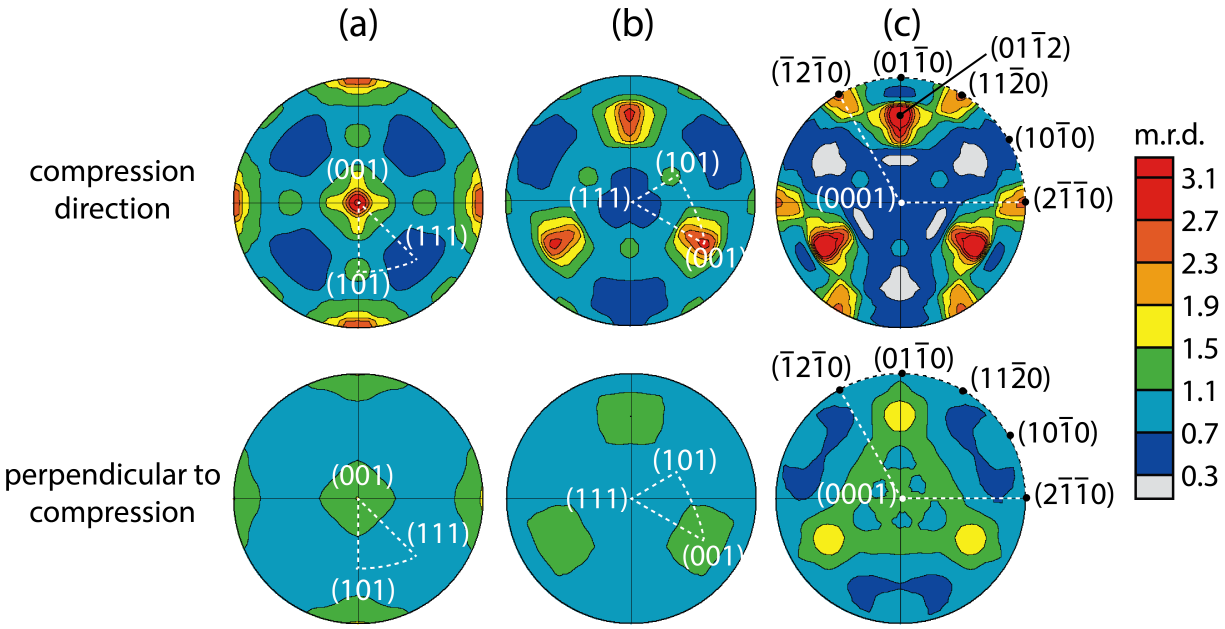

Figure 7. Full inverse pole figures for (a) cubic texture in cubic orientation, (b) cubic texture in rhombohedral orientation, and (c) rhombohedral texture in rhombohedral orientation depicting the crystallographic relationship between cubic $(Mg_{0.08}Fe_{0.88})O$ at 14 GPa and rhombohedral $(Mg_{0.08}Fe_{0.88})O$ at 27 GPa. Areas inside the dotted lines correspond to areas highlighted in Fig. 6 and slices shown in Fig. 8. Important crystallographic directions are labeled. Evidence of variant selection is seen by comparing (b) to (c); directions with equal m.r.d. values in (b) no longer have equal values in (c). Equal area projections.

Upon decompression back to the cubic phase, the maximum at $\{001\}_c$ returned, but stronger than it was before the phase transition: 4.24 m.r.d. in $(Mg_{0.08}Fe_{0.88})O$ and

7.28 m.r.d. in $Fe_{0.94}O$. In addition the secondary maximum at $\{101\}_c$ reappeared in the $(Mg_{0.08}Fe_{0.88})O$ sample and appeared for the first time in the $Fe_{0.94}O$.

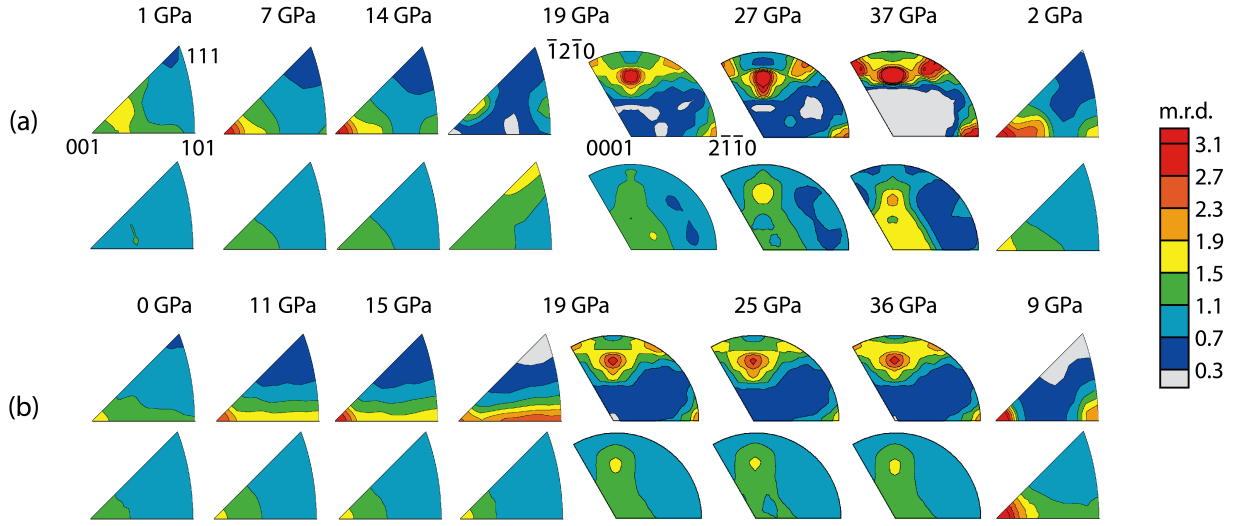

Figure 8. IPFs showing textural evolution of (a)$(Mg_{0.08}Fe_{0.88})O$ up to 36.6 GPa through the phase transition from cubic to rhombohedral and returning to cubic upon decompression; compression direction shown in top row, and axis perpendicular to the compression direction shown in second row; (b) $Fe_{0.94}O$ up to 36.2 GPa. Texture sharpness is measured in multiples of random distribution (m.r.d.). Equal area projections.

2.5 Discussion

2.5.1 Texture

Initial texture at 1 GPa and 0 GPa in $(Mg_{0.08}Fe_{0.88})O$ and $Fe_{0.94}O$, respectively, was weak. As pressure is increased in the cubic phase, a maximum pole density at $\{001\}_c$ in the IPFs (Fig. 8) developed and grew. Similar results for cubic texture were obtained by Merkel et al. (2002) for MgO, by Tommaseo et al. 2006 for $(Mg_{0.4}Fe_{0.6})O$, $(Mg_{0.25}Fe_{0.75})O$, and $(Mg_{0.1}Fe_{0.9})O$, and by Lin et al. (2009) for $(Mg_{0.83}Fe_{0.17})O$.

At the phase transition, near 19 GPa, the maximum in the cubic phase shifted away from $\{001\}_c$ (Fig. 8). This can be explained by crystals in this orientation transitioning to

the rhombohedral phase before crystals in other orientations. This also explains why the maximum at $\{01\bar{1}2\}_r$ developed immediately while the maxima at $\{2\bar{1}\bar{1}0\}_r$ developed later under greater stress. A similar phenomenon of certain crystal orientations transitioning first to a new phase was also observed in the hcp-to-bcc transition in Ti (Lonardelli et al. 2007) and in the bcc-to-hcp transition in Fe (Miyagi et al. 2008).

In the rhombohedral phase, one daughter of $\{101\}_c$, $\{11\bar{2}0\}_r$, orients perpendicular to the compression direction, and the other, $\{10\bar{1}4\}_r$, aligns at a low angle to the compression direction (Fig. 5). Similarly, one daughter of $\{111\}_c$, $\{10\bar{1}1\}_r$, orients more closely perpendicular to the compression direction than its sibling, $(0001)_r$. This variant selection may be because $<10\bar{1}4>_r$ and $[0001]_r$ are the plastically softer of the two sets of directions. Crystals with their $\{10\bar{1}4\}_r$ and/or $(0001)_r$ planes perpendicular to the compression direction would experience the greatest amount of strain along $<10\bar{1}4>_r$ and/or $[0001]_r$. If $<10\bar{1}4>_r$ and/or $[0001]_r$ were soft directions, it would be more favorable for these crystals to rotate or nucleate such that their $\{11\bar{2}0\}_r$ and/or $\{10\bar{1}1\}_r$ planes are at high angles to the compression direction, thus putting stiffer directions $<11\bar{2}0>_r$ and/or $<10\bar{1}1>_r$ more closely parallel to the compression direction. PFs in Fig. 5 show that it is in fact more likely to find crystals in this orientation. This variant selection is briefly explored with viscoplastic self-consistent modeling (VPSC) below.

Upon decompression back to the cubic phase, the reappearance of the maxima at $\{001\}_c$ and $\{101\}_c$ with a greater texture sharpness than before the phase transition (Fig. 8) is likely due to an increase in texture sharpness in the rhombohedral phase during subsequent deformation at $\{01\bar{1}2\}_r$ and $\{11\bar{2}0\}_r$, respectively. The reappearance of the cubic texture also demonstrates that the transition occurs by a martensitic mechanism, i.e. it is due to a reversible lattice-distortive displacement.

Overall, stronger texture developed in the $(Mg_{0.08}Fe_{0.88})O$ sample than in the $Fe_{0.94}O$. Similarly Tommaseo et al. (2006) observed stronger textures in magnesiowüstite samples with higher magnesium content. Stronger texture in the $(Mg_{0.08}Fe_{0.88})O$ experiment may also be due to high plastic strain, as discussed below.

2.5.2 Viscoplastic self-consistent modeling

Both elastic lattice strain and plastic deformation are imposed on the sample during axial shortening in DAC experiments. While elastic strains indicate stress conditions inside the sample chamber and are relatively small, plastic strains are much greater and produce

preferred orientation. Texture development in plastically deforming polycrystals can be approached with polycrystal plasticity models that predict slip system activity and lattice rotations under an externally imposed strain (e.g. Kocks et al. 1998). The viscoplastic self-consistent (VPSC) approach for modeling texture ignores elastic strains and considers only plastic deformation (Lebensohn and Tomé 1994). In VPSC simulations, individual grains deform inside a homogenous but anisotropic medium with the same properties as the aggregate average. Deformation (and rotation) of lattice planes inside grains depends on their orientation relative to the compression direction. However, interaction among individual grains is not taken into account. Also, work hardening is not considered here because there are no data for this system.

By comparing textures produced by VPSC simulations with experimental textures, I estimate slip systems that are active during the experiment. In the simulations, 2000 grains were compressed to 50% and 70% axial shortening in 50 and 70 steps, respectively. For the cubic phase, the observed starting crystallographic orientation distribution was nearly random; correspondingly an initially random orientation distribution was assumed in VPSC. For the rhombohedral phase, both a random starting texture and a cubic starting texture (produced from VPSC) were considered (Fig. 9).

Potential slip systems are well known in B1 structures. In halite, deformation at low temperatures occurs primarily by slip on $\{110\}<1\bar{1}0>_c$, (Carter and Heard 1970, Skrotzki and Haasen 1981), however, harder systems $\{111\}_c$ and $\{100\}_c$ can also be activated. Deformation in MgO is similar, but much more plastically anisotropic (Weaver and Paterson1969, Meade and Jeanloz 1988, Foitzik et al. 1989), making $\{111\}_c$ and $\{100\}_c$ less active than they are in halite. Using these same three slip systems, texture evolution of halite and magnesiowüstite was already explored with polycrystal plasticity modeling (e.g. Wenk et al. 1989b, Merkel et al. 2002, Lin et al. 2009). Here I repeat some of these calculations. Relative critical resolved shear stresses (CRSS) for the cubic phase were chosen to be 0.5 for $\{110\}<1\bar{1}0>_c$, 1.5 for $\{111\}<1\bar{1}0>_c$, and 3.0 for $\{100\}<1\bar{1}0>_c$ to obtain a texture maximum at $\{001\}_c$ in the IPF as observed in experiments. As with the experimental orientation distributions, calculated orientation distributions were smoothed, then plotted as IPF's. Textures produced in VPSC simulations (Fig. 9) can be directly compared to experimental textures (Fig. 8).

A primarily active $\{110\}<1\bar{1}0>_c$ slip system supports the idea that crystals with their $\{001\}_c$ planes at high angles to the compression direction, and thus according to Schmid's Law optimally oriented for $\{110\}<1\bar{1}0>_c$ slip, are the first to transition to the rhombohedral phase as mentioned earlier. Crystals in this orientation do not rotate due to two pairs of slip systems (e.g. $(110)[1\bar{1}0]_c$ and $(1\bar{1}0)[110]_c$) that are at equal angles to

the compression direction, making them equally active in opposite directions, hence cancelling out the rotation of each other. The other slip systems in $\{110\}<1\bar{1}0>_c$ have a Schmidt factor of zero and also do not cause rotation. Meanwhile crystals in other orientations experience less strain as they rotate towards the preferred orientation at a rate that depends on their individual orientations.

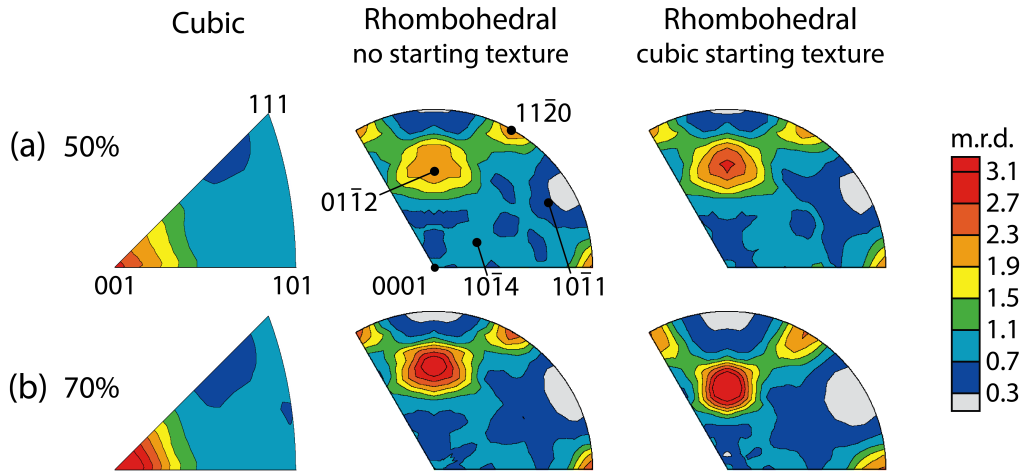

Figure 9. IPFs calculated at (a) 50% and (b) 70% axial shortening produced with VPSC for the cubic and rhombohedral phases of (Mg,Fe)O. Comparison of the effect of random and starting texture on the final texture is shown for rhombohedral (Mg,Fe)O. Simulations with stress exponent $n = 12$ produced the closest match to experiment. Equal area projections.

2.5.2.1 Rhombohedral slip systems

Two sets of VPSC simulations were done for the rhombohedral phase, one with a starting texture of 5000 crystals in random orientation, and one with 2000 crystals in the preferred cubic orientation. The starting cubic texture is the same texture obtained from the VPSC simulations for the cubic phase described above. For both sets of simulations, daughter slip systems in the rhombohedral phase $\{11\bar{2}0\}<\bar{1}101>_r$, and $\{10\bar{1}4\}<1\bar{2}10>_r$, were initially assigned the same CRSS of 0.5 as their parent, $\{110\}<1\bar{1}0>_c$. Similarly, $(0001)<11\bar{2}0>_r$, $\{10\bar{1}1\}<\bar{1}2\bar{1}0>_r$, and $\{10\bar{1}1\}<1\bar{1}0\bar{1}>_r$ were initially given a CRSS of 1.5, and $\{01\bar{1}2\}<2\bar{1}\bar{1}0>_r$, and $\{01\bar{1}2\}<01\bar{1}\bar{1}>_r$, 3.0. CRSS were then varied from these initial values to find the closest match to experimental rhombohedral texture.

For both starting textures, pole density maxima at $\{01\bar{1}2\}_r$ appeared with the starting CRSS mentioned above, producing similar IPFs as shown in Fig. 7c,d. The $\{10\bar{1}1\}<\bar{1}2\bar{1}0>_r$ daughter of $\{111\}<1\bar{1}0>_c$ was then preferentially activated by reducing the CRSS from 1.5 (as it was in the cubic phase) to 1, resulting in a secondary maximum at $\{11\bar{2}0\}_r$ (Fig. 9) as seen in the experimental IPF's. Meanwhile sibling slip systems, $(0001)<11\bar{2}0>_r$ and $\{10\bar{1}1\}<01\bar{1}\bar{1}>_r$ retained the same CRSS they had in the cubic phase. Because $\{10\bar{1}1\}<\bar{1}2\bar{1}0>_r$ is the only slip system with a CRSS that differs between the cubic phase and the rhombohedral phase, it is responsible for the variant selection that aligns $\{11\bar{2}0\}_r$ more closely perpendicular to the compression direction rather than its sibling $\{10\bar{1}4\}_r$.

The VPSC model with initial random texture shows nearly equivalent pole densities at $\{11\bar{2}0\}_r$ and at $\{01\bar{1}2\}_r$, whereas the model with cubic starting texture shows a higher m.r.d. at $\{01\bar{1}2\}_r$, which is also true of the experimental texture shown in Fig. 8. A closer match between VPSC results with cubic starting texture and experiment suggests that preferred orientation was not randomized by the phase transition. Instead crystallographic orientations continued to evolve through the rhombohedral distortion, further supporting the theory that $\{001\}_c$-oriented crystals transition to the rhombohedral phase first.

2.5.2.2 Strain and strain rate sensitivity

VPSC simulations best match experimental results when carried out to 50%-70% strain. For comparison, Lin et al. (2009) found a best match between experiment and VPSC with 100% strain, and Merkel et al. (2002) found a best match with 50-100% strain, depending on applied pressure in the DAC. While 50% strain accurately reproduces texture sharpness for the experiment performed with $Fe_{0.94}O$, 70% strain provides a closer match to data for $(Mg_{0.08}Fe_{0.88})O$. Because total strain on the sample during the experiment cannot be reliably measured, the best estimate for strain, based on VPSC simulations, is 50% and 70% at ~37 GPa in $Fe_{0.94}O$ and $(Mg_{0.08}Fe_{0.88})O$, respectively. The difference in strain may be due to experimental techniques: while pressure was applied more smoothly to the $Fe_{0.94}O$ sample using a remote-controlled gas membrane, it was incrementally and suddenly applied to the $(Mg_{0.08}Fe_{0.88})O$ using a lever-arm. As stated above, it may also be due to the difference in elasticity in the two composition. The plastic strain which is achieved in DAC experiments depends greatly on gasket materials.

Visco-plastic deformation is often described with the flow law introduced in Chapter 1. A simple version of this flow law is $\dot{\varepsilon} = A\sigma^n$ where $\dot{\varepsilon}$ is the strain rate (s^{-1}), A is a constant ($MPa^{-n}\,s^{-1}$), σ is differential stress (MPa), and n is the stress exponent, i.e. the

strain rate sensitivity to stress (e.g. Kirby and Kronenberg 1987). Low values of stress exponent n (i.e. $n \leq 3$) typically corresponds to higher diffusion activity (higher temperatures) causing strain to become distributed over many slip systems (e.g. Kocks 1998). As n increases, diffusion activity decreases and strain becomes concentrated on fewer slip systems. The best match to experimental data for both cubic and rhombohedral was found with $n = 12$, which is reasonable for deformation at ambient temperature with little diffusion.

Table 3. Activities for the slip systems of cubic (Mg,Fe)O and rhombohedral (Mg,Fe)O at 0%, 50% and 70% strain as calculated with VPSC.

Symmetry	Cubic		Rhombohedral					
Slip system	$\{110\}$ $<1\bar{1}0>$	(111) $<1\bar{1}0>$	$\{10\bar{1}4\}$ $<1\bar{2}10>$		$\{11\bar{2}0\}$ $<\bar{1}101>$		$\{10\bar{1}1\}$ $<\bar{1}2\bar{1}0>$	
CRSS	0.5	1.5	0.5		0.5		1.0	
Starting texture	Random	Random	*Activity (%)* Random	Cubic	Random	Cubic	Random	Cubic
0% strain	99	1	45	46	45	46	9	8
50% strain	100	0	48	48	48	48	4	3
70% strain	100	0	48	49	48	49	3	3

Rhombohedral activities are shown for both a starting random texture and a starting cubic texture. CRSS used provide the closest match to experimental textures. Rhombohedral slip systems $(0001)<11\bar{2}0>_r$ and $\{10\bar{1}1\}<1\bar{1}0\bar{1}>_r$ were included in calculations but showed negligible activity and so are not listed. Cubic slip system $\{100\}<1\bar{1}0>_c$ and rhombohedral slip systems $\{01\bar{1}2\}<2\bar{1}\bar{1}0>_r$ and $\{01\bar{1}2\}<01\bar{1}\bar{1}>_r$ were also used in calculations but showed no activity, so are also not listed. Activities and CRSS for 50% and 70% strain listed here correspond to IPFs shown in Fig. 9.

Slip system activities which provided the closest match to experimental textures for $n = 12$ are summarized in Table 3. For $n = 12$, $\{110\}<1\bar{1}0>_c$ is the most active slip system in the cubic phase with CRSS = 0.5; it comprises 99% of slip active at 0% strain and 100% of slip activity at 50% and 70% strain. In the rhombohedral phase, for $n = 12$, slip systems $\{10\bar{1}4\}<1\bar{2}10>_r$, and $\{11\bar{2}0\}<\bar{1}101>_r$ have CRSS=0.5 and each makes up 45% of slip system activity at 0% strain and 48% at 50% and 70% strain with a random starting texture. For a cubic starting texture, each comprises 46% slip system activity at 0% strain, 48% at 50% strain, and 49% at 70% strain. Slip system $\{10\bar{1}1\}<\bar{1}2\bar{1}0>_r$ has CRSS = 1.0 and is responsible for nearly all remaining activity in the rhombohedral phase.

Rhombohedral slip systems $(0001)<11\bar{2}0>_r$ and $\{10\bar{1}1\}<1\bar{1}0\bar{1}>_r$ showed negligible activity and are not listed in Table 3. Cubic slip system $\{100\}<1\bar{1}0>_c$ and its daughter rhombohedral slip systems $(01\bar{1}2)<2\bar{1}\bar{1}0>_r$ and $\{01\bar{1}2\}<01\bar{1}\bar{1}>_r$ showed no activity and so are also not listed in Table 3.

There are some differences between texture observed in experiments and texture obtained from VPSC modelling. For example, the experimental texture in the cubic phase for $(Mg_{0.08}Fe_{0.88})O$ and for $Fe_{0.94}O$ after decompression shows a secondary maximum at $\{101\}_c$ (Fig. 8) that is absent from the VPSC-obtained cubic texture (Fig. 9). The secondary maxima at $\{101\}_c$ appears in VPSC models for a lower stress exponent (e.g. n = 9), or equivalently, slightly increased activity of $\{111\}<1\bar{1}0>_c$. In this study I chose to simplify deformation by describing it with one slip system. A few differences between experimental and modeled texture also exist for the rhombohedral phase: positions of minima and shape of the maximum differ between the experimental IPFs and VPSC-generated IPFs. These differences are likely beyond the resolution of the orientation distribution in MAUD ($15° \times 15° \times 15°$) and are negligible.

2.6 Conclusions

Two powdered samples, $(Mg_{0.08}Fe_{0.88})O$ magnesiowüstite and $Fe_{0.94}O$ wüstite, were compressed non-hydrostatically up to ~37 GPa at ambient temperature in the DAC. Experiments were performed in radial geometry in order to observe textural evolution as a function of pressure. A pole density maximum developed in the center of the 001_c pole figures for both $(Mg_{0.08}Fe_{0.88})O$ and $Fe_{0.94}O$ (Fig. 5) upon compression and texture sharpness increased as pressure increased. Near 19 GPa, the 111_c and 220_c peaks split, while 200_c did not, in both experiments, indicating a transition to the rhombohedral phase. Variant selection aligned $\{11\bar{2}0\}_r$, a daughter of $\{101\}_c$, and $\{10\bar{1}1\}_r$, a daughter of $\{111\}_c$, more closely perpendicular to the compression direction. This may be due to elastically softer crystal directions aligning perpendicular to the compression direction in a more thermodynamically stable arrangement. Unfortunately the elastic constants of Fe-rich members of the MgO-FeO solid solution series are not yet known to confirm this. On the other hand, the variant selection may be due to progressive deformation of the rhombohedral phase with different slip system activities. Using polycrystal plasticity simulations I found deformation in the cubic phase of solid solution (Mg,Fe)O to be due mostly to slip on $\{110\}<1\bar{1}0>_c$ as previously found for other B1 structures. In the rhombohedral phase, slip system activity changed slightly with one of the daughters of $\{111\}<1\bar{1}0>_c$, $\{10\bar{1}1\}<\bar{1}2\bar{1}0>_r$ (inactive in the cubic phase), becoming active.

Interestingly, texture near the transition pressure suggests that crystals in the cubic phase with their $\{001\}_c$ planes facing the compression direction are preferentially oriented to transform to the rhombohedral phase first. Orientations which developed and strengthened in the rhombohedral phase remained after decompression back to the cubic phase. Upon decompression, a texture similar to the cubic one before the phase transition was observed, suggesting a perfect memory during this displacive, martensitic transition.

Chapter 3

Crystallographic preferred orientation in experimentally deformed stishovite

3.1 Introduction

Stishovite is an extremely hard polymorph of SiO_2 thought to exist in the mantle, making its deformation properties relevant to both material science and Earth science. Originally it was produced experimentally (Stishov and Popova 1961) and found to have a rutile structure (space group $P4_2/mnm$, Stishov and Belov 1962, Sinclair and Ringwood 1978, Ross et al. 1990) with its silicon in octahedral coordination rather than tetragonal coordination as do silicon in other, lower-pressure SiO_2 polymorphs. Stishovite has since been documented in meteorites such as the Shergotty (El Goresy et al. 2000), at meteorite impact sites such as Ries Crater, Germany (Shoemaker and Chao 1961, Chao and Littler 1963), Meteor Crater, Arizona, United States (Chao et al. 1962), and Vredefort crater, South Africa (Martini 1978, 1991), and in high pressure metamorphic environments (Liu et al. 2007). First principles calculations (e.g. Cohen 1991, Karki et al. 1997, Teter et al. 1998, Carpenter 2000, Lee and Gonze 1997), Raman spectroscopy experiments (e.g. Kingma et al. 1995), and X-ray diffraction experiments (e.g. Tsuchida and Yagi 1989, Kingma et al. 1996, Andrault et al. 1998, Hemley et al. 2000) find stishovite to be stable at room temperature to at least 47 GPa, coinciding with pressures in the upper mantle. Stishovite is inferred to exist in the upper mantle from inclusions in diamond (Joswig et al. 1999) where it is likely transported as a component in sedimentary layers and mid ocean ridge basalts in subducting slabs (Irifune and Ringwood 1993, Kesson et al. 1994). Thus, stishovite may contribute to seismic anomalies in the mantle (Vinnik et al. 2001, Asahara et al. 2013), yet little is known about deformation mechanisms which provide important information for understanding subduction of quartz-bearing crustal rocks into the mantle.

Previous studies of plastic deformation mechanisms in stishovite by transmission electron microscopy (Texier and Cordier 2006) and in isostructural rutile, TiO_2, by Ashbee and Smallman (1962) are contradictory. To better understand plastic deformation by slip in stishovite aggregates, quartz was transformed to stishovite, then deformed at ambient temperature by increasing pressure to 38 GPa in a radial diamond anvil cell while documenting the evolution of crystallographic preferred orientation (CPO). I inferred deformation mechanisms leading to the observed preferred orientation by comparing with visco-plastic self consistent modeling. These experiments will increase our understanding of deformation and anisotropy in the deep Earth and contribute to geodynamic models.

3.2 DAC experiments

Flint nodules from Cretaceous limestones along the coast of Norfolk, United Kingdom were ground into a fine powder and compressed in diamond anvil cells (DAC) to 23 GPa and 38 GPa at HPCAT and GSECARS beamlines, respectively, of the Advanced Photon Source (APS) at Argonne National Laboratory. Experiments were performed in radial geometry (e.g. Wenk et al. 2006a) rather than axial geometry in order to see variations in diffraction intensities as a function of the azimuthal angle η on Debye rings (the angle with respect to the compression direction; $\eta = 90°$ is labeled in Fig. 1). In order to activate kinetics to transition from quartz to stishovite, both samples were laser heated.

3.2.1 Run 1

The first run was performed at HPCAT beamline 16-ID-B. A modified Mao-Bell DAC with large lateral openings for radial diffraction was used. The sample was loaded into a boron epoxy gasket inside of a kapton insert. A larger sample chamber, ~80 μm in diameter and initially ~50 μm in depth, was used since quartz does not diffract strongly and pressures needed to obtain stishovite are relatively low (~14 GPa) for the DAC. The diamond culets were 300 μm in diameter. No pressure medium was used in order to impose deviatoric stress. Pressure was increased with a gas membrane system. A ~15 μm-diameter, ~5 μm-thick Pt flake, placed on the bottom of the sample chamber, was used to enhance absorption of the laser spot to heat the sample. The sample was placed ~300 mm from the detector. A monochromatic beam with wavelength 0.406626 Å was collimated to a beamsize of 4 μm × 5 μm and focused onto the sample. Diffraction patterns were collected for 40-120 seconds on a Mar CCD (charge-coupled device) detector. Instrument parameters such as detector centering and tilt were calibrated with a CeO_2 standard.

The sample was compressed to 13 GPa, then laser heated using the portable Nd:YLF double-sided laser heating setup at 16-ID-B (Meng et al. 2008) to activate kinetics and induce the transition to stishovite. A flat top laser beam 15 μm in diameter was rastered across the sample for 40 minutes, causing quartz to partially transform to stishovite. A temperature reading could not be collected, but is estimated to be ~1500-2000K. After increasing pressure to 23 GPa at ambient temperature, quartz fully converted to stishovite.

3.2.2 Run 2

A second run was done at GSECARS beamline 13-ID-D in a modified symmetric DAC with side openings 60° wide for radial diffraction. The cell was tilted such that the compression axis was 64.6° from the incoming X-rays (Fig. 1) in order to reduce noise from the boron epoxy gasket (Lin et al. 2010).

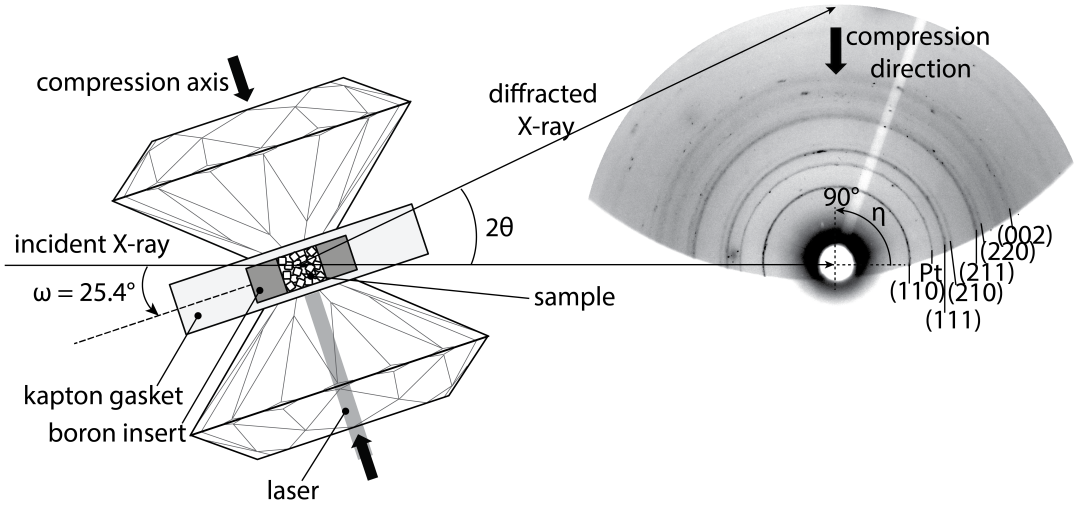

Figure 1. Experimental set-up for diamond anvil cell (DAC) in radial geometry for Run 2. The DAC was tilted 25° to reduce interference from the gasket, however the cell also obscures the bottom of the diffraction pattern when tilted at this angle. The raw diffraction pattern shown on right is #182 (see Table 1).

The sample chamber was again ~80 μm in diameter and ~50 μm in depth, diamond culets were 300 μm, and no pressure medium was used. As in Run 1, pressure was increased with a gas membrane system, and a Pt flake was used to couple with the laser for heating. The sample-to-detector distance was approximately 200 mm. An X-ray beam

with wavelength 0.3344Å and diameter of ~8 μm was focused on the sample, and diffraction patterns were collected for 60 seconds on a Mar-IP345 detector. Instrument parameters were calibrated with CeO_2.

Initial pressure in the closed DAC was 16 GPa. The flint was heated at this pressure with a laser with a flat top diameter of 20-40 μm for 5 minutes using the Nd:YLF laser heating system at 13-ID-D (Prakapenka et al. 2008). The temperature was estimated from the blackbody radiation measured by CCD detector to be ~2200 K. Following heating, sample pressure was 15 GPa. Pressure was then increased in ~5 GPa steps up to 38 GPa, with diffraction patterns taken at 2 μm intervals across the laser heated sample area. Heating was not completely uniform throughout the sample in either run, and some heterogeneities in existed. Pressure was then released to 14 GPa.

3.3 Rietveld Analysis

Diffraction patterns were analyzed using a Rietveld refinement (Rietveld 1969), which is a least squares method that minimizes the difference between the data and a calculated fit by refining backgrounds, phase volume fractions, cell parameters, crystallite size, root mean square (r.m.s.) microstrain, differential stress, and preferred orientation. The Rietveld method was implemented in the software MAUD (Material Analysis Using Diffraction, Lutterotti et al. 1997, Lutterotti et al. 2014, Wenk et al. 2014). Before analysis in MAUD, Debye rings were unrolled in Fit2D (Hammersley et al. 1996), and diffraction intensity was integrated every 5° along the azimuthal angle η for a total of 72 spectra for Run 1, and 36 spectra for Run 2.

For Run 2, the bottom of the tilted DAC blocked diffracted X-rays from reaching the detector, and Debye rings from $\eta \approx 0°$ to 180° only could be collected. While 90° in η is enough to see all crystal orientations relative to compression, 360° is preferred for textural analysis as it provides better counting statistics and diminishes influence from artifacts, such as bright intensity spots from large grains. To maintain better counting statistics, two (180°) diffraction patterns taken at different spots in the sample were analyzed at each pressure for Run 2. The DAC in Run 2 was rotated 25.4° in ω such that the incoming X-ray path was no longer perpendicular to the compression direction (see Fig. 1). To account for this, $\omega = 25.4°$ was defined for each spectra in the dataset in MAUD.

Integrated 2D plots are shown in Fig. 2 with data shown in the bottom half of each plot and the calculated fit on top. The calculated diffraction patterns derive from the experimentally determined structure for quartz (from the MAUD database, space group

$P3_121$) and stishovite (Ross et al. 1990, COD cif # 9001276), with corrections made for the background and refinement of parameters until the calculated diffraction pattern closely resembles the experimental diffraction pattern. A 2θ range of 6.8° to 21° was used in analysis of data from Run 1, and 5.5° to 17.8°, for Run 2 because of high intensity scattering from gasket material present at lower angles and clipping of diffraction peaks by the DAC windows at higher angles. Backgrounds were fit with a fourth order polynomial. Diffuse background peaks at low 2θ from the kapton insert seen near 2θ = 6.8° in Run 1 (Fig. 2) were fit with two background peaks at η =90° and η = 270°. Cell parameters, crystallite size, microstrain, microstress, and crystallographic orientation distribution were then refined until peak position, peak width, and variations in peak position and intensity with azimuthal angle η provided a close match with experiment.

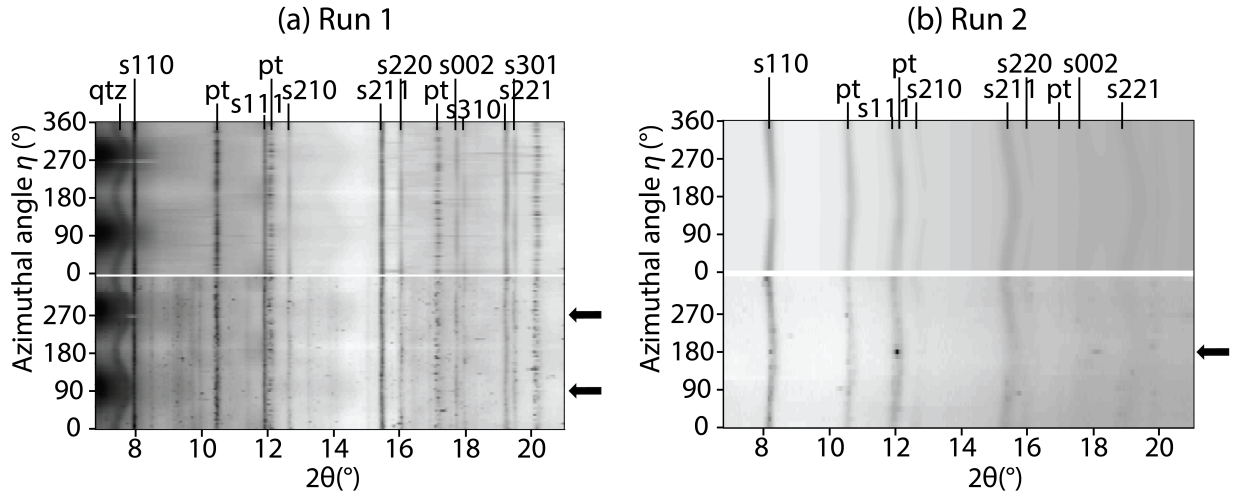

Figure 2. Unrolled diffraction images from Run 1 (#40 at 13 GPa) and Run 2 (#182 at 28 GPa). The bottom half of each pattern is the experimental data and the top is the calculated fit. Compression direction is denoted with arrows. Regular intensity variations with azimuthal angle η denotes CPO. Note, for example the stronger intensity around η = 0°, η = 180°, and η = 360° in stishovite peak 002 (s002), consistent with preferred orientation of [001] poles parallel to compression. In Run 2, the DAC was not tilted, and gasket peaks can be seen in the 2D plot to the right in the bottom (Data) half.

Sinusoidal variations in peak position with azimuthal angle η (e.g. quartz at 2θ = 7.5° in Fig. 2.a) are due to elastic strain in response to differential stress. Differential stress is defined as $t = \sigma_{33} - \sigma_{11}$ (Singh et al. 1998) where σ_{33} is the axial stress component which decreases *d*-spacing in the compression direction, and $\sigma_{11} = \sigma_{22}$ are the stress components perpendicular to compression (and equal due to axial symmetry) which

increase *d*-spacing in the direction perpendicular to compression. The Moment Pole Stress model (Matthies et al. 2001, Wenk et al. 2014) was used to calculate principal stresses σ_{11} and σ_{33} from variations in peak position by using the BulkPathGeo stress/strain averaging model (Matthies et al. 2001) and elastic constants of quartz (Kimizuka et al. 2007) and stishovite (Jiang et al. 2009) as a function of pressure as input.

In addition to elastic strain, non-hydrostatic (differential) stress also imposes plastic strain which can lead to CPO, manifested as variations in peak intensity with η in diffraction patterns. Variations in intensity are best viewed in unrolled diffraction patterns and are especially apparent in the 220 and 002 stishovite peaks in Fig. 2.a. CPO, i.e. texture, was fit using the E-WIMV algorithm, an extension of the WIMV algorithm (Matthies and Vinel 1982a,b) that produces an orientation distribution function (ODF) from data points that are irregularly distributed over orientation space. I chose an ODF resolution of 15°. Because the stress field is expected to be symmetrical about the compression axis, I enforced cylindrical (aka fiber) symmetry in MAUD. The resulting ODF was processed in the software program BEARTEX (Wenk et al. 1998) to create the inverse pole figures shown in Fig. 4.

3.4 Results

A summary for Run 1 and Run 2 of grain size, differential stress *t* (which is negative for compression), and texture strength given in multiples of random distribution (m.r.d.) as a function of pressure is shown in Table 1. Unrolled experimental diffraction patterns presented in Fig. 3 show the degree of elastic strain due to differential stress (sinusoidal variations in peak position) and texture (variations in peak intensity). Image #s in Table 1 correspond to numbers in the upper right hand corner of the plots in Fig. 3.

3.4.1 Run 1

Quartz crystallite size slightly decreased as pressure was applied, consistent with grains being broken, but became a little larger again during heating due to grain growth (Table 1). Stishovite nucleated during laser heating with a crystallite size of ~1 nm at 12 GPa, which decreased to 0.2 nm upon compression to 23 GPa.

Initial pressure in the sample chamber was 2 GPa, and differential stress on quartz was -4.28 GPa (Table 1). Differential stress (*t*), signified by the waviness of peaks in Fig. 3.a, became more negative with pressure (compare #9 to #37), indicating increasing

compression. However immediately after heating, t became less negative (#40, Fig. 3a), consistent with a pressure drop of 1 GPa. Stishovite nucleated with no differential stress, but at a pressure of 23 GPa, already t = 8.31 GPa (#48, Table 1 and Fig. 3a).

Table 1. A summary of cell parameters, microstrain, differential stress (t), and texture sharpness given in m.r.d. as a function of pressure. Minimum and maximum m.r.d. for IPFs in Fig. 4 are listed in the right-most column. Numbers in parentheses are standard deviations.

	Image#		a (Å)	c (Å)	P_{SiO_2} (GPa)	Crystallite size (Å)	t (GPa)	Pole dens. (m.r.d.)	
								min	max
Run 1	9	Q	4.762(1)	5.408(2)	1.8	474 (68)	-4.28(2)	0.88	1.11
	37	Q	4.476(1)	5.158(2)	13.1	413(66)	-6.56(2)	0.74	1.32
	40, 41	Q*	4.499(4)	5.128(8)	12.8	476(7)	-5.22(6)	0.52	1.85
		S*	4.12386(8)	2.6404(1)	11.6	981(7)	0.00(2)	0.69	2.09
	48	S	4.0797(3)	2.6189(5)	22.7	205(4)	-8.31(9)	0.50	2.42
Run 2	19,24	Q	4.4372(6)	5.121(1)	16.3	104.9(9)	-5.37(3)	0.80	1.23
	65,83	Q*	4.4573(5)	5.138(1)	15.2	113(2)	-4.83(3)	0.84	1.17
	113,123	Q	4.3560(8)	5.059(2)	21.4	91(1)	-4.89(3)	0.66	1.36
		S	4.0798(2)	2.6176(4)	22.8	312(6)	-4.89(9)	0.72	1.93
	178,182	S	4.0302(3)	2.5888(5)	38.3	248(13)	-14.0(1)	0.70	2.28
	204,212	S	4.11(2)	2.6389(4)	14.1	246(7)	0.42(6)	0.70	1.60

Texture results are displayed with inverse pole figures (IPFs) showing the sample compression direction relative to lattice orientations in the polycrystal (Fig. 4). Orientations are given in multiples of random distribution (m.r.d.), a measure of pole density normalized to one, such that a polycrystal with m.r.d. = 1 has crystal lattices with no preferred orientation. A very weak texture maximum (1.32 m.r.d.) near $10\bar{1}1$ developed in the quartz upon compression to 13 GPa (Fig. 4a, #37). The sample was then laser heated to activate kinetics and partially converted to stishovite. During heating the quartz texture became stronger (1.85 m.r.d.), and another maximum appeared at 0001.

Stishovite nucleated with 001 poles preferentially aligned with the compression direction with maximum m.r.d. = 2.09. Evidence of preferred orientation is seen in the stishovite 220 peak (Fig. 3a), which has higher intensity at η = 0°, 180°, and 360°, and also in the 002, which has higher intensity at η = 90° and 270° (i.e. the compression direction). This is quantitatively shown in the inverse pole figures #41 and #48 (Fig. 4).

Upon further compression, quartz fully converted to stishovite, and preferred orientation of stishovite increases with the maximum m.r.d. = 2.42 at 23 GPa.

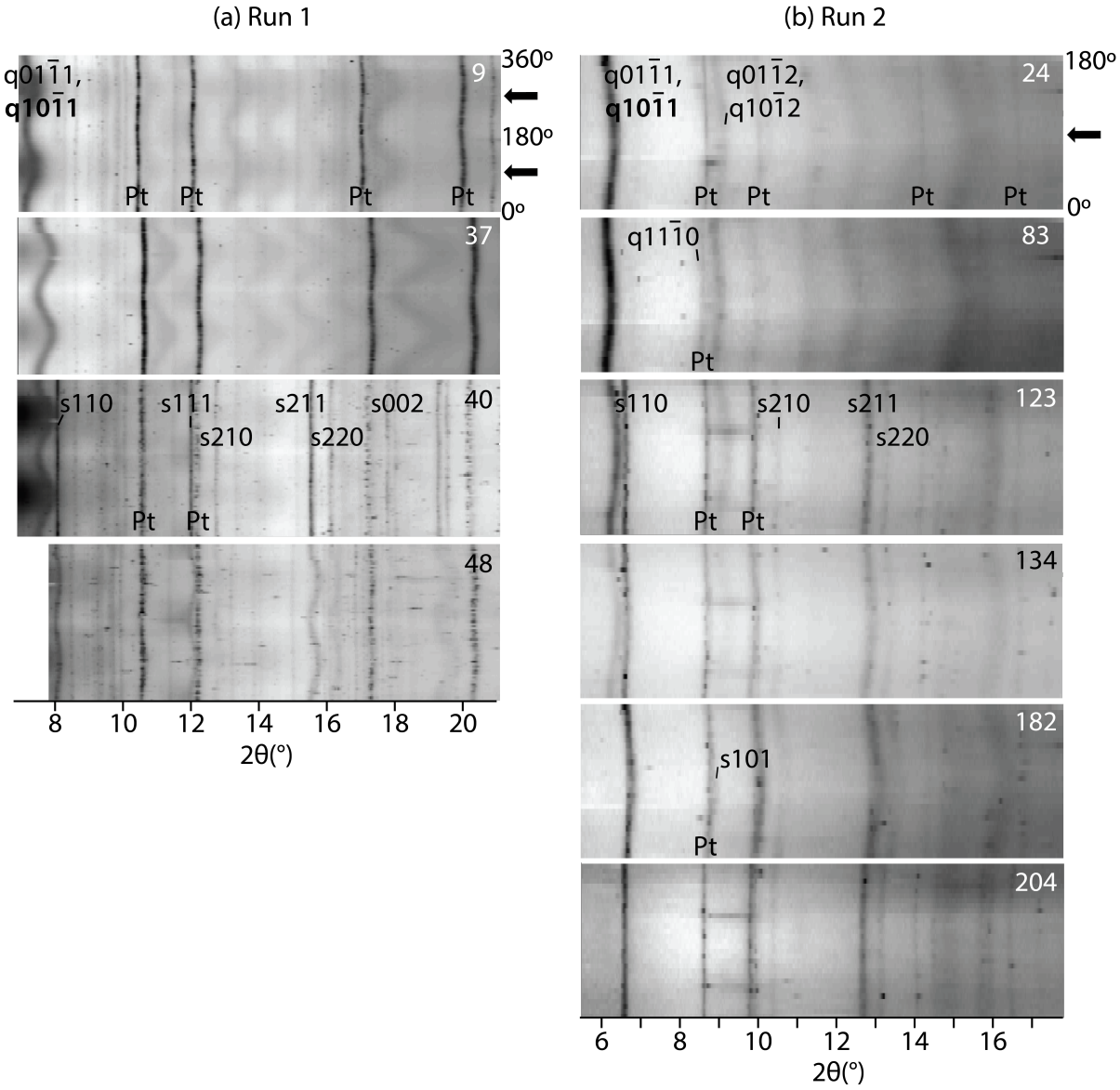

Figure 3. Unrolled diffraction patterns showing 2θ as a function of azimuthal angle η. Numbers in the upper right corner of each pattern correspond to those listed in Table 1. Compression direction is marked with an arrow. Some quartz (q) and stishovite (s) peaks are labeled. Diffraction from more than one crystallographic plane contributes to many peaks; planes which contribute substantially more to intensity are shown in bold.

Note that the stishovite 220 peak is barely visible, and the 002 peak is not visible in #48, Fig. 3.a, implying that textural information at 23 GPa derives mainly from the 110 peak, which somewhat overlaps the diffuse peak from kapton. In addition weaker peaks from the boron epoxy insert are seen, especially between $2\theta \approx 8$ to 10°. Thus experiments were repeated with the DAC tilted in order to reduce diffraction from the gasket material.

The sample was compressed beyond 23 GPa to 56 GPa in Run 1. However, pole densities for diffraction patterns above 23 GPa were irregular, perhaps due to partial transition to the $CaCl_2$ post-stishovite phase (which would complicate texture analysis) due to high differential stress (t = -8.31, Table 1) in the DAC (#48 in Fig. 4a) (Asahara et al. 2013). Because stishovite and post-stishovite are very similar in structure, their diffraction peaks nearly perfectly overlap but may be discerned from each other by comparing peak intensities. However, at high stress, diffraction peaks become diffuse, making peaks from post-stishovite, if it has nucleated, indistinguishable from stishovite peaks. Thus I omitted results for higher pressures.

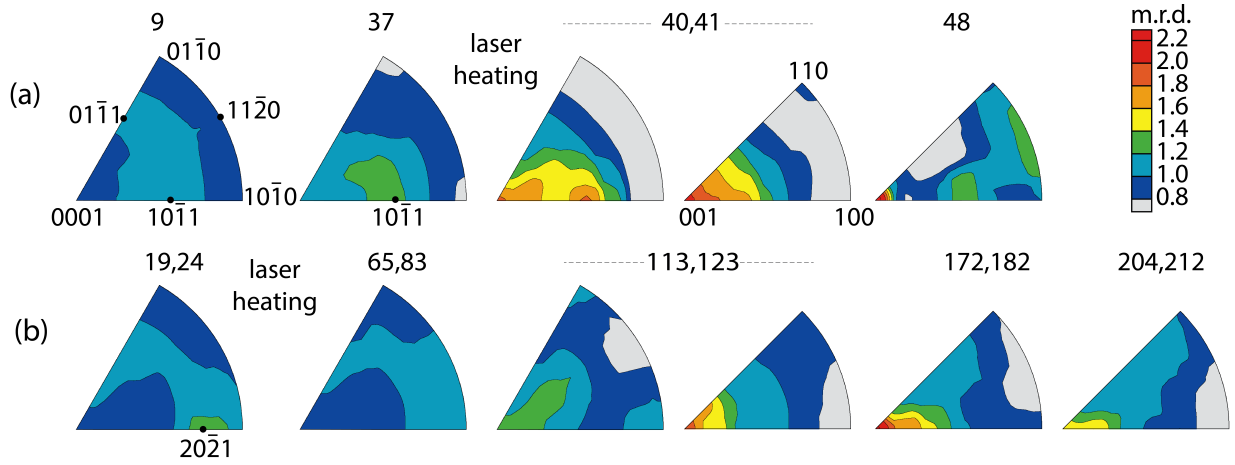

Figure 4. Inverse pole figures (IPFs) for (a) Run 1 and (b) Run 2 showing pole densities of crystallographic faces expressed in multiples of random distribution (m.r.d.). A sample with completely random orientation has m.r.d. = 1. Larger, 60° slices are used to represent CPO in trigonal α-quartz, due to its lower symmetry, and 45° slices represent CPO in tetragonal stishovite. Major crystallographic directions are labeled for quartz and stishovite in (a). Cell parameters, microstrain, differential stress (t), and maximum and minimum pole densities corresponding to each IPF here are shown in Table 1. Equal area projections.

3.4.2 Run 2

The starting pressure in the second experiment was 16 GPa, already well into the stability field for stishovite, so was heated before further compression. During laser heating quartz crystallites grew (Table 1). Compression following heating decreased quartz crystallite size, and caused nucleation of stishovite at 21 GPa. Upon further compression, both quartz and stishovite crystallite size decreased, and at 38 GPa, quartz fully converted to stishovite, as seen by the disappearance of the quartz 101 peak in #182, Fig. 3b.

At 16 GPa, t = -5.37 GPa in quartz, reduced to -4.83 GPa during laser heating, and increased to only -4.93 GPa with further pressure (21 GPa) following heating. Stishovite nucleated at 21 GPa with t = -4.93 GPa as well. Compressive differential stress in stishovite increased to -14.0 GPa at the highest pressure in Run 2, 38 GPa (Table 1). After unloading, t became positive, signifying that the sample was slightly extended, which is consistent with pressure measurements where the ending pressure (14 GPa) is lower than the starting pressure (16 GPa).

At the beginning of Run 2 quartz has a very slight texture maximum (1.23 m.r.d.) near $20\bar{2}1$ which disappears with heating (Fig. 4). Another very weak maximum (1.36 m.r.d.) develops at 0001 when pressure is increased to 21 GPa. Stishovite first appears at 21 GPa with alignment of (001) poles parallel to the compression direction (1.93 m.r.d. maximum). At 38 GPa, the sample fully converted to stishovite, and stishovite preferred orientation increased to 2.28 m.r.d. The sample was then decompressed to 14 GPa, and went into extension, as mentioned above, causing the pole density maximum at 001 to reduce to 1.60 m.r.d.

3.5 Discussion

The sample was under significant stress in both experiments, as indicated by the sinusoidal variations in peak positions (Fig. 3). Yet stishovite nucleated stress-free (t = 0 GPa) in Run 1 during laser heating, as shown by straight lines. However, in Run 2, stishovite did not nucleate during laser heating, which was done for a much shorter amount of time, but instead first appeared after subsequent compression to 21 GPa. At 21 GPa, coincidentally t = -4.89 GPa for both quartz and stishovite. However, the elastic strain in stishovite is much lower than in quartz, as seen in Fig. 3b, #123, where stishovite has straighter peak lines than quartz, because stishovite has much higher elastic constants at this pressure.

Despite differential stress during initial compression in quartz in Run 1 reaching -6.56 GPa, and in Run 2, -5.37 GPa, quartz develops little to no texture. A moderate pole density (m.r.d. < 1.4) is observed near $10\bar{1}1$, especially in Run 1. Such a pattern is consistent with mechanical Dauphine twinning (Tullis 1970). The small average grain size of our flint (< 0.05 μm) and low temperature may explain the suppressed activation of mechanical twinning (Tullis and Tullis, 1972).

Immediately after laser heating in Run 1, the $10\bar{1}1$ maximum in quartz increased to 1.85 m.r.d. and a secondary maximum appeared at 0001 (Fig. 4.a, #40,41). This is likely due to increased differential stress – expansion of the sample from heating is prohibited by the gasket, which imposes increased pressure and stress on the sample, inducing further plastic deformation. Whereas twinning put $\{10\bar{1}1\}$ poles parallel to compression, stress-induced basal slip causes quartz crystals to preferentially reorient with their (0001) poles parallel to compression (Green et al. 1970, Gleason et al. 1993). Similarly in Run 2, the maximum near $10\bar{1}1$ disappears during heating as crystals begin to reorient, and a 0001 maximum appears after pressure is further increased.

In both Run 1 and Run 2, stishovite nucleated with (001) poles preferentially oriented parallel to compression (Fig. 4). This texturing is unrelated to quartz texture, since the quartz-stishovite phase transition is reconstructive. Nucleation of the stishovite under stress may be responsible for its preferred orientation; however, for nucleation in a stress field, thermodynamics predicts alignment of elastically soft directions with the principal stress (e.g. Kamb 1959, Green 1980, Shimizu 1992), while I observe the alignment of the elastically stiffest direction, [001] (Ross et al. 1990, Jiang et al. 2009), with the compression direction. It is also possible that strain in the aggregate (as demonstrated by the waviness of quartz peaks in #40 Fig. 3a and #123 Fig. 3b) may have lead to slip in stishovite causing newly nucleated crystals to immediately preferentially reorient.

The increase in the (001) pole density maximum with further compression is attributed to slip. Electron microscopy studies of microstructures in deformed stishovite (e.g. Cordier and Sharp 1998, Cordier et al. 2004, Texier and Cordier 2006) and isostructural minerals rutile (TiO_2) (e.g. Ashbee and Smallman 1962, Blanchin and Fontaine 1975, Blanchin et al. 1980) and paratellurite (TeO_2) (e.g. Péter et al. 1986) suggest easy slip systems that are likely responsible for the texture that I observe in stishovite.

Cordier and Sharp (1998), Cordier et al. (2004), and Texier and Cordier (2006) examined dislocations in deformed stishovite using TEM and found [001] to be the preferred slip direction. Cordier and Sharp (1998) synthesized stishovite from 99.99% SiO_2

at 15 GPa and 1200 °C under quasi-hydrostatic conditions, resulting in a high density of dislocations. Samples were examined with TEM. They identified Burgers vectors [001], <100>, <101>, and <110> and found [001] to be energetically favorable with the other three having longer Burgers vectors and much higher energies, perhaps due to dissociation. Cordier et al. (2004) synthesized stishovite from wet silica glass at 14 GPa and 1,300 °C, deformed it in a Kawai multianvil apparatus, and also examined dislocations with the TEM. They suggested the easiest slip systems near the quartz-to-stishovite phase transition to be {100}[001] and {110}[001] with secondary slip along <100> and slip on $\{\bar{1}10\}<110>$ becoming more active at higher pressures. Using the same methods as Cordier et al. (2004), Texier and Cordier (2006) again found [001] to be the most active dislocation direction, and <100> active to a lesser extent. They suggest the most easily activated slip systems to be {100}[001] and {210}[001] followed by {010}<100>, (001)<100>, and {021}<100>. They saw scallop shapes for <100> dislocations with dominant or purely edge character; on the other hand, screw dislocations were straight. Because these scallop shapes are observed only for edge segments, they likely result from climb by slow propagation of jog pairs compared to their nucleation rate. Texier and Cordier also found evidence of dislocation climb in the presence of bent dislocations lying in different subgrain boundaries.

Ashbee and Smallman deformed synthesized TiO_2 in a hard-beam compression machine at atmospheric pressure and 600 to 1300 °C with strain rate 3.4×10^{-4} to 3% axial shortening and found {101}<101> to be the most active slip system, with {110}[001] also active but much less so. They suggested slip on {101}(which is not the shortest lattice vector) is made easier due to pairs of half dislocations, possible in the <101> direction because of interstitial octahedral sites found in this direction, causing lowering of Peierl stresses. Evidence of half dislocations was found in TEM images which showed a combination of partial dislocations and stacking faults. Four different slip systems belong to {101}<101>, and dislocations moving on one {101} plane may become sessile at the intersection with another {101}, e.g. at the intersection of $(0\bar{1}1)$ and $(\bar{1}01)$,leading to strain hardening. However, dislocations moving on {110} planes can overcome these barriers by cross slipping to another {110} plane, e.g. from (110) to $(1\bar{1}0)$. This may explain why {110}[001] is the secondary slip system and becomes active at much higher stress. Blanchin and Fontaine (1975) later confirmed slip in rutile happens dominantly on {101}<101> by motion of edge dislocations. They also found that interaction among the four different {101}<101> slip systems leads to strain hardening as dislocations become sessile at the intersection of different {101} planes. However, unlike Ashbee and Smallman, they did not find evidence of dissociation of <101> dislocations. Blanchin et al. (1980) deformed rutile single crystals oriented for slip on {101}<101> and {110}[001] at 1 atm and a range of temperatures between 800 and 1700 K (and in

oxygen to preserve non-stoichiometry) and again found {101}<101> slip much easier to induce.

Péter et al. (1986) studied the slip systems in paratellurite, TeO_2, a slightly distorted rutile structure (either space group $P4_12_12$ or $P4_32_12$). They calculated the energy of dislocations with <100>, <110>, and [001] Burgers vectors using linear elastic theory of dislocations in anisotropic materials (Hirth and Lothe 1982) and predicted $\{1\bar{1}0\}$<110>, {010}<100>, and (001)<100> to be the most likely slip systems. However their calculations considered only perfect dislocations and did not take possible dissociation into account. They note that [001] dislocations which are dissociated in paratellurite, are perfect dislocations in rutile. They then deformed single crystals oriented with [110], [221], [100], and [001] parallel to compression for a range of temperatures below the melting temperature (733 °C) at 1 atm in an Instron machine up to ~10% strain at strain rates from 3×10^{-5} s^{-1} to 4×10^{-5} s^{-1}. Yield stress of the differently oriented crystals and examination of dislocations with optical microscopy and X-ray topography found slip along (001)<100> to be twice as active as {010}<100> and four times more active than $\{1\bar{1}0\}$<110>.

These studies propose different slip systems which can be used to predict texture development using polycrystal plasticity models. I applied the Los Alamos viscoplastic self-consistent (VPSC) approach for modeling texture (Lebensohn and Tomé 1994). VPSC simulations model deformation of inclusions inside of a homogenous, but anisotropic medium (Eshelby 1957). Deformation (and rotation) of lattice planes inside grain inclusions depends on the relative critical resolved shear stress (CRSS) of slip systems and their orientation relative to the compression direction. Initial crystallographic orientations, crystal symmetry, slip systems (i.e. slip planes with slip directions), and corresponding relative CRSS are defined as input. Because observed texture for quartz was nearly random, an initially random orientation distribution for 2000 grains was assumed. I defined the stress exponent (i.e. the strain rate sensitivity to stress)as $n = 3$, which is typical for minerals deforming in the viscoplastic regime (Wenk et al. 1989a). The displacement gradient tensor was defined as compressive with $\sigma_{11} = \sigma_{22} = -0.5$ and $\sigma_{33} = 1$. Inverse pole figures derived from VPSC simulations (Fig. 5) for the different models show texture at 15% axial shortening, calculated in increments of 1% strain. Estimated CRSS values are shown in Table 2.

Relative CRSS suggested in the studies above and activities resulting from VPSC simulations carried out to 15% strain are summarized in Table 2. I ran VPSC using Cordier et al's (2004) Model 1 slip systems and corresponding relative CRSS, which they estimated using the anisotropic elastic theory of Stroh (1958) for both low pressure (summarized in Table 2) and high pressure, and found that [001] preferentially aligns

nearly perpendicular to the compression direction in either case (Fig. 4). Based on elastic energy calculations for edge dislocations, Texier and Cordier (2006) estimated {100}[001] and {210}[001] dislocations to be two times more favorable than <100> {010}<100>,(001)<100>, and {021}<100> dislocations and at least four times more favorable than <110> dislocations. Relative CRSS for VPSC were assigned accordingly (Table 2).

Table 2. Visco-plastic self-consistent (VPSC) model results for stishovite. Relative critical resolved shear stresses (CRSS) assigned to each slip system based on studies by Cordier et al. (C), Texier and Cordier (T & C), Ashbee and Smallman (A & S), and Péter et al. (P) and slip system activities for uniaxial compression at 15% strain are listed. Slip systems having activities less than 0.01% at 15% strain are not shown.

	Slip sys.	{100} [001]	{010} <100>	(001) <100>	{101} <101>	(001) <110>	{110} [001]	{021} <100>	{1$\bar{1}$0} <110>	{210} <001>
C	*CRSS*	1	—	—	3	—	1	2	3	—
(2004)	*Act(%)*	0.222	NA	NA	0.164	NA	0.223	0.276	0.114	NA
T & C	*CRSS*	1	2	2	—	4	—	2	4	1
(2006)	*Act(%)*	0.302	0.138	0.038	NA	0.011	NA	0.207	0.122	0.181
A & S	*CRSS*	—	—	—	1	—	2	—	—	—
(1962)	*Act(%)*	NA	NA	NA	0.811	NA	0.187	NA	NA	NA
P	*CRSS*	—	4	1	—	—	—	—	5	—
(1986)	*Act(%)*	NA	0.134	0.752	NA	NA	NA	NA	0.103	NA

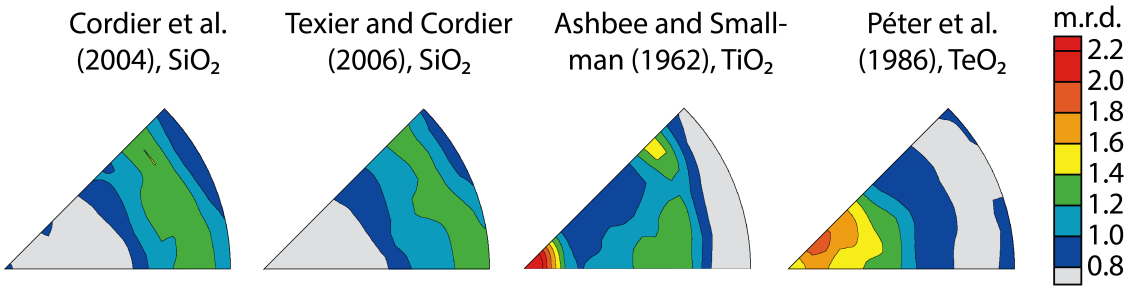

Figure 5. Inverse pole figures depicting texture development during compression to 15% strain from three different VPSC models with slip systems and CRSS suggested by Texier and Cordier (2006), Cordier et al. (2004) for SiO_2, Ashbee and Smallman (1962) for TiO_2, and Péter et al. (1986) for TeO_2. Slip system activities for each model are shown in Table 2. Pole densities are measured in multiples of random distribution (m.r.d.). Equal area projections.

The resulting texture is very similar to that of Cordier et al. (2004), with the compression axis forming a girdle at high angles to the *c*-axis. VPSC results from slip systems suggested by Cordier et al. and Texier and Cordier are both inconsistent with our results (Fig. 3). In contrast, texture obtained from VPSC simulations with slip systems suggested by Ashbee and Smallman (1962) for rutile produced a maximum pole density at 001, with a secondary maximum near 110 (Fig. 5), and closely resemble our results. Relative CRSS shown in Table 2 are based on Ashbee and Smallman's measured CRSS of ~4 kg/mm^2 at 750 °C for a single crystal of rutile oriented for optimal slip on {101}<101>, and 8.8 kg/mm^2 at 850 °C for a crystal oriented for optimal slip on {110}[001]. If secondary slip system {110}[001] is given a higher relative CRSS of 4, making it less active, the secondary maximum at 110 disappears, producing a texture pattern nearly identical to experimental texture at 38 GPa (#172,182 in Fig. 4b). Relative CRSS for easy slip systems in paratellurite (TeO_2) suggested by Péter et al. (1986) are based on their measured CRSS at 600°C and are summarized in Table 2 along with slip activities during VPSC simulations. These slip systems also produced a maximum pole density near 001 (Fig. 5).

Slip system activities proposed for stishovite by Cordier and Sharp (1998), Cordier et al. (2004), and Texier and Cordier (2006) are primarily prismatic and produce alignment of (001) poles perpendicular to compression; slip systems suggested by Ashbee and Smallman (1962) for rutile are pyramidal, and those suggested for paratellurite by Péter et al. (1986) are basal, both of which produce preferential alignment of (001) poles parallel to the compression direction. Pyramidal and basal slip produce the best match with the DAC experiments. This may be because our experiments were done at room temperature, and basal and/or pyramidal slip may dominate in stishovite at low temperatures. Prismatic slip observed by Cordier and Sharp (1998), Cordier et al. (2004), and Texier and Cordier (2006), may be typical of high temperatures.

3.6 Conclusions

Diamond anvil cell experiments were performed in radial geometry while diffraction patterns collected *in situ* to observe crystallographic preferred orientation in stishovite during axial compression. I observed in these room temperature experiments that 001 poles preferentially aligned with the compression direction in stishovite. According to polycrystal plasticity calculations, this is likely due to basal and pyramidal slip rather than prismatic slip as suggested from high temperature studies of dislocations in stishovite. This difference indicates that a variety of slip systems may be active in stishovite, depending on conditions.

Chapter 4

Two phase deformation of lower mantle mineral analogs

4.1 Introduction

While much is known about deformation mechanisms in single phase rocks, deformation of polyphase rocks is largely unexplored. Nearly all of the Earth is composed of polymineral aggregates, including the lower mantle, which is of critical importance for understanding the geodynamic evolution of the planet. Thus far experimental studies of two-phase composites are almost entirely of crustal mineral assemblages (e.g. quartz-muscovite: Tullis and Wenk 1994, Bruhn and Casey 1997; calcite-anhydrite, Barnhoorn et al. 2005; calcite-halite, Covey Crump et al. 2006), with more recent focus shifted to upper mantle assemblages (e.g. forsterite-enstatite, McDonnell et al. 2000; olivine-orthopyroxene, Farla et al. 2013; Tasaka et al. 2013), More rare are studies of deformation in lower mantle mineral composites (e.g. periclase-spinel, Li et al. 2007), very few of which examine crystallographic preferred orientation.

Geodynamic models predict large strains due to convection in the mantle, and polycrystal plasticity simulations based on viscoplastic self-consistent modeling suggest strong preferred orientation (Wenk et al. 2011). However, these models do not take the interaction between different phases into account, which is important for the lower mantle where seismic data and mineral physics estimate a composition of ~25% ferropericlase (Mg,Fe)O and ~70% Mg-perovskite ($MgSiO_3$). (Mg,Fe)O deforms more easily (is "softer") than $MgSiO_3$ (Merkel et al. 2003, Li et al. 2004), making deformation studies of a soft phase-hard phase composite very relevant to the lower mantle. Some studies of such composites suggest that grains of the soft phase become interconnected and act as a lubricant between grains of the harder phase, thereby absorbing most of the deformation and greatly reducing preferred orientation of crystals (e.g. Wenk et al. 2006, Tullis and Wenk 1994, Bons and Cox 1994). In contrast other studies find that the soft phase is not interconnected when present in ~25%, causing deformation to be absorbed by the harder phase (e.g. Madi et al. 2005, Yoshino et al. 2008).

Deformation experiments were performed on two-phase lower mantle mineral analogs in the Deformation-DIA (D-DIA). Because the D-DIA cannot reach lower mantle pressures, analogs halite (NaCl), isostructural to ferropericlase (Mg,Fe)O, and neighborite ($NaMgF_3$), isostructural to Mg-perovskite ($MgSiO_3$) were used. X-ray diffraction patterns were collected *in situ* to observe the development of crystallographic preferred orientation (CPO). In addition, an undeformed and four deformed samples were imaged with X-ray microtomography to relate observed (CPO) to 3D microstructure and help identify active deformation mechanisms. Polycrystal plasticity models were used to estimate slip systems responsible for the observed CPO and the effect of microstructure on stress and strain distribution between the phases.

4.2 Samples

Samples were deformed in the D-DIA at beamline 13-BM-D at the Advanced Photon Source (APS) in Argonne National Laboratory while diffraction patterns were collected *in situ* at moderate temperatures and pressures to collect information about development of CPO and differential stress. In addition, information about the grain structure and distribution of phases in samples, before and after being deformed, was collected using x-ray microtomography at beamlines 2-BM-XOR at APS and 8.3.2. at the Advanced Light Source (ALS) at Lawrence Berkeley National Laboratory.

4.2.1 Analog minerals

Because D-DIA cannot reach lower mantle pressures, low pressure analogues halite (NaCl) and neighborite ($NaMgF_3$) of ferropericlase (Mg,Fe)O and Mg-perovskite ($MgSiO_3$), respectively, were used.

4.2.1.1 Neighborite

Neighborite was first discovered in the Green River Formation in Utah in dolomitic oil shale (Chao et al. 1961), and later in Russia (Efimov et al. 1967). It has a distorted cubic structure characterized by tilting of MgF_6 octahedra and belongs to space group Pbmn. Neighborite was chosen as an analog mineral for perovskite because it is isostructural and isoelectronic (with comparable ionic radii and 1:2 electronic charge ratio for ions) to Mg-perovskite (Chao et al. 1961, O'Keeffe et al. 1979), yet has lower elastic constants (Table 1) and relative critical resolved shear stresses for its slip systems (Table

2) and so deforms more easily at lower pressures than Mg-perovskite. In addition density functional theory calculations (Umemoto et al. 2006) and diamond anvil cell experiments (Liu et al. 2005, Martin et al. 2006) show that $NaMgF_3$ undergoes the same transition to a $CaIrO_3$-type post-perovskite structure as $MgSiO_3$, but at pressures of 19-30 GPa (Umemoto et al. 2006, Zhao et al. 1994) compared to 127 GPa and 2500 K for $MgSiO_3$ (e.g. Murakami et al. 2004, Oganov and Ono 2004, Shim et al. 2004); transitions in both $NaMgF_3$ and $MgSiO_3$ have positive Clapeyron slopes. Calculations (Umemoto et al. 2006) find that at ~40-50 GPa pPV $NaMgF_3$ dissociates into CsCl-type NaF and cotunnite-type MgF_2, just as at 1 TPa Mg-post-perovskite dissociates into CsCl-type MgO and cotunnite-type SiO_2; both dissociations have negative Clapeyron slopes (Umemoto et al. 2006). Phase transitions at high temperature may also be similar. $NaMgF_3$ becomes tetragonal at 760°C and cubic at 900 ± 25°C (e.g. Chao et al. 1961, Lewis and Bright 1971, Zhao et al. 1994, Chen et al. 2005). First principles calculations (Wolf and Bukowinski 1985), the presence of twins in orthorhombic $MgSiO_3$ (Wang et al. 1990), molecular dynamics simulations (Matsui and Price 1991), and X-ray diffraction experiments (Meade et al. 1995) have lead many to suggest that $MgSiO_3$ is tetragonal and cubic at high temperature, as does the mineral perovskite ($CaTiO_3$) (e.g. Wang and Liebermann 1993, Redfern 1996, Matsui et al. 1997, Ashima and Ali 2009).

Deformation mechanics of neighborite (hereafter referred to as $NaMgF_3$) are not well established, and it is unknown whether $NaMgF_3$ is isomechanical to Mg-perovskite. Zhao et al. (1993) found the dominant mechanism for compression in $NaMgF_3$ to be shortening of the octahedral (Mg-F) bond, which is also true for Mg-perovskite. Twinning has been observed in both $NaMgF_3$ (Chao et al. 1961, Wang et al. 2003, Pischedda et al. 2005) and in Mg-perovskite (e.g. Wang et al. 1990, Martinez et al. 1997, Wenk et al. 2004, Auzende et al. 2008), and is commonly produced in perovskite structures, either during a phase transition or by deformation (e.g. Abrahams l97l, Salje 1990, Zhao et al. 1994, Wang et al. 1990). However, deformation is more often accommodated by slip, yet preferred slip systems in $NaMgF_3$ have not been well studied, and it is uncertain whether $NaMgF_3$ and Mg-perovskite deform plastically via the same slip systems. DAC studies of Mg-perovskite suggest $\{110\}<1\bar{1}0>$ slip is active at lower temperatures and (001)[100] slip is active at higher temperatures (Table 2) (e.g. Miyagi 2009, Wenk et al. 2004, 206, Cordier et al. 2004, Miyajima 2009); meanwhile first principle calculations find that (100)[010] slip dominates at lower mantle conditions (Mainprice et al. 2008). In general, deformation behavior in perovskite structures is complex and studies do not see systematic behavior among minerals with a perovskite structure (e.g. $CaTiO_3$: Doukhan and Doukhan 1986, Besson et al. 1996, Li et al. 1996, Miyagi et al. 2009; $BaTiO_3$: Doukhan and Doukhan 1986, Beauchesne and Poirier 1989; $KZnF_3$, Poirier et al. 1983; $SrTiO_3$, Wang et al. 1993; $YAlO_3$, Wang et al. 1999). Results presented later show some similarity

between CPO development in $NaMgF_3$ and Mg-perovskite at moderate pressures and temperatures.

Table 1. Density, ρ (g/cm^3), and elastic constants (in GPa) for MgO and $MgSiO_3$ and their analogs NaCl and $NaMgF_3$ at ambient conditions. $NaMgF_3$ elastic constants are from Zhao et al. (1993). $MgSiO_3$ are from Yeganeh-Haeri and Weidner (1989). MgO and NaCl elastic constants are from Hearmon (1979). Bulk (K) and shear (μ) moduli are Hill averages.

	ρ	C_{11}	C_{22}	C_{33}	C_{44}	C_{55}	C_{66}	C_{12}	C_{13}	C_{23}	K	μ
$MgSiO_3$	4.108	515	525	435	179	202	175	117	117	139	246.4	184.2
$NaMgF_3$	3.058	125.7	147.3	142.5	46.7	44.8	50.4	49.5	45.1	43.1	75.66	46.73
MgO	3.584	294	294	294	155	155	155	93	93	93	160	130.3
NaCl	2.163	49	49	49	13	13	13	13	13	13	24.9	14.7

Table 2. Relative CRSS of $MgSiO_3$, $NaMgF_3$, MgO, and NaCl inferred from CPO observations via polycrystal plasticity simulations. CRSS listed for $MgSiO_3$ and MgO are expected for pressures of >35 GPa obtained in DAC.

Slip systems	(001)[100], (001)[010], (001)<110>	(100)[010], (010)[100]	(100)<011>, (010)<101>		{110} <1$\bar{1}$0>	{111} <10$\bar{1}$>	{100} <011>
$MgSiO_3$	1	3	4	MgO	0.5	0.75	1
$NaMgF_3$	5	0.5	0.5	NaCl	0.25	2.5	3

4.2.1.2 Halite

Halite was chosen as the analog for ferropericlase, because it isostructural and isomechanical to ferropericlase. Both minerals have B1 structure, belonging to space group $Fm\bar{3}m$, at ambient conditions, but convert to B2 ($Pm\bar{3}m$) structure at higher pressures: MgO converts near 611 GPa (Gueddim et al. 2009), FeO, near 230 GPa (Ozawa et al. 2011), and NaCl, near 27 GPa (e.g. Bassett et al. 1968, Li and Jeanloz 1987).

The deformation behavior of halite (e.g. Carter and Heard 1970, Skrotzki and Haasen 1981, Skrotzki and Welch 1983) and ferropericlase (e.g. Day and Stokes 1966, Paterson and Weaver 1970, Srinivasan and Stoeve 1974, Kinsland and Bassett 1977,

Routbort 1979, Stretton et al. 2001, Yamazaki and Karato 2002, Merkel et al. 2002, Uchida et al. 2004, Long et al. 2006, Lin et al. 2009, Carrez et al. 2009, Cordier et al. 2012, Amodeo et al. 2012) have been studied in detail. Table 1 summarizes elastic constants and Table 2, relative CRSS for the different slip systems. In both minerals, the stiffest direction is parallel to the a-axis, and the easiest slip system is $\{110\}<1\bar{1}0>$ with the other slip systems, $\{111\}<1\bar{1}0>$ and $\{001\}<1\bar{1}0>$, being much less active at ambient temperature but becoming increasingly active at higher temperature (e.g. Heidelbach et al. 2003). However, (Mg,Fe)O with low iron content (i.e. ferropericlase) has been observed to preferentially orient with {001} poles parallel to compression (e.g.Tommaseo et al. 2006), while . iron-rich (Mg,Fe)O (i.e. magnesiowüstite) and NaCl may align with either {001} or {101} poles parallel to compression (e.g. Kern and Braun 1973).

In the two-phase system MgO + $MgSiO_3$, MgO is the softer phase with a bulk modulus of about 2/3 that of Mg-pervoskite (Table 1). The analog system NaCl + $NaMgF_3$ is similar in that NaCl is softer than $NaMgF_3$, but the bulk modulus of NaCl is only about 1/3 that of $NaMgF_3$.

4.2.2 Sample preparation

Sintered samples of 100% $NaMgF_3$, 85% $NaMgF_3$, 75% $NaMgF_3$, 70% $NaMgF_3$, 50% $NaMgF_3$, 30% $NaMgF_3$, and 25% $NaMgF_3$ (the remaining percent is NaCl) were prepared in three batches. For all three batches NaCl powder obtained from Alfa Aesar with 99.99% purity was used, and $NaMgF_3$ was prepared by sintering a stoichiometric mixture of NaF + MgF_2 following the procedure of Chao et al. (1961). The first batch was prepared by mixing NaF + MgF_2 powders in a pestle and mortar and heating the mixture in an alumina crucible to 750°C in air for five hours. Diffraction patterns of the resulting $NaMgF_3$ collected at 11-ID-C of the APS show small peaks from an unidentifiable phase. These peaks are seen at $2\theta \approx 4.4°$ and 5.5° in Fig. 1 in a diffraction pattern from the first round of experiments. NaF and MgO peaks are also present in ~1% or less in some diffraction patterns. The $NaMgF_3$ powder (light pink in color) used in the second batch was obtained from David C. Martin was also synthesized using the methods of Chao et al. (1961)and contained no contaminants. For the third batch, NaF and MgF_2 powders were mixed in a pestle and mortar, then heated in a Pt crucible in a vacuum heater backfilled with argon to 750°C for five hours. XRD analysis showed less than 2% of MgO and less than 3% NaF present due to oxygen (despite backfilling the heater with

argon) reacting with Mg from the MgF_2, leaving a small percentage of NaF and F unreacted. However, fluoride burns off and was not found in the samples.

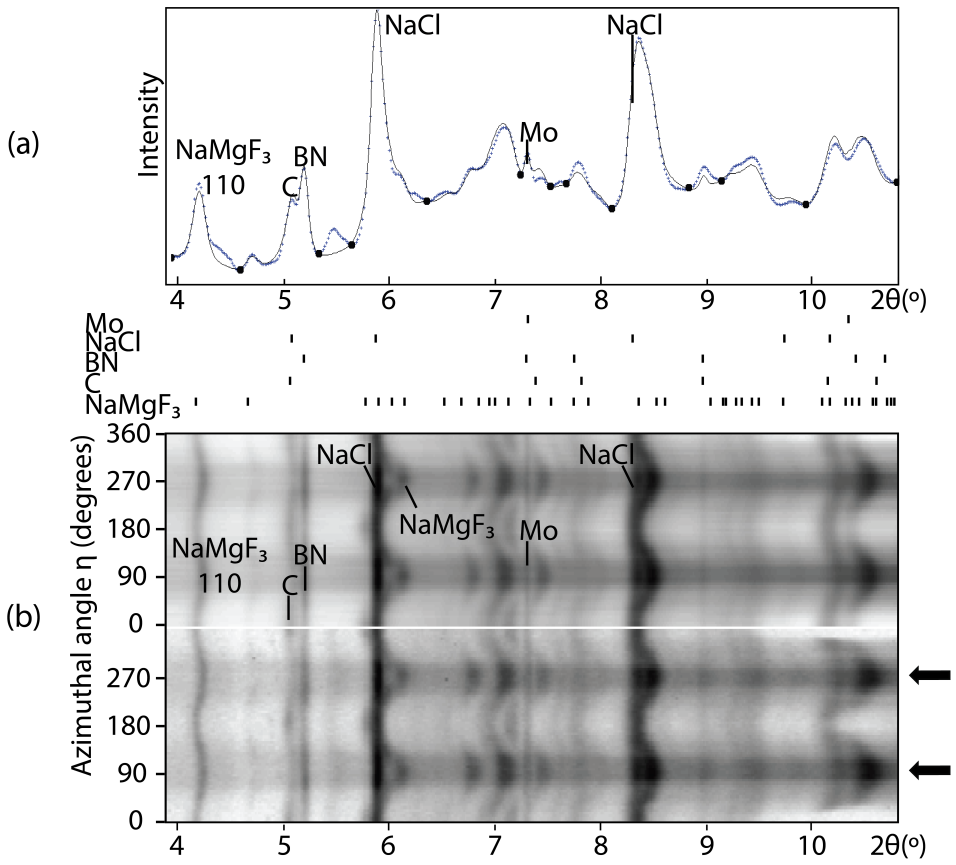

Figure 1. Diffraction pattern of 75% $NaMgF_3$, 25% NaCl collected at 5.1 GPa, 100°C, and 18% strain; (a) data shown with a dotted blue line, and a calculated fit with the solid black line and black interpolation points, (b) unrolled Debye rings, called a 2D plot, with the data shown in the bottom half, and the calculated fit in the top half. Tick marks below (a) denote peaks belonging to each phase listed to the left. Graphite heater (C), boron nitride (BN), and Mo (less than 0.05% volume) peaks are labeled. Peaks near 4.4° and 5.5° are from an identified phase. Multiple planes contribute to most $NaMgF_3$ peaks, and these are unlabeled except for the first peak near 4.1° which is solely from diffraction off the {110} planes.

Sintered cylinders produced in the first two batches were produced by mechanically mixed powders of NaCl and $NaMgF_3$ and compressing them to 3 GPa in a multianvil press in a Mo sleeve at 600°C for 1 hour. Less than 0.05% volume of Mo in was detected in

diffraction patterns, but because it diffracts so strongly, small Mo peaks are visible in diffraction patterns for this batch of samples (Fig. 1). Cylinders 1.2 mm in length and diameter were cut with an ultrasonic cutter. I prepared the third batch of samples (85% $NaMgF_3$) by pressing a mechanically mixed powder of NaCl and $NaMgF_3$ in a die to 0.7 GPa using a press, then heated for four hours at 750 °C at atmospheric pressure in air. I then sanded the sample to size, using a drill press to sand a cylindrical sample while it was spinning.

4.3 Deformation-DIA

4.3.1 Experiments

Samples were deformed in the Deformation-DIA (D-DIA), a multi-anvil press (e.g. Wang et al. 2003). The D-DIA has some advantages over the diamond anvil cell (DAC) for high pressure deformation experiments – it can apply quasi-hydrostatic pressure and uniaxial differential stress separately and deform larger samples, resulting in better counting statistics and the possibility to explore the 3D tomography. However, because of the larger sample size, pressures are limited to 12 GPa (rather than > 200 GPa in DAC), and temperatures are limited to the range obtainable with resistive heating, so up to 2000°C as opposed to 2000 – 4000°C obtained with laser heating. However resistive heating provides more homogenous heating than laser heating, and the temperature is more stable and known with more accuracy.

For deformation experiments, 1.2 mm sample cylinders were loaded into either a BN or an MgO sleeve for insulation, capped with two sets of alumina pistons (hard alumina and crushable alumina), then loaded into a cylindrical graphite heater inside of an amorphous boron epoxy cube 7 × 7 × 6 mm (Fig. 2). Tungsten carbide anvils with 4 mm truncation were used, with the exception of the two anvils on the downstream side, which were made of sintered diamond so as not to block diffracted X-rays from reaching the detector. Diffraction peaks from the insulation sleeve and graphite heater appear in the diffraction patterns (Fig. 1). The D-DIA setup is described in detail in Wang et al. (2003).

Monochromatic X-rays with a wavelength of either 0.248 Å (for the first two rounds of experiments) or 0.225 Å (for second two rounds of experiments) was collimated to a beam size of 200 × 200 μm with two pairs of tungsten carbide (WC) slits and directed through the anvil gaps to the sample. Diffraction patterns were collected on a

Mar-165 charge-coupled device (CCD) for 600 seconds (for a few runs, D1315 300 second or 1000 second exposures were collected) binned to 2048 × 2048 with pixel size 0.0079 mm.

Twelve samples of various volume fractions of $NaMgF_3$ and NaCl were compressed quasi-hydrostatically to 20 tons (~3-5 GPa, depending on sample composition), then compressed non-hydrostatically by advancing the differential rams at an average strain rate of 5×10^{-5} s^{-1} (D1475 and D1476 were done at 4×10^{-5} s^{-1}) which is in the ductile regime. Meanwhile diffraction patterns were collected regularly as pressure and strain increase to observe their effect on differentials stress and CPO. In addition temperature was varied between 25°C and 800°C, and in order to study the effect of temperature.

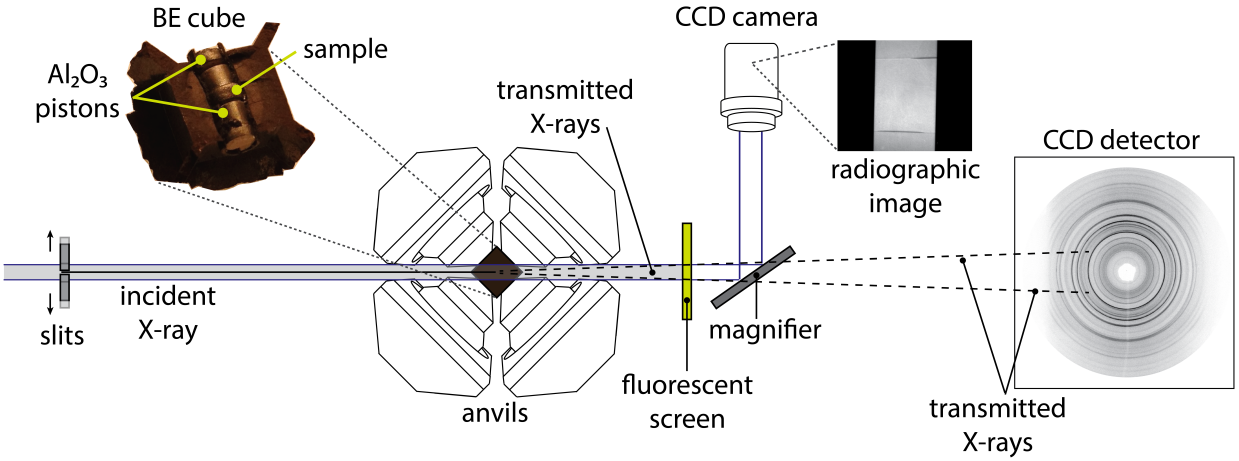

Figure 2. A simple schematic of the D-DIA setup at beamline 13-BM-D. Slits are moved in or out to either allow a bigger beam for X-ray tomography or a smaller beam for X-ray diffraction. The fluorescent screen, magnifier and CCD are moved out of the beam path when collecting diffraction patterns. The sample assemblage, i.e. boron epoxy (BE) cube, alumina pistons and sample, is shown in more detail in the upper left.

During compression, axial shortening of the samples was imaged with X-ray radiography. Two 5 μm thick flakes of Au were placed on the top and bottom of the sample cylinder to provide contrast between the sample and neighboring alumina pistons (CCD camera image in Fig. 2). Axial shortening is defined as standard strain % = $\Delta l / l_0 \times 100$ where l_0 is the sample length after quasi-hydrostatic compression but before deforming. However, in some experimental runs the rams did not advance at the same rate as the load, and the sample was slightly extended. In this case l_0 is the sample length at ambient pressure, before the start of the experiment. In a multianvil press such as D-DIA,

compression is never truly hydrostatic since there is no way to guarantee that all sets of pistons advance at exactly the same rate, thus l_0 is likely measured at non-zero strain in all cases. For softer samples such as NaCl, even a slight deviation from hydrostaticity can cause the sample to strain elastically and plastically. Evidence of this is seen in the Appendix tables where, for many runs, the differential stress (t) and maximum pole density are already high at 0% strain.

4.3.2 Data analysis

Diffraction patterns were analyzed with the Rietveld refinement as implemented in MAUD (Material Analysis Using Diffraction, Lutterotti et al. 1997, Lutterotti et al. 2014, Wenk et al. 2014). Debye rings were unrolled in Fit2D (Hammersley et al. 1996), and diffraction intensity was integrated every 5° in η for a total of 72 spectra (Fig. 1).

Instrument parameters such as image center, detector tilt, and peak shape were calibrated with a CeO_2 standard. Caglioti parameters (Caglioti 1958) were refined to account for peak width and gaussinity caused by instrument broadening. Grain size and root mean square (r.m.s.) microstrain, which also determine peak shape, were fit using the isotropic grain model. However, for multiphase systems under high stress, individual contributions from grain size and microstrain to peak broadening cannot be well constrained resulting in large errors for these values, thus they are not given in the tables in the Appendix.

Unrolled diffraction patterns for five sample compositions shown in Fig. 3. contain peaks from phases $NaMgF_3$, NaCl, graphite (from the heater), and either BN or MgO (from the insulation sleeve). For $NaMgF_3$ the Pbnm structure from Zhao et al. (1994) was used and for NaCl, the structure from Walker et al. (2004) was used. The analysis range was confined to a 2θ range of about 3° to 11° since diffuse peaks from the boron epoxy cube at lower angles and many overlapping peaks at higher angles rendered deconvolution of the texture contribution from each phase less reliable. The greater number of phases, high stresses, and diffuse scattering from the boron epoxy cube created a complicated background that was best fit with an interpolated background. About 15 interpolation points were used to pin the calculated background intensity to the observed background intensity over the 2θ range (see Fig. 1).

Pressures in samples containing NaCl were calculated from the change in volume, i.e. the change in cell parameter a as determined by peak position in 2θ at η = 54.7° (Singh et al. 1998), and the temperature using the BE_2 form from Birch (1986), which

has previously been shown to be in good agreement with other equations of state (e.g. Decker 1971, Dorogokupets 2002). Pressures for samples containing only $NaMgF_3$ were calculated from volume change only, as there are no available equations of state which include temperature; a Birch-Murnaghan isothermal equation of state with $B_0 = 76$ GPa (Liu et al. 2005) and $B_0' = 4$ GPa (Birch 1978) was used. The absolute unit cell volume is difficult to know with high accuracy in D-DIA. The multianvil press sits on a table that is rolled out to load and rolled back into place to begin the experiment. The position of the press and sample relative to the detector may vary by a few mm which can change the radius of Debye rings on the detector and thus peak position from which cell parameters are calculated. The largest error seen for cell parameter *a* of NaCl at ambient conditions was 2.5%.

Sinusoidal variations in peak position with η seen in Fig. 3 are due to lattice strains. Arrows in the top pattern indicate the compression direction at $\eta = 90°$ and $\eta = 270°$. Peaks at these angles have larger 2θ values which are inversely related to *d*-spacings by Bragg's law, $\lambda = 2d\sin\theta$, showing that *d*-spacing is smaller in the compression direction. The differential stress leading to the observed strain is defined as $t = \sigma_{33} - \sigma_{11}$, where σ_{33} is the compressive stress, and due to axial symmetry, $\sigma_{11} = \sigma_{22}$ is assumed. The Moment Pole Stress model in MAUD (Matthies et al. 2001, Wenk et al. 2014) was used to calculate differential stress in NaCl and $NaMgF_3$ from their elastic constants and sinusoidal variations of peak position as a function of η. The BulkPathGeo stress/strain averaging model (Matthies et al. 2001) was chosen, and CPO (also called "texture") was taken into account. No elastic constants of NaCl corrected for both temperature and pressure exist. Because pressure has a much greater effect than temperature, elastic constants of NaCl were determined as a function of pressure by interpolating from data collected by Liu et al. (2010). Elastic constants of $NaMgF_3$ at neither pressure nor temperature have yet been determined, thus C_{ij} at ambient conditions measured by Zhao and Weidner (1993) were used to determine differential stress in $NaMgF_3$ for all pressures and temperatures. While absolute differential stress values may not be accurate because elastic constants were not adjusted for both pressure and temperature, the relative *t* values are still meaningful. Negative differential stress is defined as compressive.

Intensity variations along η in Fig. 3 are due to plastic strain that has induced slip, causing crystal lattices to rotate toward a preferred orientation resulting in higher intensity on Debye rings at corresponding angles along η. CPO was quantified with the E-WIMV algorithm. Due to strong texture and overlapping peaks from the sample minerals, the graphite heater, and insulation sleeve, a resolution of 7.5° was needed for the orientation distribution function (ODF). Cylindrical (fiber) symmetry was imposed for sample texture since it is deformed uniaxialy. The ODF was exported from MAUD, smoothed with 7.5° Gaussian filter, and plotted as inverse pole figures in BEARTEX (Wenk et al. 1998).

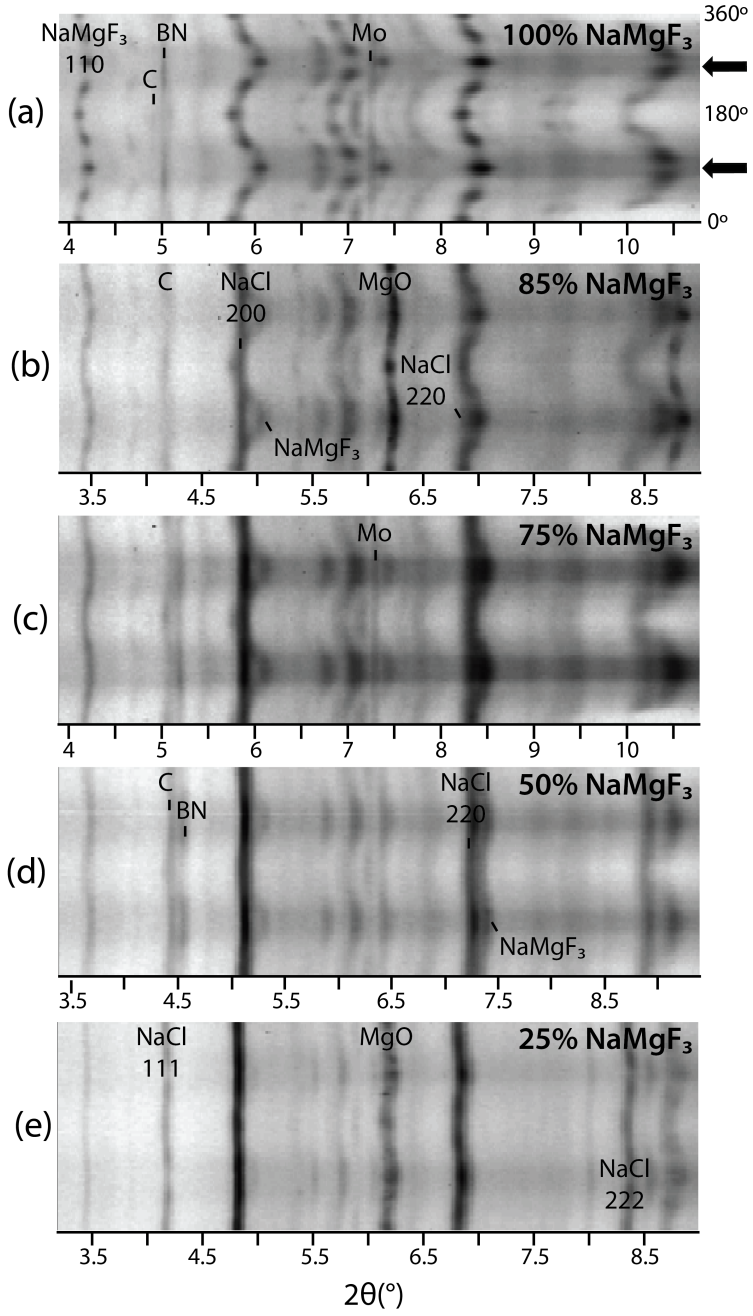

Figure 3. Unrolled diffraction patterns showing variation in peak intensity, indicative of CPO, and variation in peak position, indicative of differential stress for samples at 20 tons (~4 GPa), 100-400°C, and 30% strain with (a) 100% $NaMgF_3$, (b) 85% $NaMgF_3$, (c) 75% $NaMgF_3$, (d) 50% $NaMgF_3$, and (e) 30% $NaMgF_3$. Peaks from the graphite heater (C) and the insulation sleeve, either boron nitride (BN) or MgO are labeled. NaCl peaks are labeled as well in (b) and (e). The first $NaMgF_3$ peak, 110, is labeled, however, because diffraction from multiple $NaMgF_3$ planes contribute to each of the other peaks, these are not labeled. Unlabeled peaks are $NaMgF_3$. A small peak from Mo contamination from the crucible (mentioned in Sample preparation section) is also seen. Compression direction is labeled with arrows in (a).

4.3.3 Results

Raw unrolled diffraction patterns (Fig. 3) collected at 20 tons (~4 GPa), 100-400°C, and 30% strain for five samples with varying phase volume fractions indicate that differential stress and CPO in $NaMgF_3$ is greatly reduced with just 15% volume fraction of NaCl. Differential stress is very high and CPO is very strong in the 100% $NaMgF_3$ phase (Fig. 3a). Addition of 15% NaCl greatly reduces both (Fig. 3b). Increasing volume

fractions of NaCl further reduced CPO and differential stress in $NaMgF_3$ (Fig. 3c, d, and e). Meanwhile, the NaCl peaks remain relatively straight and uniform in intensity. Although $NaMgF_3$ and NaCl are subjected to the same bulk strain, $NaMgF_3$ has higher differential stress than NaCl because it is stiffer than NaCl. As stress builds in $NaMgF_3$, it begins to deform plastically, initiating slip. On the other hand, NaCl has lower elastic constants and experiences less stress than $NaMgF_3$ until NaCl volume percent reaches 70% (Fig. 3e), where NaCl peaks become slightly wavy (differential stress) and acquire some variation in intensity (texture).

Texture seen in Fig. 3 is quantified with an orientation distribution function (ODF) and represented in inverse pole figures (IPFs). In IPFs the compression direction is mapped relative to the poles to crystallographic planes in a 2D stereographic (equal area) projection. The density of these poles is given in multiples of a random distribution (m.r.d.) where an m.r.d. = 1 indicates no preferred orientation. Fig. 4 shows a subset of IPFs corresponding to the 2D plots shown in Fig. 3. A complete set of IPFs for the 12 experimental runs is given, along with corresponding maximum and minimum m.r.d., in the Appendix.

4.3.3.1 Neighborite

$NaMgF_3$ develops a pole density maximum at (100) in the inverse pole figures for all compositions (Fig. 6), indicating that (100) lattice planes preferentially align perpendicular to the compression direction. In the 100% $NaMgF_3$ samples, the (100) maximum extends up toward (010). This maximum is seen progressively less in 85%, 80%, and 75% $NaMgF_3$ compositions. For all compositions, though more so for higher $NaMgF_3$ content, a small secondary maximum is seen at (001). Samples inadvertently deformed in extension developed a maximum at (010), but there are too few data points taken in extension for further discussion.

The strength of the (100) maximum in the inverse pole figures depends on many variables. Fig. 5 plots the relationship between strain % (x-axis), maximum pole density of $NaMgF_3$ (y-axis), composition (marker colors), and temperature (marker shape) for data points taken at 20 tons (or equivalently ~4 GPa). The most striking trend in the plot is the vertical color distribution, which denotes a strong correlation between texture strength in $NaMgF_3$ and volume fraction. This can be confirmed by a cursory comparison among the inverse pole figures for different compositions in Fig. 4 or in the Appendix. Samples containing only $NaMgF_3$ (red markers) developed very strong preferred orientation. In the experimental run with higher average temperatures (red triangles), the maximum pole density for inverse pole figures was, on average, 5.88 m.r.d., and in the experimental run

with lower temperatures (red circles), the average pole density maximum was 7.98. m.r.d. In comparison, $NaMgF_3$ in samples which contained ~15% NaCl (orange markers) developed average pole density maximums of 4.60 m.r.d. and 4.67 m.r.d.; the average max pole density in the 20% NaCl sample (yellow markers) is not much different (4.73 m.r.d.). Increasing NaCl volume percent to 25% (green markers) reduced the average maximum pole density to 4.00 m.r.d. and for 50% and 70% NaCl (blue markers), average pole densities are near ~3.00 m.r.d.

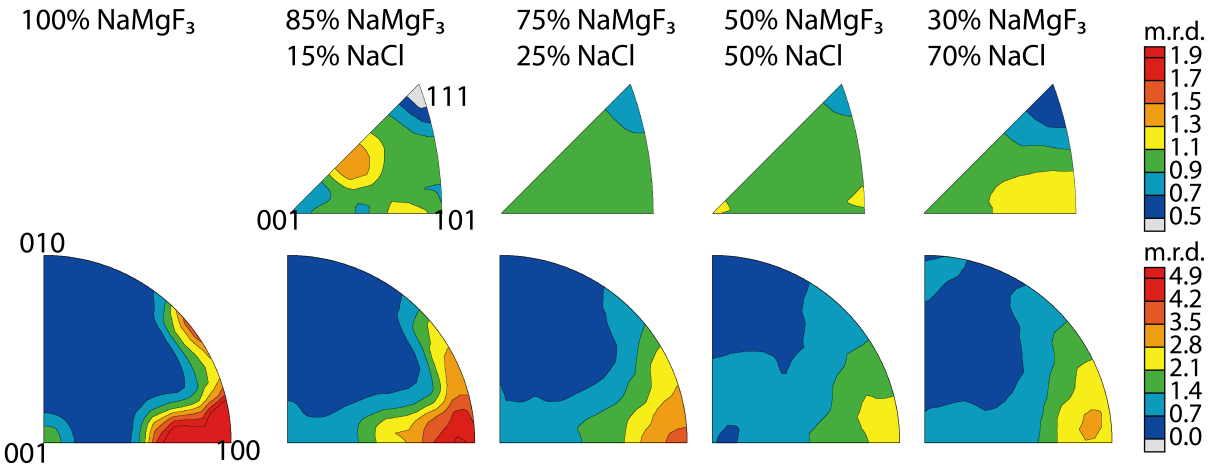

Figure 4. IPFs corresponding to 2D plots shown in Fig. 5. Major crystallographic directions are labeled for both phases. For all compositions, pressure was ~4 GPa, temperature was 100-400°C, and strain was ~30%. Pole densities are indicated by color and given in multiples of random distribution (m.r.d.). An m.r.d. of 1 indicates random orientation. Equal area projections.

Fig. 5 also shows that the maximum m.r.d. increased with strain up to ~15% in the 85% $NaMgF_3$ and 75% $NaMgF_3$ samples. For compositions 80% $NaMgF_3$, 50% $NaMgF_3$, and 30% $NaMgF_3$, the samples were already under some strain due to differential rams advancing slightly faster than the load, and so acquired texture before 20 tons was reached and do not develop stronger texture with further strain. Only texture in the 100% $NaMgF_3$ samples increased beyond 15% strain, where the maximum m.r.d. increased from 5.00 to 6.63 m.r.d. with a 50% strain increase in the higher temperature run (red triangles), and from 6.02 to 12.15 m.r.d. with a 34% strain increase in the lower temperature run (red circles).

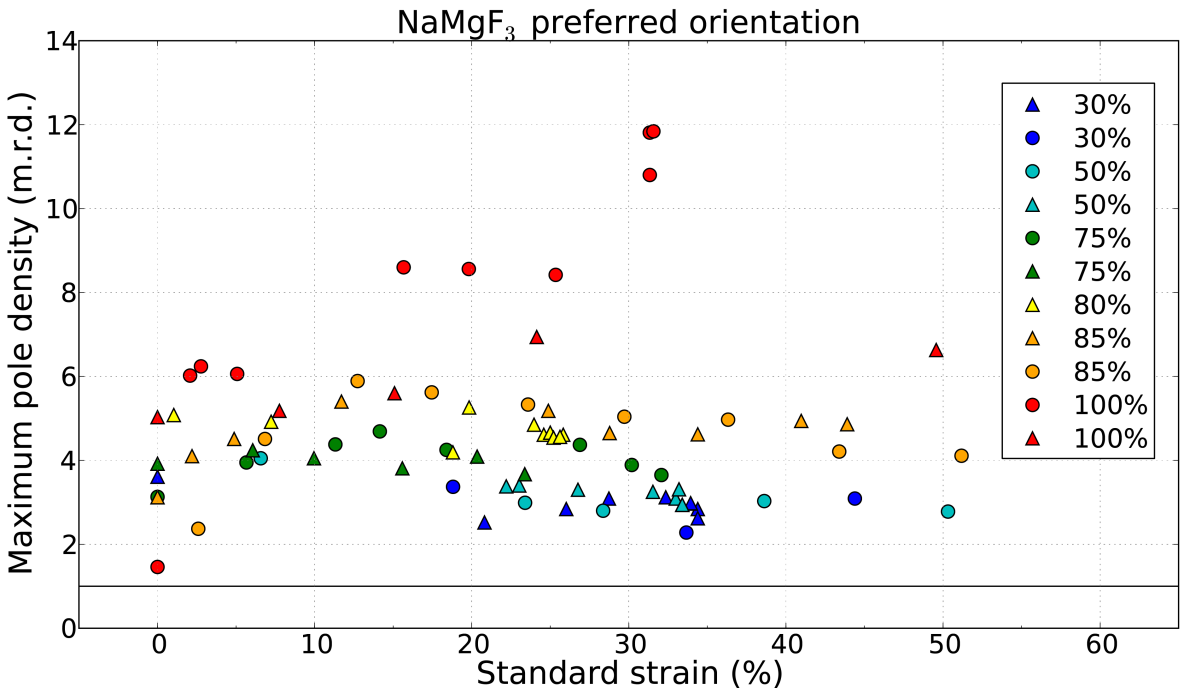

Figure 5. Scatter plot summarizing results shown in IPFs in the Appendix. Texture strength (maximum pole density of IPFs) is plotted as a function of axial shortening (standard strain). The results from eleven experimental runs are plotted with composition indicated by colors. All but one composition was deformed twice, once at higher average temperature (triangle markers) and one at lower average temperature (circle markers). Only data for samples at 20 tons (~3 GPa) are plotted here. Standard strains, maximum pole densities, temperatures, and exact pressure for each data point are shown in tables in the Appendix.

Two runs were done for most sample compositions, one at higher temperature, and one at lower temperature. Data points collected during experiments with higher average temperature are plotted with triangles while their lower temperature counterparts are plotted with circles in Fig. 5. Generally triangles of a given color plot just barely below circles of the same color showing that texture strength is slightly less at higher temperature. However, the difference is quite pronounced for 100% $NaMgF_3$ for which the average maximum m.r.d. during the lower temperature (200 °C) run is 7.98 m.r.d., while for the higher temperature run (400 °C), average maximum m.r.d. is 5.88 m.r.d. With addition of 15% NaCl, the difference in texture strength with temperature is already greatly reduced: the average maximum m.r.d. for 200 °C is 4.67 m.r.d., and for 400 °C, 4.60 m.r.d. For samples with 25% NaCl, the difference is also nearly negligible, and for 50% NaCl and 30%, some triangles plot above some circles.

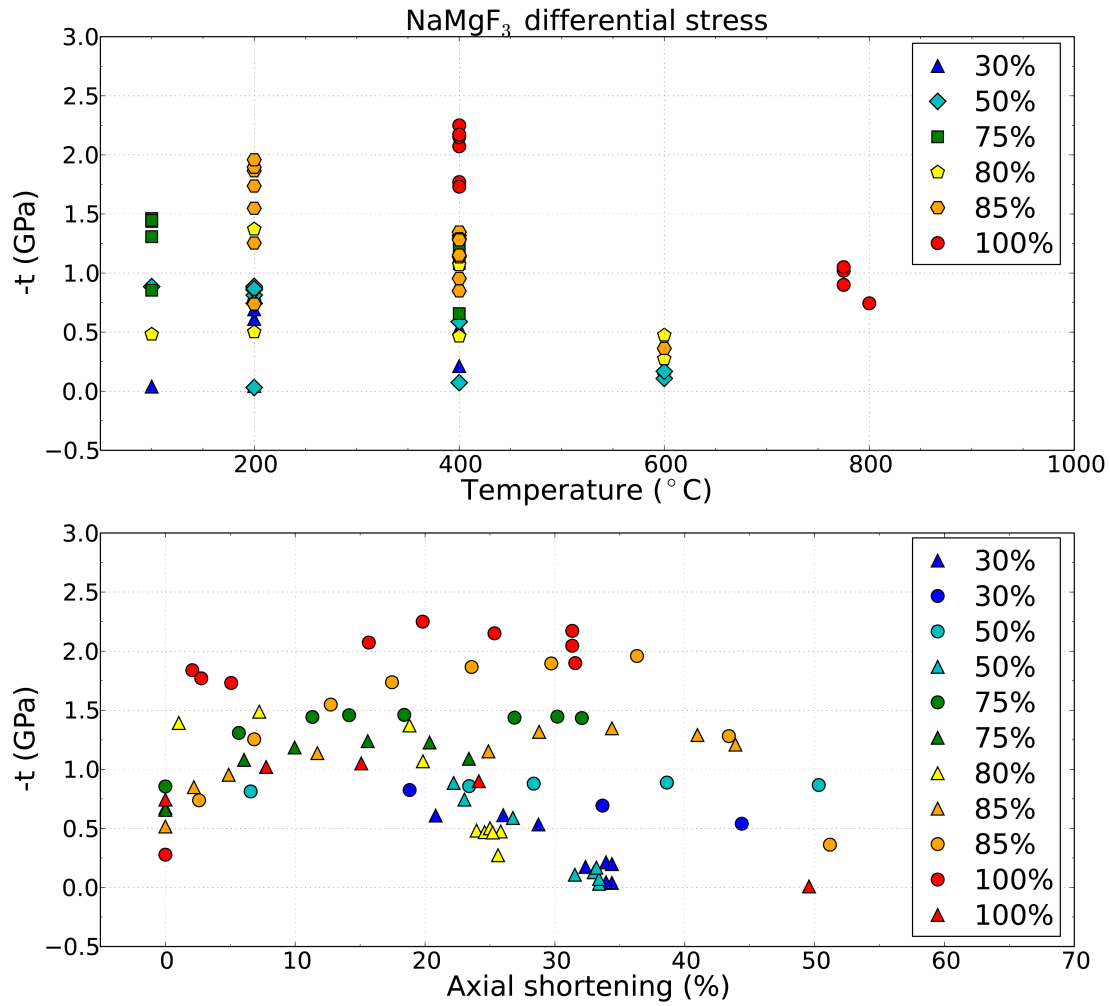

Figure 6. Scatter plot of temperature (top) and standard strain (bottom) and versus differential stress (-t). The y-axis is shown as $-t = (\sigma_{11} - \sigma_{33})$ rather than $t = (\sigma_{11} - \sigma_{33})$ to more intuitively show the relationship between stress and strain. Compositions are indicated by marker color (which corresponds to compositions shown in Fig. 5) and shape. All data points shown were collected at 20 tons during sample compression.

Temperature has a greater effect on differential stress. Fig. 6 (top) shows a plot of temperature versus differential stress; marker colors indicate composition and correlate with colors in Fig. 5. Differential stress decreases with increasing temperature for a given composition. For example, stress in the 100% $NaMgF_3$ sample decreased by ~50% when the temperature was raised by 400°C; a similar relationship between stress and temperature is observed for the other compositions as well. Since the differential stress is not initially as high for compositions containing NaCl, stress is not reduced as much during a temperature increase.

Differential stress also depends on composition. The 100% $NaMgF_3$ sample acquires the highest stress, -2.25 GPa (Appendix) that decreases in magnitude to -2 GPa for 85% $NaMgF_3$, -1.49 for 80% $NaMgF_3$, -1.5 for 75% $NaMgF_3$, and less negative than -1 for 50% $NaMgF_3$ and 30% $NaMgF_3$ samples. Differential stress does not increase much for any composition beyond 15-20% strain (Fig. 6, bottom).

4.3.3.2 Halite

NaCl texture is more irregular and much weaker than $NaMgF_3$ texture (Fig. 4). The maximum pole densities for NaCl in samples containing 15% NaCl and 20% NaCl lie near (112) and (101), with pole densities being weaker in the 20% NaCl sample. At 25% NaCl volume fraction, pole density maxima at (112) have shifted towards (001), and for 50% and 70% NaCl, the maximum pole density for samples in compression is found at either (001) or (110). A few NaCl samples deformed in extension have a maximum at (111) as seen in the Appendix, particularly for run D1186.

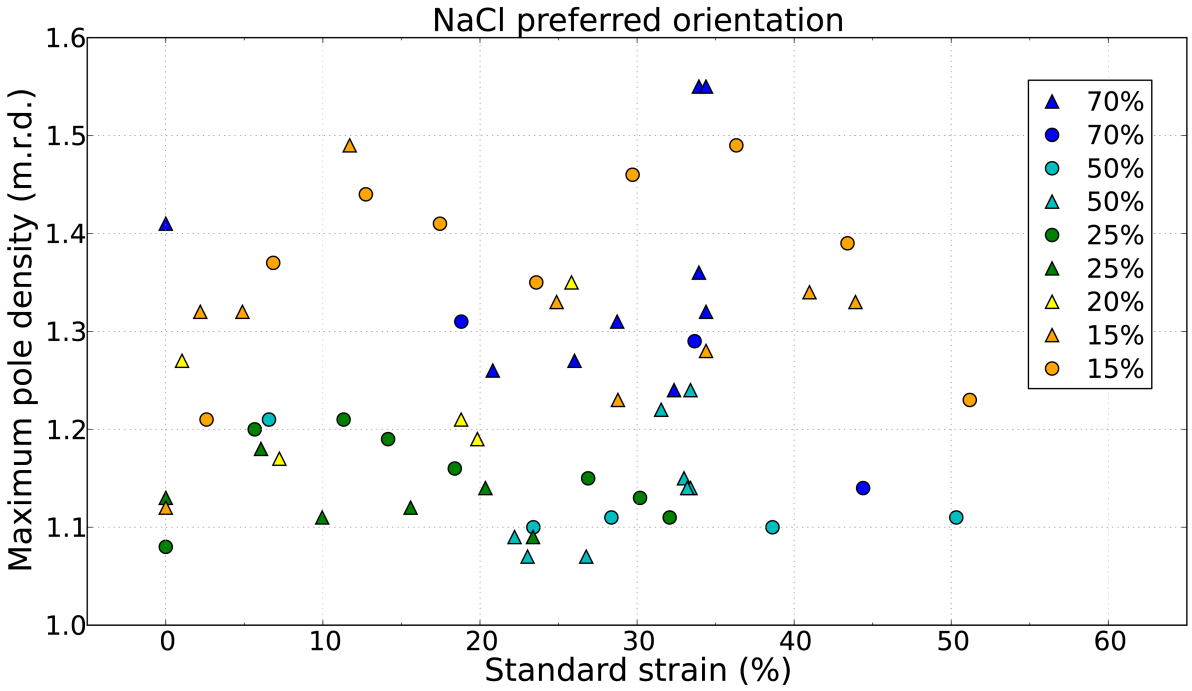

Figure 7. Maximum pole density versus axial shortening (standard strain). Composition indicated by colors. Runs done at higher average temperature are plotted with triangles, and lower average temperature, with circles. All points plotted were collected at 20 tons. Standard strains, maximum pole densities, temperatures, and exact pressure for each data point are shown in tables in the Appendix.

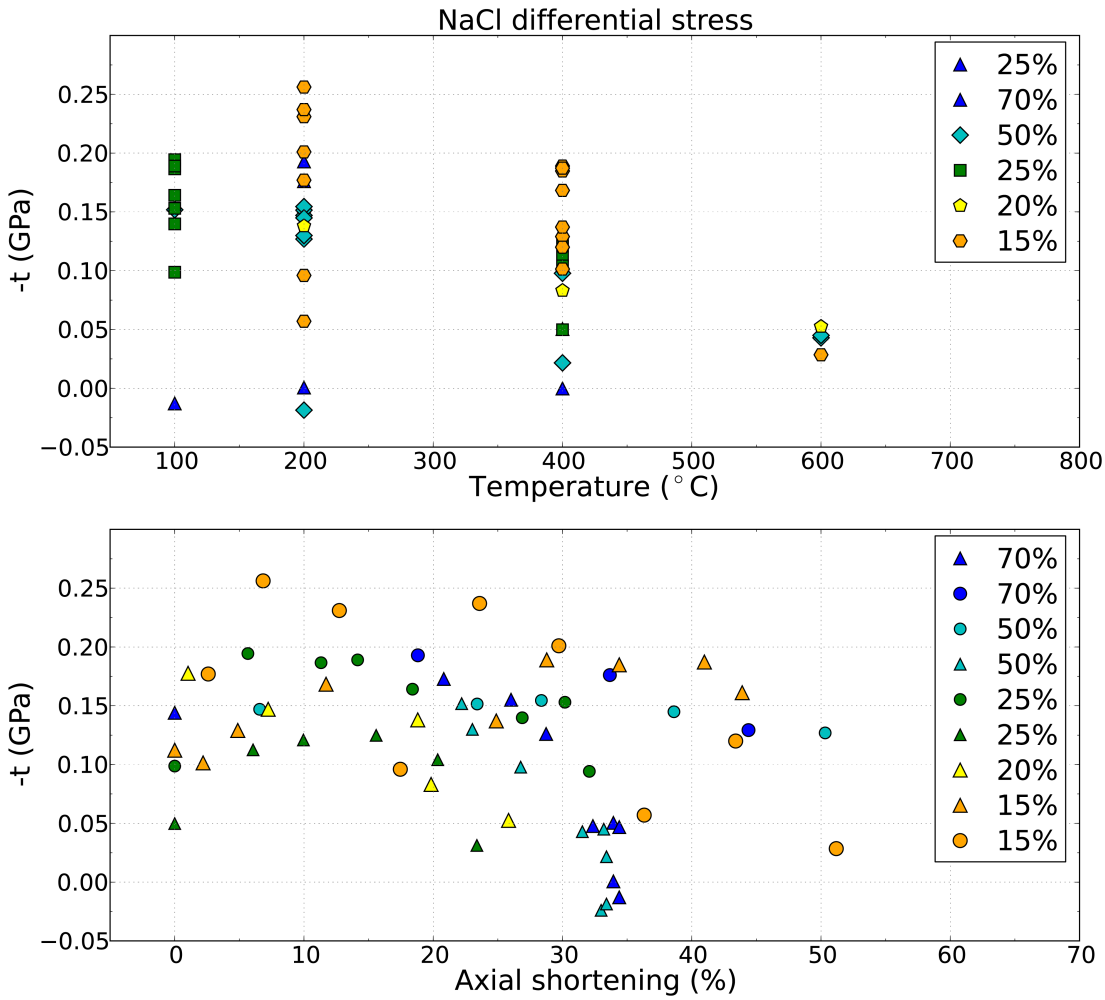

Figure 8. Scatter plot of temperature (top) and standard strain (bottom) versus differential stress in NaCl with sample compositions indicated by color marker and shape.

Fig. 7 shows the effects of percent strain, composition, and temperature on preferred orientation in NaCl. Maximum pole densities in NaCl never reached more than 1.56 m.r.d., compared to 11.84 m.r.d. for $NaMgF_3$, so nearly an order of magnitude less. Unlike for $NaMgF_3$, the relationship between maximum pole density and content is not very strong as seen by the scattering of markers with different colors. Still there is some correlation. Inverse pole figures for samples with the most NaCl (70% NaCl, dark blue) have an average pole density maximum of 1.31 m.r.d. Samples with 50% (light blue) and 25% NaCl (green) both have lower average pole density maxima of 1.14 m.r.d. However, the samples with the least amount of NaCl, 20% (yellow) and 15% NaCl (orange) have higher maximum pole densities on average: 1.24 m.r.d. and 1.34 m.r.d., respectively, likely due to strain heterogeneity which is later discussed. Neither strain % nor temperature

(data from lower temperature runs plotted with a circle, higher temperatures plotted with a triangle) appear to correlate with pole densities in NaCl.

The maximum differential stress reached in the NaCl was -0.26 GPa, so like texture, nearly an order of magnitude less than the maximum for $NaMgF_3$, which was -2.25 GPa. While this is very little stress, trends similar to those seen in $NaMgF_3$ are also seen for NaCl. Fig. 8 plots differential stress as a function of temperature with composition indicated by marker color and shape. Differential stress decreases in NaCl with increasing temperature. As for $NaMgF_3$, stress in NaCl is lowest in samples with the greatest percent volume of NaCl. Differential stress peaks at 15% strain (Fig. 8, bottom).

4.4 Microtomography

Microstructure greatly influences which deformation mechanism dominates and thus the development of CPO. Specifically, the degree to which each phase is interconnected, and whether softer NaCl lies in between harder $NaMgF_3$ grains, will determine which phase absorbs most of the deformation and controls the rheology (Herwegh et al. 2011, Tasaka et al. 2013, Farla et al. 2013). Grain size (Twiss 1977, Frost and Ashby 1982, ter Heege et al. 2002, Li et al. 2007, Tasaka and Hiraga 2013), grain shape (e.g. Dawson et al. 1994), and grain clustering (Brechet 1994) also effect deformation.

4.4.1 Experiments

Phase connectivity and distribution of one undeformed sample and four deformed samples recovered from the D-DIA were quantified using microtomography at beamline 8.3.2 of the ALS and beamline 2-BM of the APS. Microtomography is a form of phase contrast imaging that uses high-intensity X-rays to render a 3D reconstruction of a sample without damaging it. The amount of light transmitted during imaging depends on the absorption coefficient of each phase in the sample and on the sample length in the path of the X-ray (Beer-Lambert's Law). A more detailed discussion of X-ray microtomography for 3D imaging of multiphase rocks and comparison between facilities at APS and ALS is given in Kanitpanyacharoen et al. (2013). Details of the procedures used in these experiments are given below, and a schematic of the general setup at microtomography beamlines is shown in Fig. 9.

Microtomography data for most samples was collected at beamline 8.3.2. of the ALS. A monochromatic X-ray beam with energy 20 keV and size 40 mm × 4.6 mm was

focused on the sample. Sample cylinder axes were positioned vertically on a mounting needle using a small piece of clay. The mounting needle was attached to a rotation stage, and the samples were centered on the axis of rotation. Images were collected every 0.088° from 0 - 180° for a total of 2049 images. Either a 50 μm thick scintillator cut from a single-crystal of cerium doped with lutetium silver (LuAg:Ce) or a 20 μm thick scintillator cut from a cerium crystal doped with yttrium aluminum garnet (YAG:Ce) converted transmitted X-rays to visible light. An Optique Peter mirror objective was used. An Olympus lens magnified the light 10× resulting in a pixel size of 0.65 μm. Images were collected for 1500 seconds on a 16-bit sCMOS PCO.edge camera with a resolution of 2560 × 2160. To correct for inhomogeneous illumination, 40 bright field images were taken during full illumination by the X-ray beam, with no sample in the field of view, both before and after images were collected, and 40 dark field images were taken with no X-ray beam after images were collected. Details of the setup at beamline 8.3.2. are found in MacDowell et al. (2012).

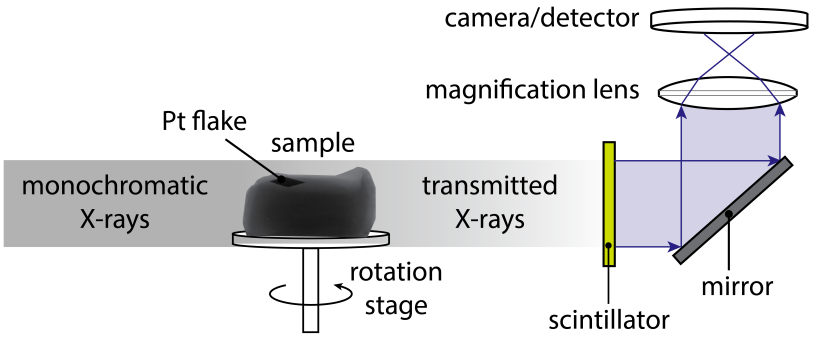

Figure 9. An illustration of the general setup at tomography beamlines 8.3.2. and 2-BM-B. The Pt flake (labeled) used for contrast in radiographic images during D-DIA experiments often became encrusted on the samples.

The setup of 2-BM-B at APS is similar. The X-ray beam had energy 17 keV and size 25 mm × 4 mm. Images were collected every 0.120 ° from 0 – 180° for a total of 1500 images. A single-crystal lutetium aluminum garnet doped with cerium (LuAG:Ce) scintillator converted transmitted X-rays to 535 nm wavelength light which was magnified with a Zeiss Axioplan 5× magnification lens, giving a pixel size of 1.43 μm. Images were collected on a 14-bit CCD with a resolution of 2048 × 2048 pixels for 200 seconds. After sample images were collected, 40 bright field images and 40 dark field images were collected. Details of the setup at beamline 2-BM-B are found in Wang et al. (2001).

4.4.2 Data analysis

Tomographic projections collected at beamline 8.3.2 of the ALS were output in Tagged Image Format (TIF) format, while images collected at 2-BM-B at APS were output as Hierachical Data Format (HDF) and were converted into TIF format before reconstruction using a Matlab code. Steps taken to reconstruct projections into a 3D image are shown in Fig. 4. Sample projections (Fig 10a) were corrected for heterogeneous illumination by dividing the difference between the sample images and the dark field images by the difference between the bright field images and the dark field images (Wang et al. 2001) with *Image J* software. Using the *Octopus* software (Dierick et al. 2004), the corrected projections were normalized to the average value in a selected region of interest with no sample where 100% X-ray transmission is assumed. The transmission intensities of the projections are reorganized into sinograms (Fig. 10b). Defects or dust on the scintillator will create ring artifacts after processing into sinograms, thus a ring removal filter was applied. Prior to creating reconstructed slices from the sinograms, the center of rotation was determined by comparing the images taken at 0° and 180°. In addition the grayscale range was adjusted so that the intensity range of the pixels in the sample just fit inside that range in order to optimize contrast. Approximately 1200 slices perpendicular to the compression direction were created from reconstruction of the sinograms. A reconstructed slice is shown in Fig. 10c.

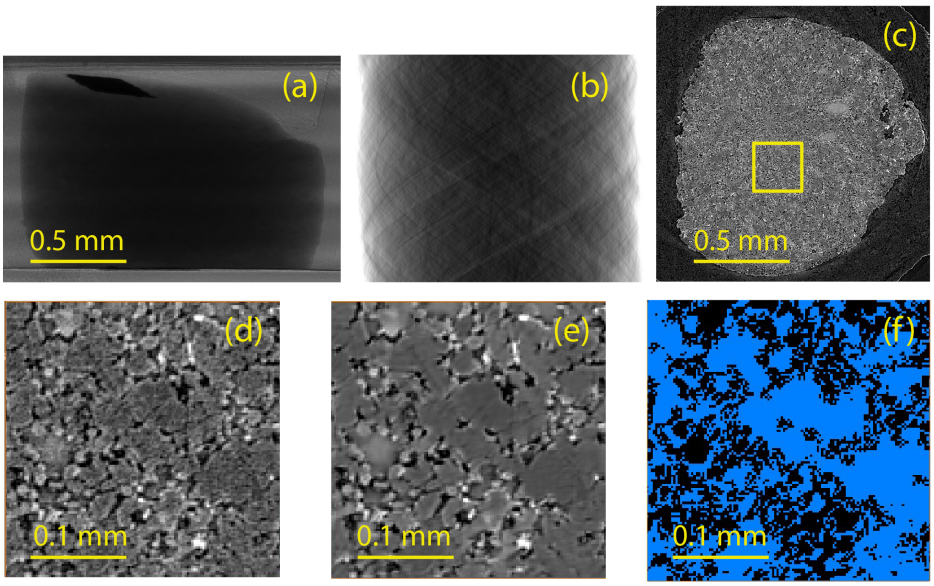

Figure 10. Steps in microtomography data analysis: (a) raw transmission image, (b) sonogram, (c) reconstructed slice, (d) selected subsection, (e) smoothing, (f) $NaMgF_3$ threshold. The square in (c) corresponds to the entire area shown in (d).

Processing, statistical analysis, and visualization of reconstructed slices was done in Avizo Fire 3D Analysis Software for Materials Science (Visualization Sciences Group, Massachusetts, USA). Slices are imported into Avizo Fire and stacked to render a 3D image. In order to ease processing load, a 500 × 500 × 500 voxel subvolume for each sample was selected and processed (Fig. 10d). At this scale, the sample is mostly homogenous and statistics from these subsections are expected to be representative of the whole sample. A non-local means algorithm used to reduce noise (Fig. 10e). Next each phase was thresholded by selecting its intensity range (Fig. 10f).

4.4.3 Results

The spatial distribution of phases, grain cluster size distributions, and aspect ratios were quantified with X-ray microtomography for one undeformed sample with composition 75% $NaMgF_3$ and four deformed samples with compositions 80% $NaMgF_3$, 75% $NaMgF_3$, 50% $NaMgF_3$, and 30% $NaMgF_3$. Volume percentages of both phases after thresholding are consistent with volume percents seen with X-ray diffraction.

Cross sections perpendicular to the compression direction for each of the four deformed samples are shown in Fig 11. Both $NaMgF_3$ and NaCl grains form clusters. The 75% $NaMgF_3$ (b), 50% $NaMgF_3$ (c), and 30% $NaMgF_3$ (d) all have similar microstructures with clusters of the NaCl grains (lighter gray) surrounding harder $NaMgF_3$ grains (darker gray). The microstructure of the 80% $NaMgF_3$ (a) sample is very different from the other three with NaCl grains clustering more tightly, leaving larger volumes of $NaMgF_3$ without any NaCl neighbors.

Fig. 12 displays a 3D reconstruction of a deformed sample with 75% $NaMgF_3$ made by stacking slices similar to those shown in Fig. 11. Clusters of $NaMgF_3$ grains are shown in green, and clusters of NaCl grains are shown in blue. The grain clusters are shortened in the compression direction and elongated perpendicular to it. The blue NaCl appears to fill in between the green $NaMgF_3$ grain clusters.

With phase contrast imaging, individual grains are difficult to discern from their neighbors if they are of the same mineral, and therefore transmit the same amount of light. Therefore when analyzing images like those shown in Fig. 11 and Fig. 12, statistics shown are not counting "grains" but actually clusters of grains. Grain statistics find that both $NaMgF_3$ and NaCl in all samples measured and analyzed so far have one very large interconnected cluster of grains. These grain clusters are 2×10^6 to 2×10^7 μm^3 in volume

and comprise most of the total phase volume in the measured volume, signifying that both phases are highly connected.

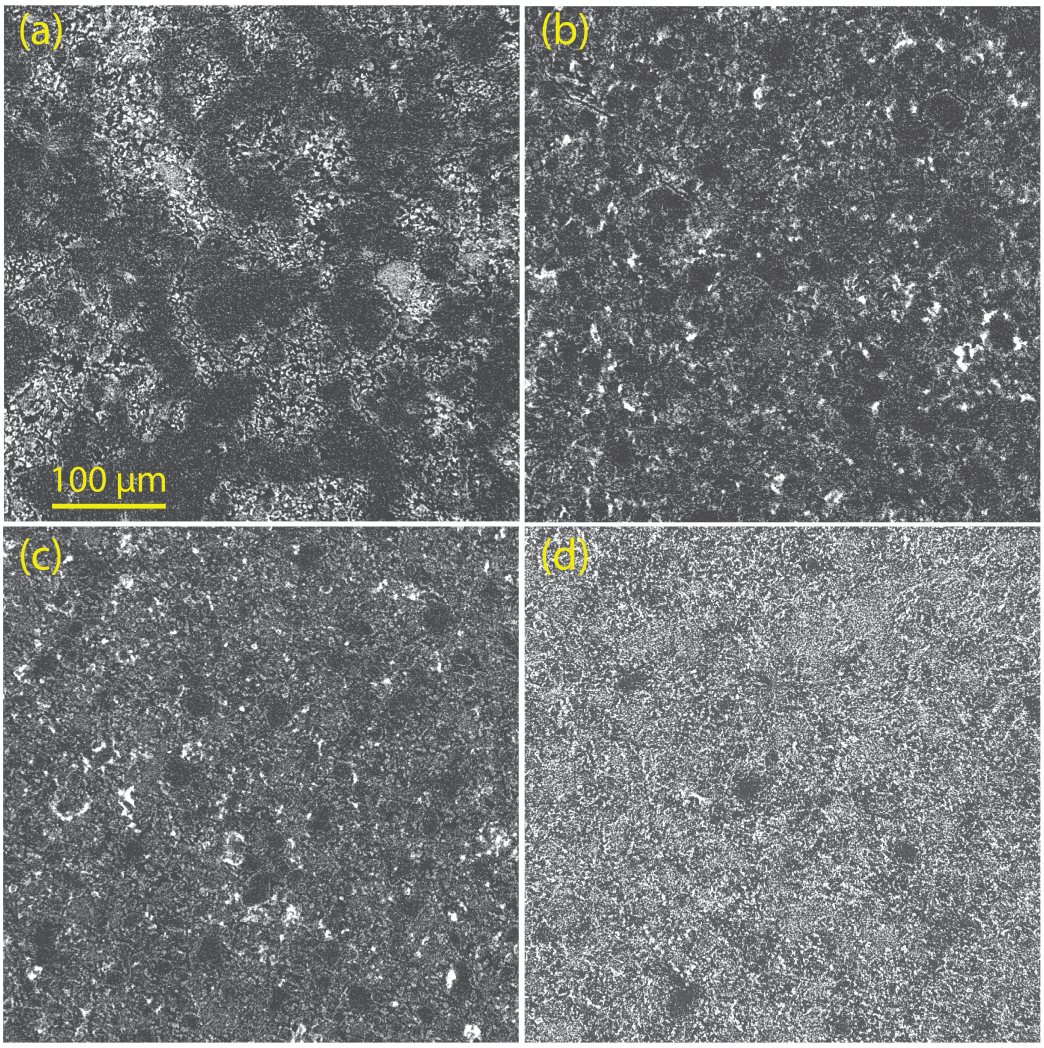

Figure 11. Cross sectional slices of four deformed samples with compositions (a) 80%, (b) 75%, (c) 50%, (d) 25% $NaMgF_3$. Darker gray grains are $NaMgF_3$.

Median grain cluster size and degree of connectivity for $NaMgF_3$ and NaCl in the five samples are shown in Table 3. Connectivity is defined here as the percent of the total phase volume contained in the largest, interconnected cluster of grains. Grain clusters that are not part of this interconnected network are very small and for most compositions make up less than 1% of the total volume. An appreciable decrease in connectivity does not happen for either $NaMgF_3$ or NaCl until their volume fraction in the aggregate drops

below 50%. NaCl is unexpectedly less connected in the 25% NaCl sample than in the 20% NaCl sample likely due to clustering of NaCl into large branches rather than a thin network of veins as in the 25% NaCl sample (Fig. 11). Comparison of statistics for the undeformed and deformed 75% $NaMgF_3$ samples shows that while connectivity of $NaMgF_3$ remained constant during deformation, connectivity of NaCl decreased. This may be because NaCl squeezed in between $NaMgF_3$ grain clusters in the planes perpendicular to compression and became less connected in the compression direction.

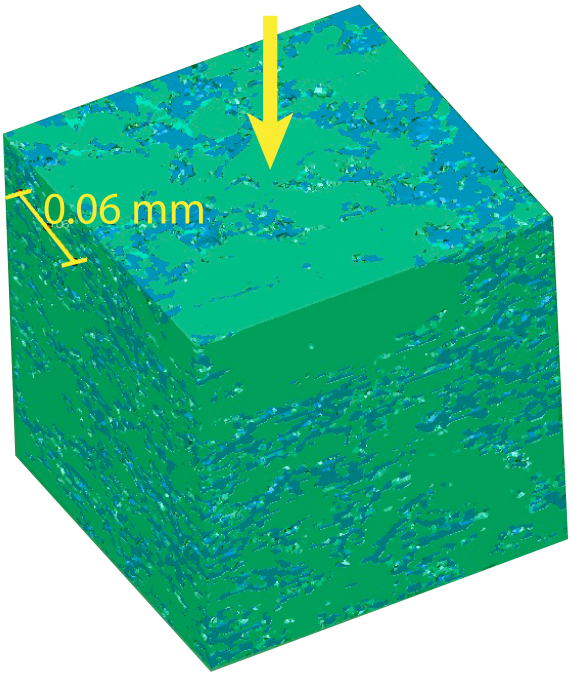

Figure 12. The compression direction is indicated by the arrow, and $NaMgF_3$ grains (green) and NaCl grains (blue) are elongated in the plane perpendicular to the compression direction.

Table 3. Statistics for NaMgF3 and NaCl from microtomography analysis. Connectivity is the percent of the total volume contained in the largest clump of grains. Aspect ratio is the ratio of the longest dimension of a grain cluster in 3D to the shortest dimension. The first column in italics are statistics for the undeformed sample.

NaCl	*25%*	20%	25%	50%	70%
Median cluster volume (μm^3)	*1.61*	1.37	3.02	3.02	1.92
Average aspect ratio	*1.60*	2.79	3.20	3.29	3.10
Connectivity (%)	*99.09*	98.37	95.60	99.79	99.98

$NaMgF_3$	*75%*	80%	75%	50%	30%
Median cluster volume (μm^3)	*0.80*	1.37	1.65	3.30	3.30
Average aspect ratio	*1.25*	2.63	2.85	3.47	3.61
Connectivity (%)	*99.98*	99.95	99.98	99.71	96.25

Disconnected clusters, which make up less than 5% of the total volume for either phase, are very small – approximately 1-15 μm^3. Fig. 13 shows the grain size distribution for $NaMgF_3$ and NaCl in an undeformed sample with 75% $NaMgF_3$, and in deformed samples of 80% $NaMgF_3$, 75% $NaMgF_3$, 50% $NaMgF_3$, and 30% $NaMgF_3$. The undeformed sample contains more grains of the smallest size than the deformed samples indicating that grains of the same phase clustered together during deformation but not to great enough extend to noticeably increase connectivity (Table 3).

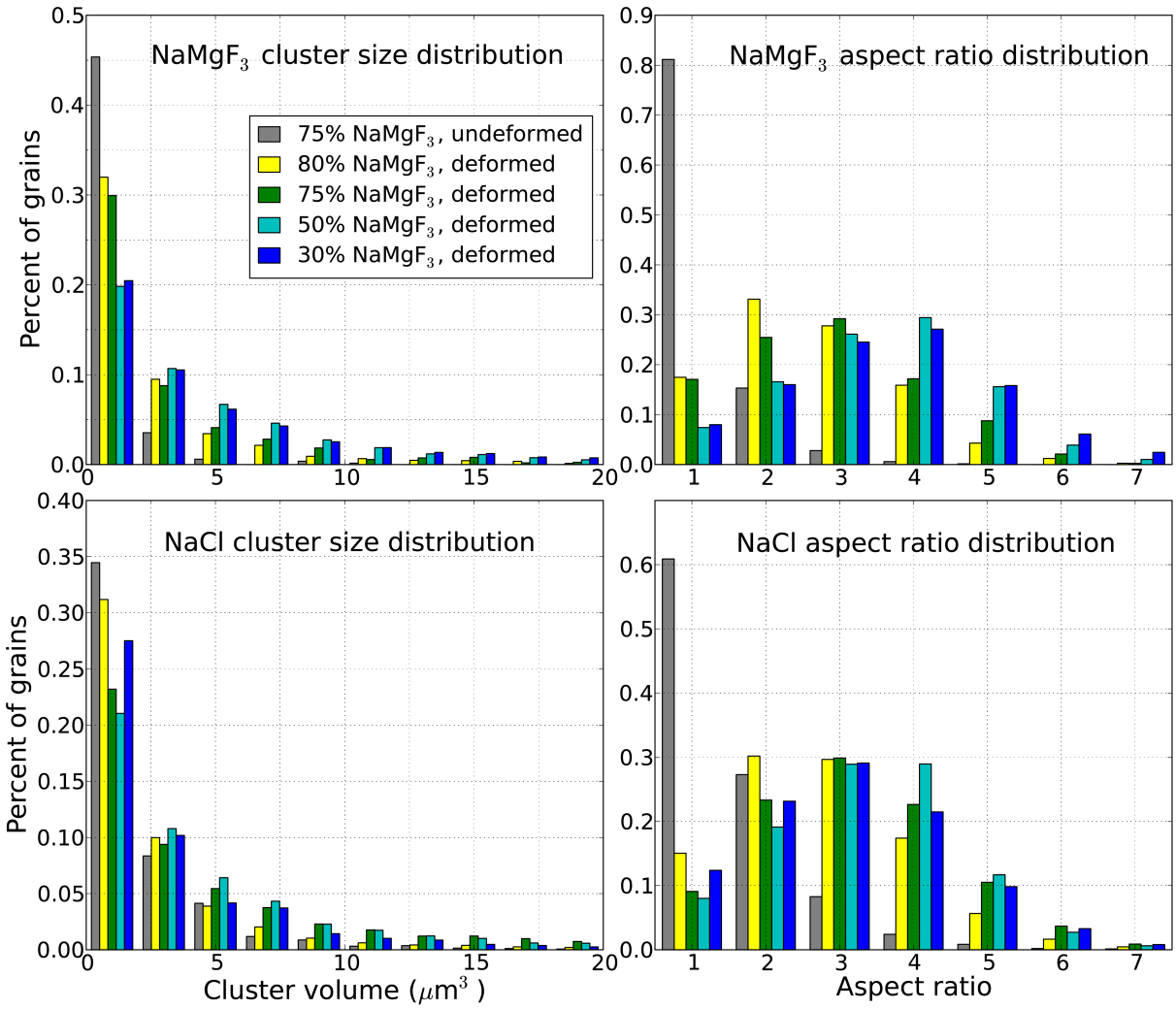

Figure 13. Histograms showing the distribution of grain cluster sizes and grain cluster aspect ratios in $NaMgF_3$ and NaCl for three deformed samples and one undeformed sample. Composition colors correspond to previous plots.

The aspect ratios of grain clusters of each phase are graphed in Fig. 13. The largest distribution in the undeformed sample has aspect ratio =1, while the deformed samples have aspect ratio >1. This is true for both $NaMgF_3$ and NaCl. The $NaMgF_3$ grain clusters in samples with the lowest $NaMgF_3$ volume fraction (30% and 50% $NaMgF_3$) and the least $NaMgF_3$ connectivity (Table 3), have the largest aspect ratios (~ 3), and samples with greater connectivity (75% and 80% $NaMgF_3$) have a smaller aspect ratio (~2). The largest bin of aspect ratios of NaCl for all deformed samples is 3, except for the 20% NaCl sample that has a different microstructure from the other samples.

4.4.4 Scanning Electron Microscopy

Since X-ray diffraction patterns collected for samples under large strain are unreliable for determining grain size, and microtomography could not resolve grain size, a backscattered image of an undeformed 75% $NaMgF_3$ sample was collected in a Zeiss Evo Ma10 scanning electron microscope (SEM) at 1000× magnification. Resolution in the scanning electron microscope is higher than for the X-ray microtomography, and qualitatively it is seen in Fig. 14 that NaCl grains (white) are smaller than $NaMgF_3$ grains.

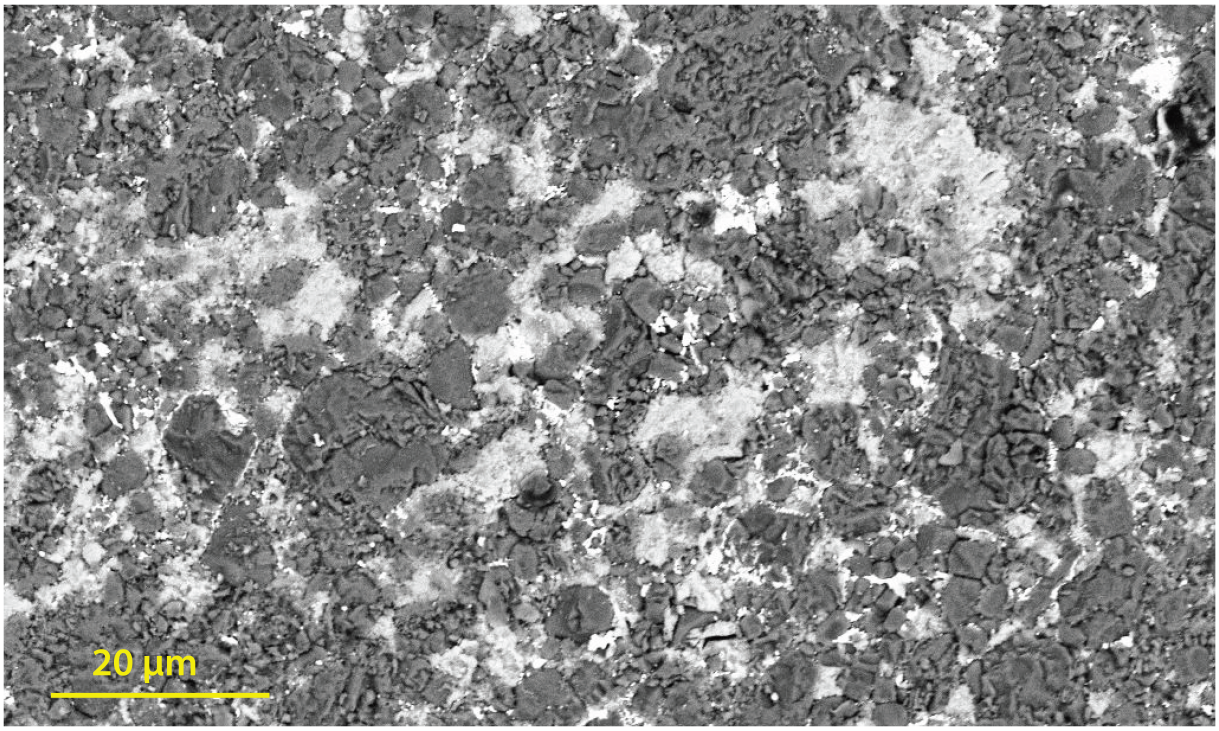

Figure 14. Image of an undeformed sample with 75% $NaMgF_3$ (darker gray) and 25% NaCl (white) collected in a scanning electron microscope at 1000× magnification.

4.5 Discussion

4.5.1 Experimental deformation results

Texture strength in $NaMgF_3$ was greatly reduced by addition of just 15% of softer NaCl, and further decreased with increased NaCl composition. Differential stress in $NaMgF_3$ also decreased with addition of NaCl. This suggests that NaCl accommodates much of the deformation. Meanwhile NaCl develops very low maximum pole densities (< 1.5 m.r.d.) and low differential stress (< 0.5 GPa), which are both an order of magnitude less than for $NaMgF_3$, demonstrating that stress partitions into the harder $NaMgF_3$ phase.

Several studies find that 10%-20% volume of the soft phase is enough for it to be interconnected and coat the grains of the harder phase (e.g. Cahn 1966; limestone-halite, Jordan 1987; quartz-muscovite, Tullis and Wenk 1994; camphor and octachloropropane, Bons and Cox 1994 and Bons and Urai 1994; quartz-plagioclase-biotite gneiss, Holyoke and Tullis 2006; forsterite-enstatite, Li et al. 2007), but others find that 25% volume percent or more of the soft phase is needed (e.g. finite element modeling of Mg-perovskite and MgO, Madi et al. 2005; Mg-perovskite and (Mg,Fe)O, Yoshino et al. 2008). For the system $NaMgF_3$ + NaCl it seems that 15% of softer NaCl is at the threshold for being interconnected as explained next, as explained below.

Deformation of NaCl has been studied extensively and has been shown to develop a texture consistent with a pole density maximum at {001} or {101} in IPFs when deformed in compression (Franssen 1994), and at {111} when deformed in extension (Skrotzki and Welch 1983, Lebensohn et al. 2003). The pole density maxima seen at {112} and {101} in IPFs in Fig. 4 and in the Appendix may have developed as a result of NaCl grains lying in very narrow veins between harder $NaMgF_3$ grains and being deformed heterogeneously depending on the grain shape and orientation of neighboring $NaMgF_3$ grains. A similar texture was observed for MgO in a Mg-perovskite + MgO assemblage deformed in the DAC (Miyagi 2009). The anomalous NaCl texture is also seen for the 20% NaCl sample (see Appendix), suggesting that the NaCl network is still relatively thin. In contrast, compositions with 25% NaCl or more develop a texture similar to previous single phase compression experiments of NaCl (Skrotzki and Welch 1983, Franssen 1994). Based on these results it appears as though, while 15% of NaCl greatly reduces preferred orientation in the aggregate, NaCl may not be fully connected until present in 25%. Microtomography suggesting that NaCl is not completely connected at lower volume percent supports this.

Relatedly, in samples with <25% volume fraction of NaCl, $NaMgF_3$ acquires an extension of the {100} maximum in IPFs extending up towards {010} (Fig. 4 and Appendix). The {100} extension is very pronounced in the 100% $NaMgF_3$ samples and diminishes with NaCl. Likely, because less deformation is accommodated by the network of NaCl grains at low NaCl volume percent, additional slip systems in $NaMgF_3$ are activated leading to the secondary maximum observed in $NaMgF_3$.

Samples containing 50% volume of each phase have the least amount of preferred orientation and lowest differential stress. Further increasing NaCl volume to 70% does not change texture strength or differential stress in $NaMgF_3$ (Fig. 5 and Fig. 6), but leads to stronger texture and greater differential stress in NaCl (Fig. 7 and Fig. 8). The stronger texture in NaCl in the 70% NaCl sample likely corresponds to decreased connectivity of $NaMgF_3$ (Table 3).These observations demonstrate that the aggregate is weakest for intermediate compositions and cannot accommodate as much stress as either single phase $NaMgF_3$ or NaCl. This has been observed for other two-phase systems (e.g. McDonnell et al. 2000, Ji et al. 2001, Covey-Crump et al. 2006, Li et al. 2007, 2013).

Differential stress (Fig. 6 and Fig. 8) and CPO (Fig. 5 and Fig. 7) decreased in both $NaMgF_3$ and NaCl once roughly 20% strain was reached, likely due to strain weakening. However a decrease in differential stress nor CPO occurred in the colder 100% $NaMgF_3$ sample. The gradual decline of strength and preferred orientation beyond 20% strain in the two-phase samples may be due to a transition of deformation mechanism from dislocation slip to grain boundary sliding or migration by recrystallization as suggested by others (mica-quartz, Tullis and Wenk 1994; orthopyroxene-olivine, Farla et al. 2013) who also observed strain weakening in two-phase systems. Grain boundary pinning by a second phase is more likely to lead to recrystallization and grain boundary migration (e.g. Wenk and Pannetier 1990, Herwegh and Berger 2004, Linckens et al. 2011, Herwegh et al. 2011), explaining why strain weakening was observed for the two phase samples but not in the 100% $NaMgF_3$ sample. Both lower connectivity of NaCl in the 75% $NaMgF_3$ sample after deformation (Table 3) and the smaller grain size of NaCl (Fig. 15) suggest that flow of NaCl grains took place.

Temperature effects, though small, also decreased differential stress, and to a smaller degree, texture, in both $NaMgF_3$ and NaCl for all samples. At lower temperatures, dynamic recrystallization and diffusion cannot keep up with deformation, leading to strain hardening. At high temperature, dislocations can climb and glide more easily, but even at high temperature this cannot happen so easily if a second phase is present in large enough volume to pin grain boundaries. In this situation, deformation may be accommodated by grain boundary sliding or grain boundary sliding with some dislocation creep (Herwegh and Berger 2004, Mehl and Hirth 2008) or by recrystallization (e.g. Farla et al. 2013).

If grain boundary migration does occur during deformation, the microstructure of the sample will evolve. In fact, statistics from microtomography show a tendency of grains to form larger clusters during deformation (Table 3, compare undeformed grain cluster sizes in first row to those in the third row). Likewise, Li et al. (2007) observed clustering of upper mantle minerals MgO and spinel in MgO + spinel aggregates. They found that the MgO clusters surround the spinel in the 75% spinel sample, much like liquid filling voids, similar to NaCl in the 75% $NaMgF_3$ in Fig. 11b, further supporting the idea that softer phase carries the strain.

Anomalous results for the sample with 80% $NaMgF_3$ (20% NaCl) demonstrate that microstructure greatly influences deformation. The NaCl in this sample is 98.4% connected while the sample with 25% NaCl is only 95% connected, yet the latter develops a stronger preferred orientation. Comparison of a tomography slice of this sample with tomography slices for the other samples (Fig. 11) show a much different microstructure with NaCl being more strongly clumped and less intermixed with $NaMgF_3$ grains. Rather than forming a fine interconnected web of NaCl grains that coat most of the harder $NaMgF_3$ grains like the other samples, the NaCl in the 20% NaCl sample clumps into large branches that do not touch many of the $NaMgF_3$ grains.

Evolution of crystallographic preferred orientation, the location of maximum pole densities in IPFs and corresponding slip activity, and the effect of microstructure on preferred orientation and strain heterogeneity can be examined more carefully with polycrystal plasticity models.

4.5.2 Polycrystal plasticity simulations

4.5.2.1 Self-consistent model

Viscoplastic self-consistent (VPSC) modeling (Molinari et al. 1987, Lebensohn and Tomé 1993, Lebensohn et al. 2007), as described in the previous chapters, was done to infer slip system activities during two-phase deformation experiments. VPSC allows grain inclusions of multiple phases to be deformed in a homogenous medium that has the average properties of the composite. Simulations with 2000 grains of each $NaMgF_3$ (larger grains) and NaCl (smaller grains) present in various volume fractions were compressed to 30% equivalent strain in 1% increments. The texture before deformation was random for both $NaMgF_3$ and NaCl in experiments, thus grains were initially randomly oriented in VPSC. A stress exponent of $n = 3$ was assumed (Wu 2002). A closest match to experimental texture for $NaMgF_3$ and NaCl (Fig. 4) was created using the relative CRSS

with corresponding activities for five compositions shown in Table 4 and Table 5, respectively.

Table 4. Relative CRSS assigned to slip systems for $NaMgF_3$ and resulting slip activity (%) for five different compositions. The twinned model was run for 100% $NaMgF_3$.

Slip/twin systems	(100) <010>	(100) <011>	(010) [100]	(010) <101>	(001) <100>	(001) <010>	(001) <110>	{111} $<01\bar{1}>$	*{110} $<1\bar{1}0>$
CRSS	3	4	3	4	3	3	4	10	10
twinned	0.099	0.111	0.099	0.102	0.135	0.122	0.118	0.213	0.001
CRSS	0.5	0.5	10	10	5	5	5	--	--
100%	0.102	0.793	0.000	0.004	0.001	0.044	0.054	0.000	0.000
85%	0.088	0.616	0.000	0.002	0.001	0.025	0.031	0.000	0.000
75%	0.078	0.514	0.000	0.002	0.001	0.017	0.021	0.000	0.000
50%	0.051	0.303	0.000	0.001	0.001	0.006	0.007	0.000	0.000
25%	0.025	0.136	0.000	0.000	0.000	0.002	0.002	0.000	0.000

*twin system

Table 5. Relative CRSS assigned to slip systems for NaCl and resulting slip activity (%) for five different compositions.

Slip systems	{111} $[10\bar{1}]$	{110} $[\bar{1}10]$	{100} [011]
CRSS	2.50	0.25	3.00
15%	0.038	0.143	0.055
25%	0.056	0.233	0.079
50%	0.078	0.441	0.111
75%	0.082	0.639	0.114

Slip on (100)<010> and (100)<011>, with some contribution from twinning of $\{110\}<1\bar{1}0>$, is likely responsible for the maximum pole density seen at (100) in experimental $NaMgF_3$ IPFs (Fig. 4). Twinning activity decreases once grains have twinned: initial activity for twinning $\{110\}<1\bar{1}0>$ was 1.2%, but by 30% strain, twinning decreased to 0.1% activity (Table 4), indicating it is nearly complete. Twinning alone produced a maximum pole density at (100) in the IPF (Fig. 15) that is much weaker than the maximum pole density observed in experiments, suggesting that slip on (100)<010> and (100)<011> is mostly responsible for the (100) texture. Texture similar to that of $NaMgF_3$, with (100) planes oriented perpendicular to compression, was observed for Mg-

perovskite by Wenk et al. (2004) and Miyagi (2009) immediately following the transition from lower pressure $MgSiO_3$ polymorphs. They attributed this texture to twinning of $\{110\}<1\bar{1}0>$ or nucleation in a stress field. However, a pole density maximum at (001) in IPFs developed during subsequent compression in the DAC in some samples suggesting that slip on (001) is most active during deformation in Mg-pervoskite.

VPSC results show a closest match to experimental results for NaCl textures with slip on $\{110\}<1\bar{1}0>$, in agreement with previous studies of slip in NaCl (Carter and Heard 1970, Skrotzki and Haasen 1981) and (Mg,Fe)O (e.g. Wenk et al. 1989b, Merkel et al. 2002, Lin et al. 2009, Kaercher et al. 2012).

Pole density maximums predicted by VPSC for both $NaMgF_3$ and NaCl decreased with the addition of NaCl, but not nearly as much as observed in experiments; the decrease in pole densities due to adding 15% NaCl was only 0.91 m.r.d. in simulations, in contrast to, on average, 2.00 m.r.d. observed in experiments. As expected, Table 4 shows that activities of $NaMgF_3$ slip systems greatly decrease, while activities of NaCl slip systems increase with increasing NaCl content.

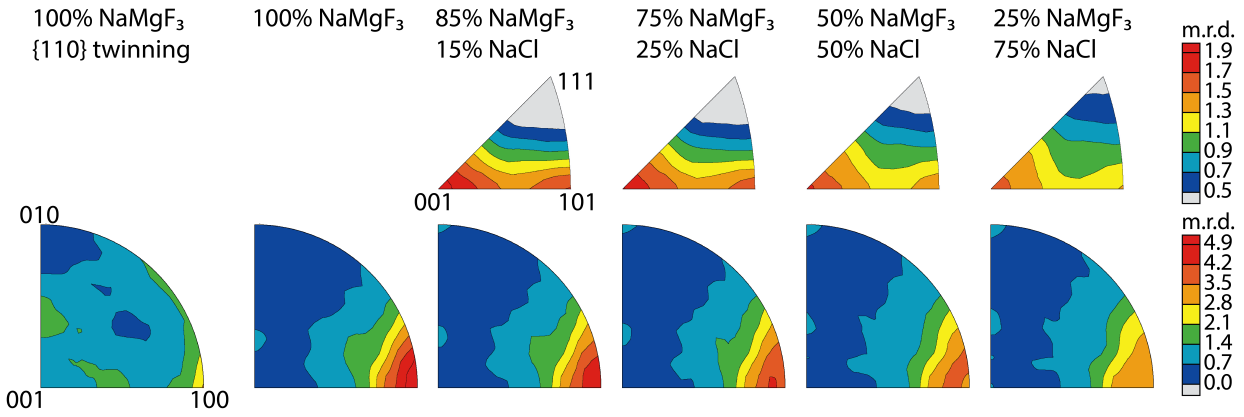

Figure 15. Inverse pole figures showing VPSC results for crystallographic preferred orientation relative to compression in $NaMgF_3$ and NaCl for varying volume fractions. Pole densities are shown in m.r.d. with separate scales for each phase. Equal area projections.

Although the location of maximum pole densities obtained with VPSC for $NaMgF_3$ and NaCl are well matched to experiments, the texture strengths are not, likely because the amount of CPO also depends on interaction between grains of different phases with different elastic and plastic properties, shapes, and crystallographic orientations. VPSC

simulations, which only consider the interaction among individual grains and the homogenous equivalent medium, underestimate stress and strain heterogeneity and are not ideal for modeling two-phase deformation.

4.5.2.2 Viscoplastic model using fast Fourier transform

Two-phase viscoplastic deformation was also modeled with a method that uses fast Fourier transform (FFT) and Greens functions. This method solves the governing equations for stress and strain rate at regularly-spaced grid points in a chosen 3D microstructure in response to an applied strain; it is well-suited for simulating deformation in heterogeneously materials such as two-phase composites. The code used here was developed by Ricardo Lebensohn and is based on the model of Moulinec and Suquet (1994, 1995, 1998) for elastic and elastoplastic deformation, later adapted for viscoplastic deformation by Michel et al. (2000, 2001). As opposed to methods which employ the finite element method (FEM) (e.g. Mika and Dawson 1998, Barbe et al. 2001a, b, Delanney et al. 2006), the FFT method avoids meshing, which, depending on mesh resolution, can complicate results for local stress variations (Barbe et al. 2001) and convergence (Diard et al. 2005). In addition, FEM has a greater number of degrees of freedom and limits the volume that can be modeled in a reasonable amount of time. FEM has computing times that scale as N^2, where N is the number of discretization points, while FFT has computing times that scale as $N \times \log(N)$ and converge much more rapidly to a solution for a larger volume (e.g. Lebensohn et al. 2008). However, the FFT method, which uses Green functions, requires a repeating microstructure, making its application less general than that of FEM. The method is briefly described below with more details and equations found in Lebensohn (2001) and Lebensohn et al. (2008), but first the derivation of the repeating microstructures used here is explained.

Voronoi tessellations (Voronoi 1908) were created to have a likeness to the microstructures of the $NaMgF_3$ and NaCl samples observed with microtomography and SEM (Fig. 11, Fig. 12, Fig. 14). Voronoi cells (grains in this case) are produced from a set of points (or seeds) spaced in three dimensions. All points in space closest to a given seed are assigned to that seed and make up one grain, or equivalently, grain boundaries are drawn equidistant between neighboring seeds. The volume containing these seeds can be repeated to give a periodic grain map. Volume fractions and grain size distributions obtained from microtomography analysis for each of $NaMgF_3$ and NaCl were used to determine how many Voronoi seeds to use for each phase. Since the SEM image (Fig. 14) showed NaCl grains to be much smaller than $NaMgF_3$ grains, NaCl seeds were spaced more closely together, while $NaMgF_3$ seeds were spaced further apart. Placement of Voronoi seeds not only determines grain size but also grain shape and phase distribution.

Two microstructures with 75% $NaMgF_3$ and 25% NaCl were created: a "random" microstructure, in which equant grains of both phases are randomly distributed, and a "percolate" microstructure, in which NaCl grains lie as veins between harder $NaMgF_3$ grains (Fig. 16). The "random" microstructure was constructed by creating two Voronoi tessellations, one with 300 $NaMgF_3$ seeds spaced further apart, and one with 1337 NaCl seeds spaced more closely together. The two 3D Voronoi grain maps created from these tessellations were then merged to create a 3D volume with 300 $NaMgF_3$ grains having average grain size five times larger than the 1337 NaCl grains. The "percolate" microstructure was similarly created using 55 $NaMgF_3$ grains and 79 NaCl grains. A third "random" microstructure with 100% $NaMgF_3$ was created to see what effect a second phase has on deformation. Finally, each grain, already labeled as $NaMgF_3$ and NaCl, was indexed and assigned an orientation. Because no CPO before deformation was observed with X-ray diffraction, the initial orientation of grains was random.

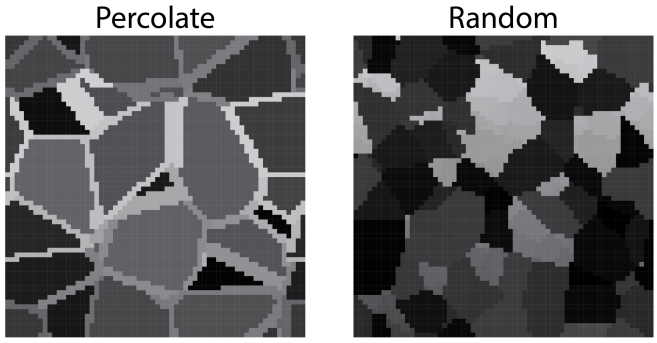

Figure 16. Two microstructure types used in FFT simulations. $NaMgF_3$ grains are darker gray, and NaCl grains are lighter grey.

These 3D microstructures/grain maps were then discretized into a grid of Fourier points. Here a grid of 64 × 64 × 64 points was chosen to obtain higher resolution in a reasonable amount of time (15 hours or less if running on an 8 GB RAM laptop). Each Fourier point falling inside of a given grain in the microstructure acquired that grain's index number, phase label, and grain orientation. These Fourier points are Lagrangian, as opposed to Eulerian, such that during axial shortening, Fourier points maintain their grain index number and phase label but may acquire different spatial coordinates. Thus grains are shortened along with the sample but maintain constant volume (e.g. they cannot break or recrystallize) during pure shear deformation.

The FFT-based model is a full-field solution that iteratively adjusts both the strain and stress field to minimize work while fulfilling stress equilibrium and strain compatibility at each Fourier point. The local constitutive equation relating deviatoric stress field $\sigma'(\mathbf{x})$

(introduced in Chapter 2) and strain rate $\dot{\varepsilon}_{ij}(\mathbf{x})$ evaluated at grid point $\mathbf{x}$ for crystal plasticity is

$$\dot{\varepsilon}_{ij}(\mathbf{x}) = \sum_{k=1}^{N_S} m^s(\mathbf{x})\dot{\gamma}^s(\mathbf{x}) = \dot{\gamma}_o \sum_{k=1}^{N_S} m^s(\mathbf{x}) \left(\frac{\left| m^s(\mathbf{x}) : \sigma'(\mathbf{x}) \right|}{\tau_o^s(\mathbf{x})} \right)^n \times \mathrm{sgn}(m^s(\mathbf{x}) : \sigma'(\mathbf{x})), \quad (1)$$

where N_s is the number of slip and twinning systems, $m^s(\mathbf{x})$ and τ_o^s are the symmetric Schmid tensor and CRSS associated with a slip system (s), $\dot{\gamma}^s(\mathbf{x})$ is the shear rate and $\dot{\gamma}_o$ is a normalized factor of the local shear rate, and n is the rate-sensitive exponent (e.g. Rollett et al. 2010, Lebensohn et al. 2008), similar to the stress exponent introduced in Chapter 1. The ":" symbol denotes a double-dot product.

The local strain field $\dot{\varepsilon}_{ij}$ can also be written as a function of the local velocity field $v_k(\mathbf{x})$. Meanwhile, the stress field $\sigma'(\mathbf{x})$ is written as a sum of the stiffness of a linear reference field L^0, which must be chosen, and a displacement field (i.e. polarization field) $\varphi_{ij}(\mathbf{x})$ minus the hydrostatic pressure field $p(\mathbf{x})$. Differential equations that satisfy strain compatibility, stress equilibrium, and periodic boundary conditions across the unit cell boundary can be used to obtain the local strain field $\dot{\varepsilon}_{ij}(v_k(\mathbf{x}))$ if $\varphi_{ij}(\mathbf{x})$ is known. The displacement field $\varphi_{ij}(\mathbf{x})$ is solved for by convolution with Green functions that are associated with $v_k(\mathbf{x})$ and $p(\mathbf{x})$; these Green functions are obtained by taking the Fourier transform of the equations describing strain compatibility and stress equilibrium. In Fourier space, these convolution integrals are simply products, thus these calculations are done in Fourier space $\{\boldsymbol{\xi}^{\mathbf{d}}\}$ rather than in Cartesian space $\{\mathbf{x}^{\mathbf{d}}\}$. Once $\varphi_{ij}(\boldsymbol{\xi})$ is solved for in Fourier space, it is converted back into real space using inverse Fourier transform. However, this only provides a new guess of $\varphi_{ij}(\mathbf{x})$ until convergence is reached.

The "augmented Lagrangians" scheme, first introduced by Michel et al. (2000, 2001), is used to guarantee convergence. This scheme uses two strain fields and two stress fields, with one strain field fulfilling compatibility, and one stress field fulfilling equilibrium. Constitutive equations are used to iteratively relate the two strain fields and two stress fields until they converge.

Once convergence is reached, the deviatoric stress field $\sigma'(\mathbf{x})$, and thus the local strain rate field $\dot{\varepsilon}_{ij}(\mathbf{x})$, can be determined from $\varphi_{ij}(\mathbf{x})$ for all discritization points and mapped as long as $m^s(\mathbf{x})$ and τ_o^s are known. In addition, the rotation rate of the crystallographic lattice $\dot{\omega}_{ij}^p(\mathbf{x})$, defined as

$$\dot{\omega}_{ij}^{p}(\mathbf{x}) = \sum_{s=1}^{N_s} \alpha_{ij}^{s}(\mathbf{x}) \dot{\gamma}^{s}(\mathbf{x}), \qquad (2)$$

where $\alpha_{ij}^{s}(\mathbf{x})$ is the antisymmetric Schmid tensor, can be solved once the strain field, and thus $\dot{\gamma}^{s}(\mathbf{x})$, is known. Therefore resulting CPO is predicted.

In simulations done here, stress was defined as axial compressive, and the same relative CRSS used in VPSC simulations for $NaMgF_3$ (Table 4) and NaCl (Table 5) were defined in input files. The volume was then shortened to either 20% or 30% strain in incremental 2% strain steps. Grains are shortened along with the sample, resulting in greater aspect ratios after deformation, just as was observed with microtomography. Grain orientation relative to compression, grain shape, and the shape, orientation, and phase of neighboring grains, all of which cause stress and strain to distribute heterogeneously, are considered.

Two-dimensional grain maps and maps of average strain rate for all slip systems are shown in Fig. 18. Resulting inverse pole figures for $NaMgF_3$ and NaCl in the random structures show a closer match to experimental textures (Fig. 4) than VPSC (Fig. 15) for samples with 75% $NaMgF_3$ or less. However, FFT underestimates the texture strength in the 100% $NaMgF_3$ sample. By changing the microstructure such that NaCl lies as veins in between $NaMgF_3$ grains, a closer match to samples with higher $NaMgF_3$ volume percent is produced, suggesting samples with less than 25% NaCl may have a similar microstructure.

As seen in the strain rate maps, strain is concentrated in the NaCl, especially for the "percolate" structure. In the 100% $NaMgF_3$ sample, strain is more homogenous. These results agree with flow laws outlined by Handy (1994) and with other two-phase deformation experiments (e.g. Tullis 2002, Holyoke and Tullis 2006) for which strain rate, and sometimes stress are higher in the interconnected softer phase, but nearly uniform for samples in which the soft phase is not interconnected.

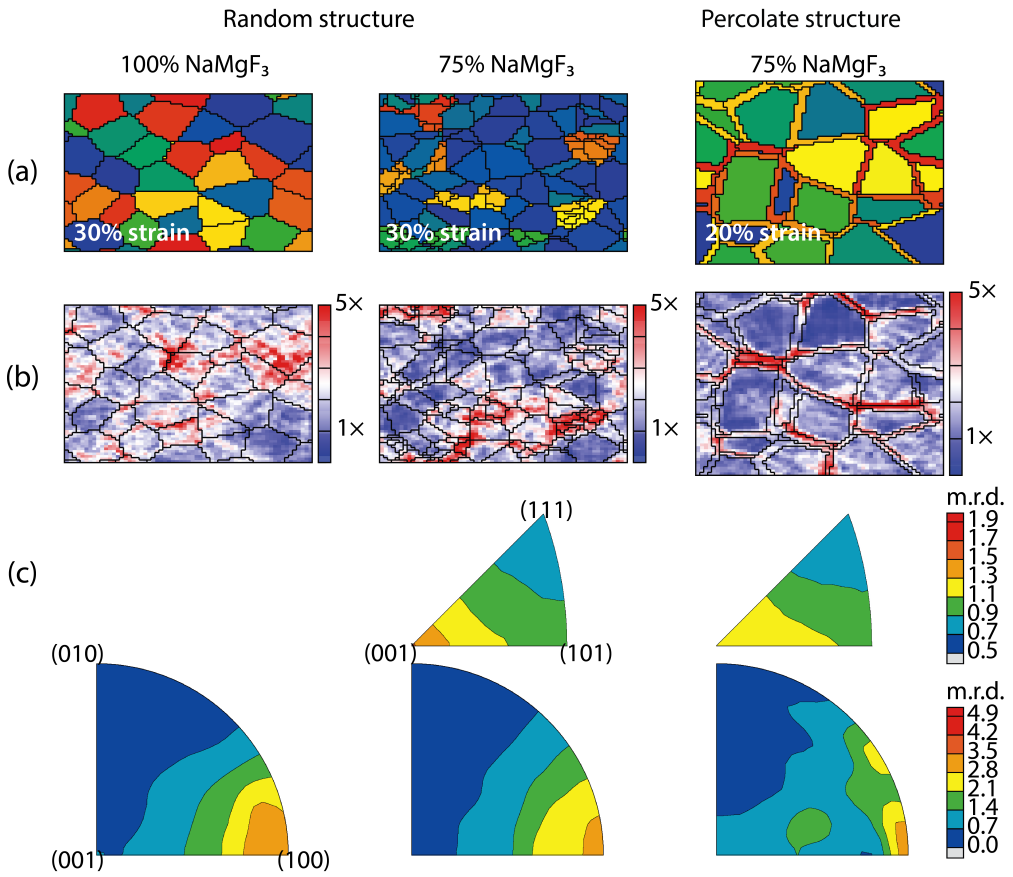

Figure 17. Microstructures (a), maps of average strain rate (b), and associated inverse pole figures for NaCl and $NaMgF_3$ (c) are shown for the "random" structure with two different compositions (100% $NaMgF_3$ and 75%$NaMgF_3$ + 25% NaCl) and for the "percolate" structure with composition 75% $NaMgF_3$ + 25% NaCl. $NaMgF_3$ grains in the grain maps (a) are shades of blue in the 75% $NaMgF_3$ random structure, and shades of bright yellow, green, and blue in the percolate structure. Color bars in strain rate maps (b) show relative strain rate with red being fastest, and blue being slowest. Pole densities in inverse pole figures (c) are given in multiples of distribution (m.r.d.). Inverse pole figures are equal area projections.

4.6 Implications for rheology of the lower mantle

There are clearly differences between the deformation of analog minerals $NaMgF_3$ and NaCl at experimental conditions and deformation of Mg-perovskite and MgO at lower mantle conditions. Different strain rates may cause deformation to occur in different regimes and affect the strength of materials (e.g. Hirth and Tullis). For example, slip is less active at lower strain rate in NaCl (Carter and Heard 1970) and MgO (Routbort

1979), which suggests that CPO may be less in the lower mantle (strain rates of ~10^{-14} s^{-1}) than in D-DIA experiments (~10^{-5} s^{-1}). Grain sizes in experiments are on the order of microns, whereas grains in the mantle are presumably much larger, making grain-size dependent mechanisms, such as grain boundary sliding, less likely to occur, and grain-size independent mechanisms, such as dislocation creep and climb, more likely to dominate (Frost and Ashby 1982, Wenk and Pannetier 1990). While twinning has been observed in $NaMgF_3$ and Mg-perovskite in experiments, twinning probably does not occur in the deep Earth due to low stresses, higher temperatures, and much lower strain rates.

Despite these differences, there is overwhelming support that texture is greatly reduced by the presence of a second phase for a two-phase system similar to $MgSiO_3$ and MgO. For the lower mantle mineral analogs, soft NaCl uptakes most of the deformation via a mechanism that does not produce strong CPO and reduces the activity of slip in both NaCl and harder $NaMgF_3$. Studies of other two phase assemblages also observed a switch in dominant deformation mechanism with the addition of a second phase (e.g. spinel-periclase, Li et al. 2007; olivine-orthopyroxene, Skemer and Karato 2008). This mechanism becomes more pronounced beyond 20% strain, suggesting that the microstructure reorganizes during deformation. This may have occurred by grain boundary migration or recrystallization, which create smaller grain sizes and promote grain-size dependent mechanisms such as diffusion creep (Warren and Hirth 2006, Herwegh et al. 2011, Tasaka and Hiraga 2013). As shown with viscoplastic polycrystal models using FFT, reorganization of the microstructure and/or evolution of the microstructure with increasing stress towards a structure with interconnected soft phase increases strain localization and weakening and decreases CPO. In fact, calculations of viscosities in the lower mantle that take both Mg-perovskite and MgO into account find that lower mantle rheology highly depends on microstructure and strain (Yamazaki and Karato 2001), and likely diffusion creep dominates in the lower mantle. The switch from slip-accommodated deformation to another mechanism that does not produce CPO may help explain why the lower mantle is mostly isotropic (e.g. Karato et al. 1995, Meade et al. 1995). Including the effect of interactions between two phases on rheology in geophysical models of the lower mantle would improve them (e.g. Cottaar et al. 2014, *in press*).

It is clear that addition of second softer phase leads to strain weakening and reduction of CPO through promotion of other deformation mechanisms over slip. The next step is to identify which mechanisms these are, which may be done by examining deformed samples more closely using electron microscopy or perhaps with *in situ* microtomography, to better constrain rheology in the lower mantle.

Chapter 5

Conclusions

Crystallographic preferred orientation (CPO) provides insight into phase relationships and deformation mechanisms at the angstrom scale. On a larger scale, these mechanisms can be linked to deformation history and help connect seismic observations to composition and evolution in the Earth. Chapter 2 and 3 focused on microscale properties, namely the evolution of crystallographic structure and related preferred orientation during the cubic-to-rhombohedral phase transition in wüstite (FeO) (Chapter 2), and the slip activity responsible for observed preferred orientation in stishovite at high pressure (Chapter 3). These experiments were done in diamond anvil cells (DACs) while collecting diffraction patterns with synchrotron X-rays in radial geometry (X-ray beam perpendicular to compression) in order to observe all crystallographic orientations relative to compression. Chapter 4 explores how deformation occurs in a two-phase system that is relevant to the lower mantle, which consists of mostly $MgSiO_3$ perovskite and MgO. Instead of a DAC, a multianvil press was used (D-DIA), limiting pressures to 12 GPa or less, thus analog minerals $NaMgF_3$ perovskite (isostructural to $MgSiO_3$ perovskite), and NaCl (isostructural to MgO) that are stable at lower pressures were used. Results are summarized below, and future studies are suggested.

The phase transition in wüstite from cubic to rhombohedral symmetry displayed orientation variant selection. Cubic crystals preferentially aligned with {001} planes perpendicular to the compression direction. During the phase transition, one body diagonal extends, causing the $\{101\}_c$ cubic planes to separate into two symmetrically unequivalent sets of planes, $\{10\bar{1}4\}_r$ and $\{11\bar{2}0\}_r$. Whereas both of these sets of planes were oriented at the same angle relative to compression in the cubic phase, upon nucleation in the rhombohedral phase, $\{10\bar{1}4\}_r$ orients perpendicular to compression, and $\{11\bar{2}0\}_r$ orients parallel to it. Correspondingly, one daughter of $\{111\}_c$, $\{10\bar{1}1\}_r$, preferentially aligns more closely perpendicular to compression than its sibling, $(0001)_r$. Since the texture is already present immediately after the transition and before deformation, it is likely due to a martensitic mechanism. The variant selection is likely related to the structural relationships and corresponding elastic constants, which have not yet been determined for rhombohedral FeO. Thermodynamic theory suggests that $\{10\bar{1}4\}_r$ and $\{10\bar{1}1\}_r$, which align more closely perpendicular to compression, are elastically softer than their siblings, however this

should be confirmed. For a future study, elasticity in rhombohedral FeO may be measured or calculated, for example, using density functional theory.

This demonstrates that CPO observed in the Earth with seismic tomography may not only be due to slip, but also due to phase transitions and dynamic recrystallization. Thus CPO may evolve with depth in the Earth even in the absence of slip due to phase transitions. Another example of CPO development is during the transition from quartz to stishovite.

In Chapter 3, little to no preferred orientation was observed in quartz, even at stresses as high as 6.5 GPa – just a weak texture likely due to mechanical twinning. However, during the transition at high pressure from quartz, stishovite crystals nucleated with their (001) planes preferentially orientated perpendicular to compression and acquired stronger (001) texture with increasing pressure due to subsequent slip. Polycrystal plasticity modeling of uniaxial compression in stishovite using a self-consistent method found that active pyramidal slip (on {101} planes) and basal slip (on (001) planes) can both explain the observed texture. This disagrees with transmission electron microscopy (TEM) studies of stishovite done by Cordier and Sharp (1998), Cordier et al. (2004), and Texier and Cordier (2006) that examined dislocations in stishovite and inferred prismatic slip (on (100) planes) to be the responsible mechanism. These experiments were done at pressures of 14 GPa and temperatures of 1300°C in contrast to mine, which were done at slightly higher pressure but room temperature. Different slip systems become more active at higher temperatures, which may explain the difference in observed slip system activities. It would be interesting to repeat this experiment, but at higher temperature. Conventionally, laser heating is used in DAC experiments and produces temperatures of up to >4000 K (e.g. Shen et al. 2001), but with less control, especially for lower temperatures, and greater temperature gradients (e.g. Manga and Jeanloz 1996). However, recent developments for resistive heating in the DAC (e.g. Liermann et al 2009, Du et al. 2013, Miyagi et al. 2013) may make such an experiment possible.

The slip activities that occur at a very small scale can have a great impact at a much grander scale. The alignment of crystallographic planes due to slip or recrystallization in a stress field for minerals in the Earth influences deformation and plastic flow. For example, in the mantle, CPO has been shown to lead to anisotropic viscosity (Vauchez et al. 1998, Hansen et al. 2012). Besides viscosity, deformation mechanisms such as slip influence the strength of the mantle (e.g. Skemer et al. 2010). Viscosity and strength of the mantle greatly impact surface processes such as plate motion, and related processes such as volcanism and mountain building.

Chapter 4 focused on deformation of the lower mantle with experiments in a multianvil press called the Deformation-DIA (D-DIA). Based on seismic observations, mineral physics, and meteorite and solar nebular observations, the lower mantle is

estimated to be composed of 20-25% (Mg,Fe)O and ~75% $MgSiO_3$ perovskite. However, while many studies have examined deformation in each of these minerals separately (e.g. Routbort 1979, Merkel et al. 2002, 2003, Chen et al. 2002, Wenk et al. 2004, Li et al. 2005, Miyajima et al. 2009, Carrez et al. 2009, Kaercher et al. 2012), very few have examined the deformation in the two-phase system. Since the D-DIA can only reach pressures up to 12 GPa, lower pressure analogs $NaMgF_3$ perovskite (neighborite) and NaCl (halite) were used in place of mantle minerals $MgSiO_3$ perovskite and MgO.

Deformation experiments of lower mantle mineral analogs $NaMgF_3$ and NaCl show that CPO in the harder phase, $NaMgF_3$, greatly decreases with the addition of as little as 15% of the softer phase, NaCl, and continues to decrease as more NaCl is added. This suggests that the soft NaCl may already be largely interconnected at 15% volume fraction, forming a soft network around harder $NaMgF_3$ grains and thereby absorbing most of the deformation. However, 15% volume of NaCl may be at the threshold of what is needed to form an interconnected network. CPO of NaCl was very weak and irregular for samples containing less than 15-20% volume fraction of NaCl, as if hard $NaMgF_3$ grains impose strain heterogeneities, suggesting a very thin network of NaCl between hard $NaMgF_3$ grains.

The amount of differential stress that was supported and the development of CPO in both $NaMgF_3$ and NaCl gradually declined once ~15-20% strain was reached. Conversely, differential stress and CPO continued to increase beyond ~15-20% strain in the 100% $NaMgF_3$ samples. This demonstrates that strain weakening occurred here only in two-phase samples. This may be explained by reorganization of the microstructure during compression from one in which NaCl is not largely connected, and the stiffer $NaMgF_3$ supports the load, to one in which NaCl begins to flow between harder $NaMgF_3$ grains, or recrystallize along $NaMgF_3$ grain boundaries, to form an interconnected network.

Indeed, microtomography analysis of undeformed and deformed 3D microstructures showed a slight tendency of both $NaMgF_3$ and NaCl grains to cluster, and NaCl grains to flow in between harder $NaMgF_3$ grains, during deformation. This analysis also shows that both $NaMgF_3$ and NaCl are largely interconnected. Scanning electron microscope images depicting NaCl grains to be much smaller than $NaMgF_3$ suggest that NaCl may have more likely accommodated stress via a diffusion creep mechanism such as grain boundary diffusion or sliding rather than by slip.

I also examined the effect of microstructure on texture and strain heterogeneity, using a polycrystalline plasticity model that employs fast Fourier transform (FFT) and Green functions (e.g. Lebensohn et al. 2012). The results show strain rate to be most homogenous in the microstructure containing only $NaMgF_3$ grains. A "percolate" microstructure with NaCl lying in veins between the harder $NaMgF_3$ grains returned a

closer match to experimental $NaMgF_3$ texture for samples with < 25% NaCl suggesting that NaCl does form a network in between $NaMgF_3$ grains, even when present in only 15% volume.

These results have important implications for the lower mantle and may help explain why the lower mantle is observed to be mostly isotropic for seismic waves. The decrease in CPO and stress with addition of NaCl, especially for higher strain, suggests that (Mg,Fe)O in the lower mantle may control the rheology of the lower mantle, and that slip is not the major mechanism operating in most of the mantle.

Of course, experimental conditions differ from deep Earth conditions. In the lower mantle grain sizes are expected to be larger, stresses and strain rates lower than in experiments. These factors influence which deformation mechanism dominates, and therefore the development of CPO. Considering that strain rates equal to those in the Earth (on the order of 10^{-14} s^{-1}) are not feasible for experiments, and grain sizes and stresses are limited by experimental techniques and apparatuses, modeling may be a great alternative for studying two-phase deformation. Modeling of two phase deformation should be continued using fast Fourier transform, or perhaps the finite element method, to examine more carefully the effect of microstructure and strain rate.

References

Abrahams SC (1971) Ferroelasticity. Material Research Bulletin, 6: 881-890.

Amodeo J, Carrez P, Cordier P (2012) Modelling the effect of pressure on the critical shear stress of MgO single crystals. Philosophical Magazine, 92(12): 1523-1541.

Andrault D, Fiquet G, Guyot F, Hanfland M (1998) Pressure-induced Landau-type transition in stishovite. Science, 282: 720-724.

Angel RJ, Allan DR, Miletich R, Finger LW (1997) The use of quartz as an internal pressure standard in high-pressure crystallography. Journal of Applied Crystallography, 30: 461-466.

Antonangeli D, Siebert J, Aracne C, Farber D, Bosak A, Hoesch M, Krisch M, Ryerson F, Fiquet G, Badro J (2011) Spin crossover in ferropericlase at high pressure: a seismologically transparent transition? Science, 331: 64-67.

Asahara Y, Hirose K, Ohishi Y, Hirao N, Ozawa H, Murakami M (2013). Acoustic velocity measurements for stishovite across the post-stishovite phase transition under deviatoric stress: Implications for the seismic features of subducting slabs in the mid-mantle. American Mineralogist, 98: 2053-2062.

Ashbee KHG, Smallman RE (1963) The plastic deformation of titanium dioxide single crystals. Proceedings of the Royal Society A, 274: 195–205.

Auzende AL, Badro J, Ryerson FJ, Weber PK, Fallon SJ, Addad A, Siebert J, Fiquet G (2008) Element partitioning between magnesium silicate perovskite and ferropericlase: New insights into bulk lower-mantle geochemistry. Earth and Planetary Science Letters, 269: 164-174.

Badro J, Guillaume F, François G, Rueff JP, Struzhkin V, Vankó G, Monaco G (2003) Iron partitioning in earth's mantle: toward a deep lower mantle discontinuity. Science, 300: 789-791.

Badro J, Struzhkin V, Shu J, Hemley R, Mao HK (1999) Magnetism in FeO at megabar pressures from X-ray emission spectroscopy. Physical Review Letters, 83(20): 4101-4104.

Barbe F, Decker L, Jeulin D, Cailletaud G (2001a) Intergranular and intragranular behavior of polycrystalline aggregates. Part 1: F.E. model. International Journal of Plasticity, 17: 513-536.

Barbe F, Forest S, Cailletaud G (2001b) Intergranular and intragranular behavior of polycrystalline aggregates. Part 2: Results. International Journal of Plasticity, 17: 537-563.

Barber DJ (1990). Regimes of plastic deformation – processes and microstructures: an overview. Deformation Processes in Minerals, Ceramics and Rocks. The Mineralogical Society Series, ed. Barber DJ, Meredith PG, 1: 138-178.

Barnhoorn A, Bystricky M, Kunze K, Burlini L, Burg JP (2005) Strain localization in bimineralic rocks: Experimental deformation of synthetic calcite-anhydrite aggregates. Earth and Planetary Science Letters, 240: 748-763.

Bassett WA, Takahashi T, Mao HK, Weaver JS (1968) Pressure induced phase transformation in NaCl. Journal of Applied Physics, 39: 319-325.

Bate P, Hutchinson B (2000) The effect of elastic interactions between displacive transformation on textures in steels. Acta materialia, 48: 3183-3192.

Beauchesne S, Poirier JP (1989) Creep of barium titanate perovskite: a contribution to a systematic approach to the viscosity of the lower mantle. Physics of the Earth and Planetary Interiors, 55: 187-199.

Besson P, Poirier JP, Price GD (1996) Dislocations in $CaTiO_3$ perovskite deformed at high-temperature: a transmission electron microscopy study. Physics and Chemistry of Minerals, 23: 337-344.

Birch F (1952) Elasticity and constitution of the Earth's interior. Journal of Geophysical Research, 57: 227-286.

Birch F (1978) Finite strain isotherm and velocities for single-crystal and polycrystalline NaCl and high pressures and 300°K. Journal of Geophysical Research, 83(B3): 1257-1268.

Birch F (1986) Equation of state and thermodynamic parameters of NaCl to 300 kbar in the high-temperature domain. Journal of Geophysical Research, 91(B5): 4949-4954.

Bishop JFW, Hill R (1951) A theory of the plastic distortion of a polycrystalline aggregate under combined stresses. Philosophical Magazine, 42(327): 414-427.

Blanchin MG, Fontaine G (1975) Transmission electron microscope observations of deformed rutile (TiO_2). Physica Status Solidi (a), 29: 491-501.

Blanchin MG, Fontaine G, Kubin LP (1980) Dynamic strain aging in stoichiometric rutile single crystals. Philosophical Magazine A, 41: 261-280.

Boehler R (2000) Laser heating in the diamond cell: Techniques and applications. Hyperfine Interactions, 128(1-3): 307-321.

Bonczar L, Graham E (1982) The pressure and temperature dependence of the elastic constants of polycrystal magnesiowustite. Journal of Geophysical Research, 87(B2): 1061-1078.

Bons PD, Cox SJD (1994) Analogue experiments and numerical modeling on the relation between microgeometry and flow properties of polyphase materials. Material Science and Engineering A, 175: 237-245.

Bons PD, Urai J (1994) Experimental deformation of two-phase rock analogues. Materials Science and Engineering A, 175: 221-229.

Bovolo CI (2005) The physical and chemical composition of the lower mantle. Philosophical Transactions of the Royal Society A, 363(1837): 2811-2835.

Brechet YJM (1994) Clusters, plasticity and damage: a missing link?. Material Science and Engineering, A175: 63-69.

Bruhn DF, Casey M (1997) Texture development in experimentally deformed two-phase aggregates of calcite and anhydrite. Journal of Structural Geology, 19(7): 909-925.

Bullen KE, (1947) An introduction to the theory of seismology. University Press, Cambridge.

Byerlee JD (1968) Brittle-Ductile Transition in Rocks. Journal of Geophysical Research, 73(14): 4741-4750.

Caglioti G, Paoletti A, Ricci FP (1958) Choice of collimators for a crystal spectrometer for neutron diffraction. Nuclear Instruments, 3: 223-228.

Cahn JW (1966) A model for connectivity in multiphase structures. Acta Metallurgica, 14: 477-480.

Carpenter MA, Hemley RJ, Mao HK (2000) High-pressure elasticity of stishovite and the P4(2)/mnm phase transition. Journal of Geophyical Research: Solid Earth, 105: 10807-10816.

Carrez P, Ferré D, Cordier P (2009) Peierls-Nabarro modelling of dislocations in MgO from ambient pressure to 100 GPa. Modelling Simulation in Materials Science and Engineering, 17: 035010.

Carter NL, Heard HC (1970) Temperature and rate dependent deformation of halite. American Journal of Science, 269: 193-249.

Chao ECT, Evans HT, Skinner FJ, Milton C (1961) Neighborite, $NaMgF_3$, a new mineral from the Green River Formation, South Ouray, Utah. The American Mineralogist, 46: 379-393.

Chao ECT, Fahey JJ, Littler J, Milton DJ (1962) Stishovite, SiO_2, a very high pressure new mineral from Meteor Crater, Arizona. Journal of Geophysical Research, 67: 419–421.

Chao ECT, Littler J (1963) Additional evidence for the impact origin of the Ries basin, Bavaria, Germany, Geological Society of America Abstracts, 127.

Chen J, Liu H, Martin CD, Parise JB, Weidner DJ (2005) Crystal chemistry of $NaMgF_3$ perovskite at high pressure and temperature. American Mineralogist, 90: 1534-1539.

Chen J, Weidner DJ, Vaughan MT (2002) The strength of $Mg_{0.9}Fe_{0.1}SiO_3$ perovskite at high pressure and temperature. Nature, 419: 824-700.

Chin GY, Mammel WL (1973) A theoretical examination of the plastic deformation of ionic crystals: II. Analysis of uniaxial deformation and axisymmetric flow for slip on {110}<110> and {100}<110> systems. Metallugical transactions. A, Physical metallurgy and materials science, 4(1): 335-340.

Christensen UR (1987) Some geodynamical effects of anisotropic viscosity. Geophysical Journal of Research of the Royal Astronomical Society, 91: 711-736.

Cohen RE (1991) Bonding and elasticity of stishovite SiO_2 at high pressure: Linearized augmented plane wave calculations. American Mineralogist, 76: 733-742.

Cohen RE, Mazin I, Isaak D (1997) Magnetic collapse in transition metal oxides at high pressure: implications for the earth. Science, 275(654): doi:10.1126/science.275.5300.654.

Conrad CP, Molnar P (1997) The growth of Rayleigh-Taylor-type instabilities in the lithosphere for various rheological and density structures. Geophysical Journal International, 129: 95-112.

Cordier P, Amodeo J, Carrez P (2012) Modelling the rheology of MgO under Earth's mantle pressure, temperature and strain rates. Nature, 481: 177-181.

Cordier P, Mainprice D, Mosenfelder JL (2004) Mechanical instability near the stishovite-$CaCl_2$ phase transition: implications for crystal preferred orientations and seismic properties. European Journal of Mineralogy, 16: 387–399.

Cordier P, Rubie DC (2001) Plastic deformation under extreme pressure using a multi-anvil apparatus. Materials Science and Engineering A, 309: 38–43.

Cordier P, Sharp TG (1998) Characterization of dislocations in stishovite by large angle convergent beam electron diffraction. Physics and Chemistry of Minerals, 25: 548–555.

Cordier P, Ungár T, Zsoldos L, Tichy G (2004) Dislocation creep in $MgSiO_3$ perovskite at conditions of the earth's uppermost lower mantle. Nature, 428: 837-840.

Cottaar S, Romanowicz B (2012) An unsually large ULVZ at the base of the mantle near Hawaii. Earth and Planetary Science Letters, 355: 213-222.

Cottaar S, Romanowicz B (2013) Observations of changing anisotropy across the southern margin of the African LLSVP. Geophysical Journal International, 195(2): 1184-1195.

Cottaar S, Li M, McNamara A, Wenk HR, Romanowicz B (2014) Synthetic seismic anisotropy models within a slab impinging on the core-mantle boundary. Geophysical Journal International, *in press*.

Covey-Crump SJ, Schofield PF, Daymond MR (2006) Using neutrons to investigate changes in strain partitioning between the phases during plastic yielding of calcite + halite composites. Physica B, 385-386: 946-948.

Crowhurst J, Brown J, Goncharov A, Jacobsen S (2008) Elasticity of (Mg,Fe)O through the spin transition of iron in the lower mantle. Science, 319: 451-453.

Dawson PR, Needleman A, Suresh S, (1994) Issues in the finite element modeling of polyphase plasticity. Material Science and Engineering, A175: 43-48.

Dawson PR, Wenk HR (2000) Texture of the upper mantle during convection. Philosophical Magazine A, 80(3): 573-598.

Day RB, Stokes RJ (1966) Mechanical behavior of polycrystalline magnesium oxide at high temperatures. Journal of the American Ceramic Society, 49(7):3 45-354.

Decker DL (1971) High pressure equation of state for NaCl, KCl, and CsCl. Journal of Applied Physics, 42(8): 3239-3244.

Delanney L, Jacques PJ, Kalidindi SR (2006) Finite element modeling of crystal plasticity with grains shaped as truncated octahedrons. International Journal of Plasticity, 22: 1879-1898.

Diard O, Leclereq S, Rousselier G, Cailletaud G (2005) Evaluation of finite element based analysis of 3D multicrystalline aggregates plasticity – application to crystal plasticity

model identification and the study of stress and strain fields near grain boundaries. International Journal of Plasticity, 21: 691.

Dierick M, Masschaele B, Van Hoorebeke L (2004) Octopus, a fast and user-friendly tomographic reconstruction package developed in LabView (R). Measurement Science and Technology, 15(7): 1366-1370.

Ding Y, Xu J (2005) Variable pressure-temperature neutron diffraction of wüstite (Fe 1-x O): absence of long-range magnetic order to 20 GPa. Applied Physics Letters, 86: 052505.

Dorogokupets PI (2002) Critical analysis of equations of state for NaCl. Geochemistry International, 40(Suppl. 1): S132-S144.

Doukhan N, Doukhan JC (1986) Dislocations in perovskites $BaTiO_3$ and $CaTiO_3$. Physics and Chemistry of Minerals, 13: 403-410.

Du Z, Miyagi L, Amulele G, Lee KKM (2013) Efficient graphite ring heater suitable for diamond-anvil cells to 1300 K. Review of Scientific Instruments, 84: 024502.

Dubrovinsky L, Dubrovinskaia N, Saxena S, LiBehan T, (2000) X-ray diffraction under non-hydrostatic conditions in experiments with diamond anvil cell: wustite (FeO) as an example. Material Science and Engineering A, 288: 187-190.

Duffy TS, Hemley RJ, Mao HK (1995) Equation of state and shear strength at multimegabar pressures: magnesium oxide to 227 GPa. Physical Review Letters, 74(8): 1371-1374.

Dziewonski AM, Anderson DL (1981) Preliminary reference Earth model. Physics of the Earth and Planetary Interiors, 25: 297-356.

Efimov AF, Es'kova EM, Kataeva ZT (1967) The first discovery of neighborite in the USSR. Doklady (Akademiia Nauk SSSR): Earth Science Sections, 174: 140-142.

El Goresy A, Dubrovinsky L, Sharp TG, ChenM (2004). Stishovite and post-stishovite polymorphs of silica in the Shergotty meteorite: their nature, petrographic settings versus theoretical predictions and relevance to Earth's mantle. Journal of Physics and Chemistry of Solids, 65: 1597–1608.

Eshelby JD (1957) The determination of the elastic field of an ellipsoidal inclusion, and related problems. Proceedings of the Royal Society A, 241(1226): 376-396.

Faccenda M (2014) Mid mantle seismic anisotropy around subduction zones. Physics of the Earth and Planetary Interiors, 227: 1-19.

Farla RJM, Karato S, Cai Z (2013) Role of orthopyroxene in rheological weakening of the lithosphere via dynamic recrystallization. Proceedings of the National Academy of Sciences, 110(41): 16355-16360.

Fei Y (1996) Crystal chemistry of FeO at high pressure and temperature, in Mineral Spectroscopy: A Tribute to Roger G. Burns, M. D. Dyar, C. McCammon, and M. W. Schaefer Houston, TX pp 243-254.

Fei Y, Mao HK (1994) In situ determination of the NiAs phase of FeO at high pressure and temperature. Science, 266(5191): 1678-1680.

Fei Y, Zhang L, Corgne A, Watson H, Ricolleau A, Meng Y, Prakapenka V (2007) Spin transition and equations of state of (Mg,Fe)O solid solutions. Geophysical Research Letters, doi: 10.1029/2007GL030712.

Foitzik A, Skrotzki W, Haasen P (1989) Correlation between microstructure, dislocation dissociation and plastic anisotropy in ionic crystals. Material Science and Engineering A, 113: 399-407.

Franssen RCMW (1994) The rheology of synthetic rocksalt in uniaxial compression. Tectonophysics, 233: 1-40.

Frost HJ, Ashby MF (1982) Deformation-mechanism maps: The plasticity and creep of metals and ceramics. Pergamon Press, New York.

Garnero EJ, McNamara AK (2008) Structure and dynamics of Earth's lower mantle. Science, 320: 626-628.

Gerken J., Dawson P., 2008. A crystal plasticity model that incorporates stresses and strains due to slip gradients. Journal of the Mechanics and Physics of Solids, 56: 1651-1672.

Gramsch S, Cohen R, Savrasov S (2003) Structure, metal-insulator transitions, and magnetic properties of FeO at high pressures. American Mineralogist, 88: 257-261.

Green HW (1980) On the thermodynamics of non-hydrostatically stressed solids. Philosophical Magazine A, 41(5): 637-647.

Griggs DT (1936) The factor of fatigue in rock exfoliation. The Journal of Geology, 44(7): 783-796.

Gueddim A, Bouarissa N, Villesuzanne A (2009) First-principles determination of structural properties of MgO. Physica Scripta, 80: 055702.

Hammersley A, Svensson S, Hanfland M, Fitch A, Häusermann D (1996) Two-dimensional detector software: from real detector to idealised image two-theta scan. High Pressure Research, 14: 235-248.

Handy (1994) Flow laws for rocks containing two non-linear viscous phases: a phenomenological approach. Journal of Structural Geology, 16(3): 287-301.

Hansen LN, Zimmerman ME, Kohlstedt DL (2012) Laboratory measurements of the viscous anisotropy of olivine aggregates. Nature, 492: 415-418.

Heidelbach F, Stretton I, Langenhorst F, Mackwell S (2003) Fabric evolution during high shear strain deformation of magnesiowüstite ($Mg_{0.8}Fe_{0.2}O$). Journal of Geophysical Research, 108(B3): 2154.

Hemley RJ, Mao HK, Gramsch SA (2000). Pressure-induced transformations in deep mantle and core minerals. Mineralogical Magazine, 64(2): 157-184.

Herwegh M, Berger A (2004) Deformation mechanisms in second-phase affected microstructures and their energy balance. Journal of Structural Geology, 26: 1483-1498.

Herwegh M, Linckens J, Ebert A, Berger A, Brodhag SH (2011) The role of second phases for controlling microstructural evolution in polymineralic rocks: A review. Journal of Structural Geology, 33: 1728-1750.

Hess HH (1964) Seismic anisotropy of uppermost mantle under oceans. Nature, 203(494): 629-631.

Hirth JP, Lothe J (1982) *Theory of dislocations*. J. Wiley and Sons, New York.

Hirth G, Tullis J (1992) Dislocation creep regimes in quartz aggregates. Journal of Structural Geology, 14(2): 145-159.

Hobbs BE (1984) Point defect chemistry of minerals under a hydrothermal environment. Journal of Geophysical Research, 89(B6): 4026-4038.

Hofmann AW (1997) Mantle geochemistry: the message from oceanic volcanism. Nature, 385: 219-229.

Holyoke CW, Tullis J (2006) Mechanisms of weak phase interconnection and the effects of phase strength contrast on fabric development. Journal of Structural Geology, 28: 621-640.

Honneff H, Mecking H (1981) A method for the determination of the active slip systems and orientation changes during single crystal deformation. In: Gottstein G, Lücke K (eds) Textures of Materials, Berlin, pp 265-275.

Irifune T, Shinmei T, McCammon C, Miyajima N, Rubie D, Frost D (2010) Iron partitioning and density changes in pyrolite in Earth's lower mantle. Science, 327: 193-195.

Jackson I, Khanna S, Revcolevschi A, Berthon J (1990) Elasticity, shear-mode softening and high-pressure polymorphism of wustite ($Fe_{1-x}O$). Journal of Geophysical Research, 21: 671-685.

Jackson I, Ringwood AE (1981) High-pressure polymorphism of the iron oxides. Geophysical Journal of the Royal Astronomical Society, 64: 767-783.

Jacobsen S, Spetzler H, Reichmann H, Smyth J (2004) Shear waves in the diamond-anvil cell reveal pressure-induced instability in (Mg,Fe)O. Proceedings of the National Academy of Sciences, 101(16): 5867-5871.

Jeanloz R, Thompson A (1983) Phase transitions and mantle discontinuities. Review of Geophysics, 21: 51-74.

Jeanloz R, Sato-Sorensen Y (1986) Hydrostatic compression of $Fe_{1-x}O$ wüstite. Journal of Geophysical Research, 91: 4665-4672.

Ji S, Wang Z, Wirth R (2001) Bulk flow strength of forsterite-enstatite composites as a function of forsterite content. Tectonophysics, 341: 69-93.

Jiang F, Gwanmesia G, Dyuzheva T, Duffy T (2009). Elasticity of stishovite and acoustic mode softening under high pressure by Brillouin scattering. Physics of the Earth and Planetary Interiors, 172: 235-240.

Joswig W, Stachel T, Harris JW, Baur WH, Brey GP (1999). New Ca-silicate inclusions in diamonds – tracers from the lower mantle. Earth and Planetary Science Letters, 173: 1-6.

Jung H, Karato S (2001) Effects of water on dynamically recrystallized grain-size of olivine. Journal of Structural Geology, 23(9): 1337-1344.

Kaercher P, Speziale S, Miyagi L, Kanitpanyacharoen W, Wenk HR (2012) Crystallographic preferred orientation in wüstite (FeO) through the cubic-to-rhombohedral phase transition. Physics and Chemistry of Minerals, 39: 613-626.

Kamb WB (1959) Theory of preferred crystal orientation developed by crystallization under stress. The Journal of Geology, 67(2): 153-170.

Kanitpanyacharoen W, Parkinson DY, De Carlo F, Marone F, Stampanoni M, Mokso R, MacDowell A, Wenk HR (2013) Acomparative study of X-ray tomographic microscopy on shales at different synchrotron facilities: ALS, APS and SLS. Journal of Synchrotron Radiation, 20: 172-180.

Kantor A, Jacobsen S, Kantor I, Dubrovinsky L, McCammon C, Reichmann H, Goncharenko I (2004b) Pressure-induced magnetization in FeO: evidence from elasticity and Mössbauer spectroscopy. Physical Review Letters, doi:10.1103/93.215502.

Kantor I, Dubrovinsky L, McCammon C, Dubrvinskaia N, Goncharenko I, Kantor A, Kuznetsov A, Crichton W (2007) FeO and MnO high-pressure phase diagrams: relations between structural and magnetic properties. Phase Transitions, 80: 1151-1163.

Kantor I, Dubrovinsky L, McCammon C, Kantor A,Pascarelli S, Aquilanti G, Crichton W, Mattesini M, Ahuja R, Almeida J, Urusov V (2006) Pressure-induced phase transition in $Mg_{0.8}Fe_{0.2}O$ ferropericlase. Physics and Chemistry of Minerals, 33: 35-44.

Kantor I, McCammon C, Dubrovinsky L (2004a) Mössbauer spectroscopic study of pressure-induced magnetisation in wüstite (FeO). Journal of Alloys and Compounds, 376: 5-8.

Karato S, Weidner DJ (2008) Laboratory studies of the rheological properties of minerals under deep-mantle conditions. Elements, 4(3): 191-196.

Karato S, Zhang S, Wenk HR (1995) Superplasticity in Earth's lower mantle: evidence from seismic anisotropy and rock physics. Science, 270(5235): 458-461.

Karki BB, Warren MC, Stixrude L, Ackland GJ, Crain J (1997). Ab initio studies of high-pressure structural transformations in silica. Physical Review B: Condensed Matter, 55: 3465-3471.

Kawai K, Geller RJ (2010) The vertical flow in the lowermost mantle beneath the Pacific from inversion of seismic waveforms for anisotropic structure. Earth and Planetary Science Letters, 297(1-2): 190-198.

Kellogg LH, Hager BH, van der Hilst RD (1999) Compositional stratification in the deep mantle. Science, 283(5409): 1881-1884.

Kendall JM (2013) Seismic anisotropy in the boundary layers of the mantle. In: Karato SI, Forte A, Liebermann R, Masters G, Stixrude (eds) Earth's deep interior: Mineral physics and tomography from the atomic to the global scale. American Geophysical Union, Washington, DC, pp 133.

Kendall JM, Silver PG (1996) Constraints from seismic anisotropy on the nature of the lowermost mantle. Nature, 381(6581): 409-412.

Kesson SE, Fitz Gerald JD, Shelley JMG (1994) Mineral chemistry and density of subducted basaltic crustal at lower-mantle pressures. Nature, 372: 767-769.

Kimizuka H, Ogata S, Li J, Shibutani Y (2007). Complete set of elastic constants of α-quartz at high pressure: A first-principles study. Physical Review B, 75: 054109.

Kingma KJ, Cohen RE, Hemley RJ, Mao HK (1995). Transformation of stishovite to a denser phase at lower-mantle pressures. Nature, 374: 243-245.

Kingma KJ, Mao HK, Hemley RJ (1996). Synchrotron X-ray diffraction of SiO_2 to multimegabar pressures. High Pressure Research, 14:363-374.

Kinsland GL, Bassett WA (1977) Strength of MgO and NaCl polycrystals to confining pressures of 250 kbar at 25°C. Journal of Applied Physics, 48(3): 978-985.

Kirby S, Kronenberg A (1987) Rheology of the lithosphere; selected topics. Review of Geophysics, 25(6): 1219-1244.

Koch PS, Christie JM (1989) Effect of water on the rheology of experimentally deformed quartzite. Journal of Geophysical Research, 94(B10): 13875-13996.

Koči L, Vitos L, Ahuja R (2007) Ab initio calculations of the elastic properties of ferropericlase $Mg_{1-x}Fe_xO$ ($x<0.25$). Physics of the Earth and Planetary Interiors, 164: 177-185.

Kocks UF, Canova GR (1981) How many slip systems and which? In: Hansen N et al. (eds) Deformation of Polycrystals, Risø National Lab, Roskilde, Denmark, pp 35-44.

Kocks UF, Tomé C, Wenk HR (1998) Texture and anisotropy: preferred orientations in polycrystals and their effect on materials properties. Cambridge, United Kingdom, pp 564-567.

Kondo T, Ohtani E, Hirao N, Yagi T, Kikegawa T (2004) Phase transitions of (Mg,Fe)O at megabar pressures. Physics of the Earth and Planetary Interiors, 143-144: 201-213.

Kronenberg AK, Tullis J (1984) Flow strengths of quartz aggregates: Grain size and pressure effects due to hydrolytic weakening. Journal of Geophysical Research, 89(B6): 4281-4297.

Kustowski B, Ekström G, Dziewoński AM (2008) Anisotropic shear-wave velocity structure of the Earth's mantle: A global model. Journal of Geophysical Research, 113: B06306.

Lay T, Garnero EJ (2004) Core-mantle boundary structures and processes. In: Sparks RSJ, Hawkesworth CJ (ed) State of the planet: Frontiers and challenges in geophysics. Geophysical Monograph Series, Sapporo, Japan, 150, pp 25-41.

Lay T, Williams Q, Garnero E (1998) The core-mantle boundary layer and deep Earth dynamics. Nature, 392: 461-468.

Lebensohn RA (2001) N-site modeling of a 3D viscoplastic polycrystal using fast Fourier transform. Acta Materialia, 49: 2723-2737.

Lebensohn RA, Brenner R, Castelnau O, Rollett AD (2008) Orientation image-based micromechanical modelling of subgrain texture evolution in polycrystalline copper. Acta Materialia, 56: 3914-3926.

Lebensohn RA, Dawson PR, Kern HM, Wenk HR (2003) Heterogeneous deformation and texture development in halite polycrystals: comparison of different modeling approaches and experimental data. Tectonophysics, 370: 287-311.

Lebensohn RA, Kanjarla AK, Eisenlohr P (2012) An elasto-viscoplastic formulation based on fast Fourier transforms for the prediction of micromechanical fields in polycrystalline materials. International Journal of Plasticity, 32-33: 59-69.

Lebensohn RA, Tomé CN (1993) A self-consistent anisotropic approach for the simulation of plastic deformation and texture development of polycrystals: Application to zirconium alloys. Acta Metallurgica Materialia, 41(9): 2611-2624.

Lebensohn RA, Tomé CN (1994) A self-consisten viscoplastic model: prediction of rolling textures of anisotropic polycrystals. Material Science and Engineering A, 175: 71-82.

Lebensohn RA, Tome CN, Ponte Castaneda P (2007) Self-consistent modeling of the mechanical behavior of viscoplastic polycrystals incorporating intragranular field fluctuations. Philosophical Magazine, 87: 4287-4322.

Lee CY, Gonze X (1997). SiO_2 stishovite under high pressure: Dielectric and dynamical properties and the ferroelastic phase transition. Physical Review B: Condensed Matter, 56: 7321-7330.

Lev E, Hager BH (2011) Anisotropic viscosity changes subduction zone thermal structure. Geochemistry Geophysics Geosystems, 12: Q04009.

Lewis MH, Bright MWA (1985) Transformation twinning in synthetic neighborite. The American Mineralogist, 56: 1519-1526.

Li L, Addad A, Weidner D, Long H, Chen J (2007) High pressure deformation in two-phase aggregates. Tectonophysics, 439: 107-117.

Li L, Brodholt JP, Stackhouse S, Weidner DJ, Alfredsson M, Price GD (2005) Elasticity of (Mg,Fe)(Si,Al))O_3-perovskite at high pressure. Earth and Planetary Science Letters, 240: 529-536.

Li L, Weidner DJ, Chen J, Vaughan MT, Davis M, Durham WB (2004) X-ray strain analysis at high pressure: Effect of plastic deformation in MgO. Journal of Applied Physics, 95(12): 8357-8365.

Li X, Jeanloz R (1987) Measurement of the B1-B2 transition pressure in NaCl at high temperatures. Physical Review B, 36(1): 474-479.

Liermann HP, Merkel S, Miyagi L, Wenk HR, Shen G, Cynn H, Evans WJ (2009) Experimental method for *in situ* determination of material textures at simultaneous high pressure and high temperature by means of radial diffraction in the diamond anvil cell. Review of Scientific Instruments, 80: 104501.

Lin JF, Heinz D, Mao HK, Hemley R, Devine J, Li J, Shen G (2003) Stability of magnesiowüstite in Earth's lower mantle. Proceedings of the National Academy of Sciences, 100: 4405-4408.

Lin JF, Mao Z, Yavaş H, Zhao J, Dubrovinsky L (2010). Shear wave anisotropy of textured hcp-Fe in the Earth's inner core. Earth and Planetary Science Letters, 298: 361-355.

Lin JF, Speziale S, Mao Z, Marquardt H (2013) Effects of the electronic spin transitions of iron in lower mantle minerals: Implications for deep mantle geophysics and geochemistry. Review of Geophysics, 51: 244-275.

Lin JF, Struzhkin V, Jacobsen S, Hu M, Chow P, Kung J, Liu H, Mao HK, Hemley R (2005a) Spin transition of iron in magnesiowüstite in the Earth's lower mantle. Nature, 436: 377-380.

Lin JF, Struzhkin V, Jacobsen S, Shen G, Prakapenka V, Mao HK, Hemley R (2005b) X-ray emission spectroscopy with a laser-heated diamond anvil cell: a new experimental probe of the spin state of iron in the Earth's interior. Journal of Synchrotron Radiation, 12: 637-641.

Lin JF, Wenk HR, Voltolini M, Speziale S, Shu J, Duffy TS (2009) Deformation of lower-mantle ferropericlase (Mg,Fe)O across the electronic spin transition. Physics and Chemistry of Minerals, 36(10): 585-592.

Linckens J, Herwegh M, Müntener O, Mercolli I (2011) Evolution of a polymineralic mantle shear zone and the role of second phases in the localization of deformation. Journal of Geophysical Research, 116: B06210.

Liu HZ, Chen J, Hu J, Martin CD, Weidner DJ, Häusermann D, Mao HK (2005) Octahedral tilting evolution and phase transition in orthorhombic $NaMgF_3$ perovskite under pressure. Geophysical Research Letters, 32: L04304.

Liu L, Zhang J, Green HW II, Jin Z, Bozhilov KN (2007). Evidence of former stishovite in metamorphosed sediments, implying subduction to >350 km. Earth and Planetary Science Letters, 263: 180-191.

Lonardelli I, Gey N, Wenk HR, Humbert M, Vogel S, Lutterotti L (2007) In situ observation of texture evolution during $\alpha \rightarrow \beta$ and $\beta \rightarrow \alpha$ phase transformations in titanium alloys investigated by neutron diffraction. Acta Materialia, 55: 5718-5727.

Long MD, Xiao X, Jiang Z, Evans B, Karato S (2006) Lattice preferred orientation in deformed polycrystalline (Mg,Fe)O and implications for seismic anisotropy in D''. Physics of the Earth and Planetary Interiors, 156: 75-88.

Lutterotti L, Matthies S, Wenk HR (1997) Combined texture and structure analysis of deformed limestone from time-of-flight neutron diffraction spectra. Journal of Applied Physics, 81(2): 594-600.

Lutterotti L, Matthies S, Wenk HR, Schultz AS, Richardson JW Jr. (1997) Combined texture and structure analysis of deformed limestone from time-of-flight neutron diffraction spectra. Journal of Applied Physics, 81(2): 594-600.

Lutterotti L, Scardi P (1990) Simultaneous structure and size-strain refinement by the Rietveld method. Journal of Applied Crystallography, 23: 246-252.

Lutterotti L, Vasin R, Wenk HR (2014) Rietveld texture analysis from synchrotron diffraction images: I. Calibration and basic analysis. Powder Diffraction, *in press*.

Madi K, Forest S, Cordier P, Boussuge M (2005) Numerical study of creep in two-phase aggregates with a large rheology contrast: Implications for the lower mantle. Earth and Planetary Science Letters, 237: 223-238.

Mainprice D, Tommasi A, Ferre D, Carrez P, Cordier P (2008) Predicted glide sstems and crystal preferred orientations of polycrystalline silicate Mg-Perovskite at high pressure: Implications for the seismic anisotropy in the lower mantle. Earth and Planetary Science Letters, 271: 135-144.

Manga M, Jeanloz R (1996) Axial temperature gradients in dielectric samples in the laser-heated diamond cell. Geophysical Research Letters, 23(14): 1845-1848.

Mao HK, Shu J, Fei Y, Hu J, Hemley R (1996) The wustite enigma. Physics of the Earth and Planetary Interiors, 96: 135-145.

Mao W, Shu J, Fei Y, Hu J, Hemley R, Mao HK (2002) Displacive transition in magnesiowüstite. Journal of Physics: Condensed Matter, 14: 11349-11354.

Mao Z, Lin JF, Liu J, Prakapenka V (2011) Thermal equation of state of lower-mantle ferropericlase across the spin crossover. Geophysical Research Letters, 38: L23308.

Marquardt H, Speziale S, Reichmann H, Frost D, Schilling F, Garnero E (2009) Elastic shear anisotropy of ferropericlase in earth's lower mantle. Science, 324 doi:10.1126/science.1169365

Martin CD, Crichton WA, Liu H, Prakapenka V, Chen J, Parise JB (2006). Phase transitions and compressibility of $NaMgF_3$ (Neighborite) in pervoskite- and post-perovskite-related structures. Geophysical Research Letters, 33: L11305.

Martini JEJ (1978). Coesite and stishovite in the Vredefort Dome, South Africa. Nature, 272: 715-717.

Martini JEJ (1991). The nature, distribution and genesis of coesite and stishovite associated with pseudotachylite of the Vredefort Dome, South Africa. Earth and Planetary Science Letters, 103: 285-300.

Matsui M, Price GD (1991) Simulation of the pre-melting behaviour of $MgSiO_3$ perovskite at high pressures and temperatures. Nature, 351: 735-737.

Matsui T, Shigematsu H, Arita Y, Hanajiri Y, Nakamitsu N, Nagasaki T (1997) High temperature phase transitions of $CaTiO_3$ and $(Ca_{0.85}Nd_{0.15})TiO_3$ by X-ray diffractometry and differential thermal analysis. Journal of Nuclear Materials, 247: 72-75.

Matthies S, Priesmeyer HG, Daymond MR (2001) On the diffractive determination of single-crystal elastic constants using polycrystalline samples. Journal of Applied Crystallography, 34: 585-601.

Matthies S, Vinel GW (1982a) On the reproduction of the orientation distribution function of textured samples from reduced pole figures using the concept of conditional ghost correction. Physica Status Solidi B, 112: K111-K114.

Matthies S, Vinel GW (1982b) An example demonstrating a new reproduction method of the ODF of texturized samples from reduced pole figures. Physica Status Solidi B, 112: K115-K120.

Mazin II, Fei Y, Downs R, Cohen R (1998) Possible polytypism in FeO at high pressures. American Mineralogist, 83: 451-457.

McDonnell RD, Peach CJ, van Roermund HLM, Spiers CJ (2000) Effect of varying enstatite content on the deformation behavior of fine-grain synthetic peridotite under wet conditions. Journal of Geophysical Research, 105: 13,535-13,553.

McDonough WF, Sun S (1995) The composition of the earth. Chemical Geology, 120: 223-253.

McNamara AK, van Keken PE, Karato SI (2002) Development of anisotropic structure in the Earth's lower mantle by solid-state convection. Nature, 416(6878): 310-314.

McNamara AK, van Keken PE, Karato SI (2003) Development of finite strain in the convection lower mantle and its implications for seismic anisotropy. Journal of Geophysical Research-Solid Earth, 108(B5): 2230.

Meade C, Jeanloz R (1988) Yield strength of MgO to 40 GPa. Journal of Geophysical Research, 93: 3261-3269.

Meade C, Silver PG, Kaneshima S (1995) Laboratory and seismological observations of lower mantle isotropy. Geophysical Research Letters, 22(10): 1293-1296.

Mehl L, Hirth G (2008) Plagioclase preferred orientation in layered mylonites: Evaluation of flow laws for the lower crust. Journal of Geophysical Research, 113: B05202.

Menendez-Proupin E, Singh A (2007) Ab initio calculations of elastic properties of compressed Pt. Physical Review B, doi:10.1103/76.054117.

Meng Y, Shen G, Mao HK (2006) Double-sided laser heating system at HPCAT for *in situ* x-ray diffraction at high pressures and high temperatures. Journal of Physics: Condensed Matter, 18: S1097-S1103.

Merkel S, Tomé C, Wenk HR (2009) Modeling analysis of the influence of plasticity on high pressure deformation of hcp-Co. Physical Review B, doi:10.1103/79.064110.

Merkel S, Wenk HR, Badro J, Montagnac G, Gillet P, Mao HK, Hemley RJ (2003) Deformation of $(Mg_{0.9},Fe_{0.1})SiO_3$ perovskite aggregates up to 32 GPa. Earth and Planetary Science Letters, 209: 351-360.

Merkel S, Wenk HR, Shu J, Shen G, Gillet P, Mao HK, Hemley RJ (2002) Deformation of polycrystalline MgO at pressures of the lower mantle. Journal of geophysical research, 107 (B11): 2271.

Michel JC, Moulinec H, Suquet P (2001) A computation scheme for linear and non-linear composites with arbitrary phase contrast. International Journal for Numerical Methods in Engineering, 52: 139-160.

Michel JC, Moulinec H, Suquet P (2000) A computational method based on augmented Lagrangians and fast Fourier transforms for composites with high contrast. Computer Modeling in Engineering and Sciences, 1(2): 79-88.

Mika DP, Dawson PR (1998) Effects of grain interaction on deformation in polycrystals. Materials Science and Engineering, A 257: 62-76.

Miyagi LM (2009) Deformation and texture development in deep earth mineral phases: Implications for seismic anisotropy and dynamics. Dissertation, University of California, Berkeley.

Miyagi L, Kanitpanyacharoen W, Vennila S, Kaercher P, Knight, J, MacDowell A, Wenk HR, Williams Q, Zepeda Alarcon E (2013) Combined resistive and laser heating technique for in situ radial X-ray diffraction in the diamond anvil cell at high pressure and temperature. Review of Scientific Instruments, 84(2): 025118.

Miyagi L, Kunz M, Knight J, Nasiatka J, Voltolini M, Wenk HR (2008) In situ phase transformation and deformation of iron at high pressure and temperature. Journal of Applied Physics, 104: 103510.

Miyagi L, Merkel S, Yagi T, Sata N, Ohishi Y, Wenk HR (2009) Diamond anvil cell deformation of $CaSiO_3$ perovskite up to 49 GPa. Physics of the Earth and Planetary Interiors, 174: 159-164.

Miyajima N, Yagi T, Ichihara M (2009) Dislocation microstructures of $MgSiO_3$ perovskite at high pressure and temperature condition. Physics of the Earth and Planetary Interiors, 174: 153-158.

Molinari A, Canova GR, Ahzi S (1987) A self consistent approach of the large deformation polycrystal viscoplasticity. Acta Metallurgica, 35(12): 2983-2994.

Moulinec H, Suquet P (1998) A numerical method for computing the overall response of nonlinear composites with complex microstructure. Computer Methods in Applied Mechanics and Engineering, 157: 69-94.

Moulinec H, Suquet P (1994) A fast numerical-method for computing the linear and nonlinear mechanical-properties of composites. Comptes rendus de l'Académie des sciences. Série 2. Méchanique, physique, chimie, astronomie, 318(11): 1417-1423.

Moulinec H, Suquet P (1995) A FFT-based numerical method for computing the mechanical properties of composites from images of their microstructures. Solid Mechanics and Its Applications, 37: 235-246.

Murakami M, Hirose K, Kawamura K, Sata N, Ohishi Y (2004) Post-perovskite phase transition in $MgSiO_3$. Science, 304(5672): 855-858.

Murakami M, Hirose K, Ono S, Tsuchiya T, Isshiki M, Watanuki T (2004) High pressure and high temperature phase transitions of FeO. Physics of the Earth and Planetary Interiors, 146: 273-282.

Oganov AR, Ono S (2004) Theoretical and experimental evidence for a post-perovskite phase of $MgSiO_3$ in Earth's D'' layer. Nature, 430: 445-448.

Ohta K, Cohen R, Hirose K, Haule K, Shimizu K, Ohishi Y (2012) Experimental and theoretical evidence for pressure-induced metallization in FeO with rocksalt-type structure. Physical Review Letters, 108: 026403.

O'Keeffe M, Hyde BG, Bovin JO (1979) Contribution to the crystal-chemistry of orthorhombic perovskites – $MgSiO_3$ and $NaMgF_3$. Physics and Chemistry of Minerals, 4: 299-305.

Ozawa H, Takahashi F, Hirose K, Ohishi Y, Hirao N (2011) Phase transition of FeO and stratification in Earth's outer core. Science, 334 doi: 10.1126.

Panning M, Romanowicz B (2004) Inferences on flow at the base of Earth's mantle based on seismic anisotropy. Science, 303(5656): 351-353.

Panning M, Romanowicz B (2006) A three-dimensional radially anisotropic model of shear velocity in the whole mantle. Geophysical Journal International, 167(1): 361-379.

Pasternak M, Taylor R, Jeanloz R, Li X, Nguyen J, McCammon C (1997) High pressure collapse of magnetism in $Fe_{0.94}O$: Mössbauer spectroscopy beyond 100 GPa. Physical Review Letters, 79(25): 5046-5049.

Paterson M, Weaver C (1970) Deformation of polycrystalline MgO under pressure. Journal of the American Ceramic Society, 53(8): 463-471.

Pischedda V, Ferraris G, Raade G (2005) Single-crystal X-ray diffraction study on neighborite (NaMgF3) from Gjerdingselva, Norway. Neues Jahrbuch für Mineralogie Abhandlungen, 812(1): 23-29.

Poirier JP, Peyronneau J, Gesland JY, Brebec G (1983) Viscosity and conductivity of the lower mantle; an experimental study on a $MgSiO_3$ perovskite analogue, $KZnF_3$. Physics of the Earth and Planetary Interiors, 32: 273-287.

Prakapenka V, Kubo A, Kuznetsov A, Laskin A, Shkurikhin O, Dera P, Rivers ML, Sutton SR (2008) Advanced flat top laser heating system for high pressure research at GSECARS: application to the melting behavior of germanium. High Pressure Research, 28(3): 225-235.

Prakapenka V, Shen G, Dubrovisky L S, Rivers M L, Sutton S R (2004) High pressure induced phase transformationof SiO_2 and GeO_2: difference and similarity. Journal of Physics and Chemistry of Solids, 65: 1537-1545.

Redfern SAT (1996) High-temperature structural phase transitions in perovskite ($CaTiO_3$). Journal of Physics: Condensed Matter, 8: 8267-8275.

Rietveld HM (1969). A profile refinement method for nuclear and magnetic structures. Journal of Applied Crystallography, 2: 65-71.

Ringwood AE (1991) Phase transitions and their bearing on the constitution and dynamics of the mantle. Geochimica et Cosmochimica Acta, 55: 2083–2110.

Rollett AD, Lebensohn RA, Groeber M, Choi Y, Li J, Rohrer GS (2010) Stress hot spots in viscoplastic deformation of polycrystals. Modelling and Simulations in Materials Science and Engineering, 18: 074005.

Ross N, Shu J-F, Hazen RM (1990) High-pressure crystal chemistry of stishovite. American Mineralogist, 75: 739–747.

Routbort JL (1979) Work hardening and creep of MgO. Acta Metallurgica 27: 649-661.

Sachs G (1928) On the derivation of a condition of flowing. Zeitschrift des Vereines Deutscher Ingenieure, 72: 734-736.

Salje E (1990) Phase transitions in ferroelastic and co-elastic crystals. Ferroelectrics, 104: 111-120.

Schmid E, Boas W (1935) Plasticity of crystals with special reference to metals. Translated by F.A. Hughes and Co. Limited (1950), London.

Shen G, Rivers ML, Wang Y, Sutton SR (2001). Laser heated diamond cell system at the Advanced Photon Source for in situ x-ray measurements at high pressure and temperature. Review of Scientific Instruments, 72: 1273-1282.

Shim S, Duffy T, Jeanloz R, Shen G (2004) Stability and crystal structure of $MgSiO_3$ perovskite to the core-mantle boundary. Geophysical Research Letters, 31(10): L10603.

Shim SH, Duffy T, Kenichi T (2002) Equation of state of gold and its application to the phase boundaries near 660 km depth in Earth's mantle. Earth and Planetary Science Letters, 203: 729-739.

Shimizu I (1992) Nonhydrostatic and nonequilibrium thermodynamics of deformable materials. Journal of Geophysical Research 97(4): 4587-4597.

Shoemaker EM, Chao ECT (1961) New evidence for the impact origin of the Ries Basin, Bavaria, Germany. Journal of Geophysical Research, 66: 3371–3378.

Shu J, Mao HK, Hu J, Fei Y, Hemley R (1998) Single-crystal X-ray diffraction of wüstite to 30 GPa hydrostatic pressure. Neues Jahrbuch für Mineralogie Abhandlungen, 172: 309-323.

Sinclair W, Ringwood AE (1978) Single crystal analysis of the structure of stishovite. Nature 272:714–715.

Singh AK, Balasingh C, Mao HK, Hemley R, Shu J (1998) Analysis of lattice strains measured under nonhydrostatic pressure. Journal of Applied Science, 83(12): 7567-7575.

Skemer P, Karato S (2008) Sheared lherzolite xenoliths revisted. Journal of Geophysical Research, 113: B07205.

Skemer P, Warren JM, Kelemen PB, Hirth G (2010) Microstructural and rheological evolution of a mantle shear zone. Journal of Petrology, 51(1,2): 43-53.

Skrotzki W, Haasen P (1981) Hardening mechanisms of ionic=crystals on (110) and (100) slip planes. Journal de Physique (Paris), 42(6): 3119-3148.

Skrotzki W, Welch P (1983) Development of texture and microstructure in extruded ionic polycrystalline aggregates. Tectonophysics, 99: 47-61.

Speziale S, Lee V, Clark S, Lin J, Pasternak M, Jeanloz R (2007) Effects of Fe spin transition on the elasticity of (Mg, Fe)O magnesiowüstite and implications for the seismological properties of the Earth's lower mantle. Journal of Geophysical Research, 112: B10212.

Speziale S, Milner A, Lee V, Clark S, Pasternak M, Jeanloz R (2005) Iron spin transition in Earth's mantle. Proceedings of the National Academy of Sciences, 102(50): 17918-17922.

Srinivasan M, Stoeve TG (1974) Temperature dependence of yielding and work-hardening rates in magnesium oxide single crystals. Journal of Materials Science, 9: 121-128.

Steinberger B (2000) Slabs in the lower mantle – results of dynamic modeling compared with tomographic images and the geoid. Physics of the Earth and Planetary Interiors, 118: 241-257.

Stishov SM, Belov NV (1962) Crystal structure of a new dense modification of silica SiO_2. Proceedings of the USSR Academy of Sciences, 143(4): 951.

Stishov SM, Popova SV (1961) New dense polymorphic modification of silica. Geochemistry, 10: 923–926.

Stroh, AN (1958) Dislocations and cracks in anisotropic elasticity. Philosophical Magazine 3: 625-646.

Struzhkin V, Mao HK, Mao W, Hemley R, Sturhahn W, Alp E, L'abbe C, Hu M, Errandonea D (2004) Phonon density of states and elastic properties of Fe-based materials under compression. Hyperfine Interactions, 153: 3-15.

Tackley (2000) Mantle convection and plate tectonics: toward an integrated physical and chemical theory. Science, 288: 2002-2007.

Takeshita T, Wenk HR, Lebensohn R (1999) Development of preferred orientation and microstructure in sheared quartzite: Comparison of natural data and simulated results. Tectonophysics, 312(2-4): 133-155.

Tasaka M, Hiraga T (2013) Influence of mineral fraction on the rheological properties of forsterite + enstatite during grain-size-sensitive creep: 1. Grain size and grain growth laws. Journal of Geophysical Research, 118: 3970-3990.

Tasaka M, Hiraga T, Zimmerman ME (2013) Influence of mineral fraction on the rheological properties of forsterite + enstatite during grain-size-sensitive creep: 2. Deformation experiments. Journal of Geophysical Research: Solid Earth 118:3991-4012.

Taylor GI (1938) Plastic strain in metals, Journal of the Institute of Metals, 62: 307-324.

ter Heege JH, de Bresser JHP, Spiers CJ (2002) The influence of dynamic recrystallization on the grain size distribution and rheological behaviour of Carrara marble deformed in axial compression. In: de Meer S, Drury MF, de Bresser JHP (ed.) Deformation mechanisms, rheology and tectonics: Current status and future perspectives, Noordwijkerhout, Netherlands, 200, pp 331-353.

Teter DM, Hemley RJ, Kresse G, Hafner J (1998). High pressure polymorphism in silica. Physical Review Letters, 80(10): 2145-2148.

Texier M, Cordier P (2006) TEM characterization of dislocations and slip systems in stishovite deformed at 14 GPa, 1,300C in the multianvil apparatus. Physics and Chemistry of Minerals, 33: 394-402.

Tommaseo CE, Devine J, Merkel S, Speziale S, Wenk HR (2006) Texture development and elastic stresses in magnesiowüstite at high pressure. Physics and Chemistry of Minerals, 33: 84-97.

Tommasi A, Mainprice D, Canova G, Chastel Y (2000) Viscoplastic self-consistent and equilibrium-based modeling of olivine lattice preferred orientations: Implications for the upper mantle seismic anisotropy. Journal of Geophysical Research, 105(B4): 7893-7908.

Tsuchida Y, Yagi T (1989). A new, post-stishovite high-pressure polymorph of silica. Nature, 340: 217-220.

Tullis J (1970) Quartz: Preferred orientation in rocks produced by Dauphiné twinning. Science, 168: 1342-1344.

Tullis J (2002) Deformation of granitic rocks: Experimental studies and natural examples. In: Karato S, Wenk HR (eds.) Plastic deformation of minerals and rocks, Reviews in Mineralogy and Geochemistry, 51, pp 51-95.

Tullis J, Tullis T (1972). Preferred orientation of quartz produced by mechanical Dauphiné twinning: Thermodynamics and axial experiments. In: Flow and fracture of rocks. American Geophysical Union Geophysical Monograph, 16: 67-82.

Tullis J, Wenk HR (1994) Effect of muscovite on the strength and lattice preferred orientations of experimentally deformed quartz aggregates. Materials Science and Engineering A, 175: 209-220.

Turcotte DL, Oxburgh ER (1967) Finite amplitude convective cells and continental drift. Journal of Fluid Mechanics, 28(1):29-42.

Twiss RJ (1977) Theory and applicability of a recrystallized grain size paleopiezometer. Pure and Applied Geophysics, 115: 227-244.

Uchida T, Wang Y, Rivers ML, Sutton SR (2004) Yield strength and strain hardening of MgO up to 8 GPa measured in the deformation-DIA with monochromatic X-ray diffraction. Earth and Planetary Science Letters 226: 117-126.

Umemoto K, Wentzcovitch RM, Weidner DJ, Parise JB (2006) $NaMgF_3$: A low-pressure analog of $MgSiO_3$. Geophysical Research Letters, 33: L15304.

Vauchez A, Nicolas A (1991) Mountain building – strike-parallel motion and mantle anisotropy. Tectonophysics, 185(3-4): 183-201.

Vauchez A, Tommasi A, Barruol G (1998) Rheological heterogeneity, mechanical anisotropy and deformation of the continental lithosphere. Tectonophysics, 296: 61-86.

Vinnik L, Kato M, Kawakatsu H (2001) Search for seismic discontinuities in the lower mantle. Geophysical Journal International, 147: 41-56.

Voronoi GF (1908) Nouvelles applications des paramétres continus à la théorie de formes quadratiques. Journal für die reine und angewandte Mathematik, 134: 198-287.

Wang F, Tange Y, Irifune T, Funakoshi K (2012). P-V-T equation of state of stishovite up to mid-lower mantle conditions. Journal of Geophysical Research, 117: B06209.

Wang Y, Durham WB, Getting IC, Weidner DJ (2003) The deformation-DIA: A new apparatus for high temperature triaxial deformation in pressures up to 15 GPa. Review of Scientific Instruments, 74(6): 3002-3011.

Wang Y, Guyot F, Yeganeh-Haeri A, Liebermann RC (1990) Twinning in $MgSiO_3$ perovskite. Science, 248: 468-471.

Wang Y, Liebermann RC (1993) Electron microscopy study of domain structure due to phase transitions in natural perovskite. Physics and Chemistry of Minerals, 20: 147-158.

Wang YX, De Carlo F, Mancini DC, McNulty I, Tieman B, Bresnahan J, Foster I, Insley J, Lane P, von Laszewski G, Kesselman C, Su MH, Thiebaux M (2001) A high-throughput x-ray microtomography system at the Advanced Photon Source. Review of Scientific Instruments, 72(4): 2062-2068.

Wang ZC, Dupas-Bruzek C, Karato S (1999) High temperature creep of an orthorhombic perovskite – $YAlO_3$. Physics of the Earth and Planetary Interiors, 110: 51-69.

Warren JM, Hirth G (2006) Grain size sensitive deformation mechanisms in naturally deformed peridotites. Earth and Planetary Science Letters, 248: 438-450.

Wenk HR, Bortolotti M, Barton N, Oliver E, Brown D (2007). Dauphiné twinning and texture memory in polycrystalline quartz. Part 2: In situ neutron diffraction compression experiments. Physics and Chemistry of Minerals, 34: 599-607.

Wenk HR, Canova G, Molinari A (1989a) Viscoplastic modeling of texture development in quartzite. Journal of Geophysical Research, 94(B12): 895-906.

Wenk HR, Canova G, Molinari A, Mecking H (1989b) Texture development in halite: comparison of Taylor model and self-consistent theory. Acta Metallurgica Materialia, 37(7): 2017-2029.

Wenk HR, Christie J (1991) Comments on the interpretation of deformation textures in rocks, Journal of Structural Geology, 13(10): 1091-1110.

Wenk HR, Cottaar S, Tomé C, McNamara A, Romanowicz B (2011) Deformation of the lowermost mantle: from polycrystal plasticity to seismic anisotropy. Earth and Planetary Science Letters, 306: 33-45.

Wenk HR, Kaercher P, Kanitpanyacharoen W, Zepeda-Alarçon E, Wang Y (2013). Orientation relations during the α→ω phase transition of zirconium – in situ texture observations at high pressure and temperature. Physical Review Letters, 111: 195701.

Wenk HR, Lonardelli I, Merkel S, Miyagi L, Pehl J, Speziale S, Tommaseo C (2006b) Deformation textures produced in diamond anvil experiments, analyzed in radial diffraction geometry. Journal of Physics: Condensed Matter, 18: S933-S947.

Wenk HR, Lonardelli I, Pehl J, Devine J, Prakapenka V, Shen G, Mao HK (2004) In situ observation of texture development in olivine, ringwoodite, magnesiowüstite and silicate perovskite at high pressure. Earth and Planetary Science Letters, 226: 507-519.

Wenk HR, Lutterotti L, Kaercher P, Kanitpanyacharoen W, Miyagi L, Vasin R (2014b) Rietveld texture analysis from synchrotron diffraction images. II. Complex multiphase materials and diamond anvil cell experiments. Powder Diffraction, *in press.*

Wenk HR, Matthies S, Donovan J, Chateigner D (1998) Beartex: a Windows-based program system for quantitative texture analysis. Journal of Applied Crystallography, 31: 262-269.

Wenk HR, Pannetier J (1990) Texture development in deformed granodiorites from the Santa Rosa mylonite zone, southern California. Journal of Structural Geology, 12(2): 177-184.

Wenk HR, Rybacki E, Dresen G, Lonardelli I, Barton N, Franz H, Gonzalez G (2006a). Dauphiné twinning and texture memory in polycrystalline quartz. Part 1: Experimental deformation of novaculite. Physics and Chemistry of Minerals, 33: 667-676.

Wenk HR, Speziale S, McNamara AK, Garnero EJ (2006) Modeling lower mantle anisotropy development in a subducting slab. Earth and Planetary Science Letters 245: 302-314.

Wenk HR, Takeshita T, Vanhoutte P (1986) Plastic anisotropy and texture development in calcite polycrystals. Journal of Geophysical Research, 91(B3): 3861-3869.

Wenk HR, Vasin R, Lutterotti L (2014a) Rietveld texture analysis from synchrotron diffraction images: I. Basic analysis. Powder Diffraction, *in press*.

Wolf GH, Bukowinski MST (1985) *Ab initio* structural and thermoelastic properties of orthorhombic MgSiO3 perovskite. Geophysical Research Letters, 12(12): 809-812.

Wookey J, Kendall JM (2004) Evidence of midmantle anisotropy from shear wave splitting and the influence of shear-coupled *P* waves. Journal of Geophysical Research, 109: B07309.

Wookey J, Kendall JM, Barruol G (2002) Mid-mantle deformation inferred from seismic anisotropy. Nature, 415(6873): 777-780.

Wu P (2002) Effects of mantle flow law stress exponent on postglacial induced surface motion and gravity in Laurentia. Geophysics Journal International, 148: 676-686.

Yagi T, Suzuki T, Akimoto SI (1985) Static compression of wüstite ($Fe_{0.98}O$) to 120 GPa. Journal of Geophysical Research, 90(B10): 8784-8788.

Yamazaki D, Karato S (2001) Some mineral physics constraints on the rheology and geothermal structure of Earth's lower mantle. American Mineralogist, 86: 385-391.

Yamazaki D, Karato S (2002) Fabric development in (Mg,Fe)O during large strain, shear deformation: implications for seismic anisotropy in Earth's lower mantle. Physics of the Earth and Planetary Interiors, 131: 251-267.

Yashima M, Ali R (2009) Structural phase transition and octahedral tilting in the calcium titanate perovskite $CaTiO_3$. Solid State Ionics, 180: 120-126.

Yeganeh-Haeri A, Weidner DJ (1989) Single-crystal elastic moduli of magnesium metasilicate perovskite. In: Perovskite: A structure of great interest to geophysics and materials science. Geophysical Monograph Series, 45: 13-25.

Yoshino T, Yamazaki D, Ito Eiji, Katsura T (2008) No interconnection of ferro-periclase in post-spinel phase inferred from conductivity measurement. Geophysical Research Letters, 35: L22303.

Zhang S, Karato S (1995) Lattice preferred orientation of olivine aggregates deformed in simple shear. Nature, 375: 774-777.

Zhao Y, Weidner DJ (1993) The single crystal elastic moduli of neighborite. Physics and Chemistry of Minerals, 20: 419-424.

Zhao Y, Weidner DJ, Ko J, Leinenweber K, Liu X, Li B, Meng Y, Pacalo REG, Vaughan MT, Wang Y, Yeganeh-Haeri A (1994) Perovskite at high P-T conditions: An in situ synchrotron X ray diffraction study of $NaMgF_3$ perovskite. Journal of Geophysical Research, 99(B2): 2871-2885.

Zhuravlev K, Jackson J, Wolf A, Wicks J, Yan J, Clark S (2010) Isothermal compression behavior of (Mg,Fe)O using neon as a pressure medium. Physics and Chemistry of Minerals, 37: 465-474.

Zou G, Mao HK, Bell P, Virgo D (1979-1980). High pressure experiments on the iron oxide wüstite ($Fe_{1-x}O$). In: Carnegie Institute of Washington Yearbook. Washington, D.C (39): 374-376.

Appendix

Tables

The following tables summarize results from experiments discussed in Chapter 4 and are organized by composition. Standard strain is defined as $\Delta // l_0 \times 100$, where l_0 is the sample length after quasi-hydrostatic compression. Differential stress is defined as $t = \sigma_{33} - \sigma_{11}$, where σ_{33} is the compressive stress. Pole densities from inverse pole figures (shown in the next section) are given in multiples of a random distribution (m.r.d.) as a measure of degree of crystallographic preferred orientation; minimum pole densities (min m.r.d.) and maximum pole densities (max m.r.d.) are shown. The data shown in these tables corresponds with inverse pole figures with the same Run and #.

100% $NaMgF_3$

Run	#	Load (tons)	P_V(GPa)	T(ºC)	a(Å)	b(Å)	c(Å)	Standard strain %	t(GPa)	min m.r.d	max m.r.d
D1185	1	0	0.0	25	5.3998(1)	5.5172(1)	7.7221(2)	0	0.00726	0.79	1.23
D1185	2	20	0.1	25	5.3973(2)	5.5175(2)	7.7197(3)	0	-0.2778	0.88	1.46
D1185	4	20	4.6	25	5.2617(4)	5.4700(4)	7.5718(6)	2	-1.839	0.01	6.02
D1185	7	20	2.9	400	5.3185(3)	5.4687(3)	7.6314(5)	3	-1.77	0.01	6.24
D1185	9	20	2.9	400	5.3191(3)	5.4663(4)	7.6357(5)	5	-1.731	0.00	6.06
D1185	16	20	3.6	400	5.3024(4)	5.4527(4)	7.6228(6)	16	-2.073	0.00	8.60
D1185	18	20	3.6	400	5.3042(5)	5.4576(4)	7.6121(7)	20	-2.25	0.00	8.56
D1185	20	20	3.6	400	5.2960(5)	5.4565(5)	7.6260(8)	25	-2.151	0.00	8.42
D1185	22	20	3.5	400	5.2993(4)	5.4536(4)	7.6309(6)	31	-2.172	0.00	10.80
D1185	23	20	4.3	25	5.2803(4)	5.4419(5)	7.6057(6)	31	-2.046	0.00	11.81
D1185	63	20	4.2	25	5.2824(4)	5.4412(4)	7.6096(6)	32	-1.899	0.00	11.84
D1185	64	9	3.0	25	5.2941(4)	5.4867(5)	7.6316(6)	34	-2.229	0.00	12.15
D1189	1	0	0	25	5.3935(1)	5.5099(1)	7.7139(2)	0	-0.0252	0.84	1.11
D1189	3	7	1.0	400	5.3655(3)	5.4961(3)	7.6763(4)	0	-1.107	0.02	5.00
D1189	8	20	1.0	800	5.3808(2)	5.4771(2)	7.6788(4)	0	-0.744	0.02	5.03
D1189	11	20	1.6	775	5.3628(3)	5.4677(3)	7.6617(4)	8	-1.02	0.03	5.18
D1189	12	20	1.6	775	5.3625(3)	5.4682(3)	7.6633(4)	15	-1.05	0.03	5.60
D1189	13	20	1.3	775	5.3623(3)	5.4790(2)	7.6714(4)	24	-0.9	0.02	6.94
D1189	41	20	3.1	25	5.3096(1)	5.4542(2)	7.6217(3)	50	*-0.0087*	0.03	6.63
D1189	43	12	2.4	25	5.3168(3)	5.4906(3)	7.6238(4)	28	-1.572	0.03	7.30

85% $NaMgF_3$, 15% NaCl

Run	#	Phase	Load (tons)	$P_{V,T}$(GPa)	T(°C)	a(Å)	b(Å)	c(Å)	Standard strain %	t(GPa)	min m.r.d	max m.r.d
D1476	1	NaCl	0.8	0.0	25	5.5927(2)	-	-	0	0.0105	0.72	1.31
		$NaMgF_3$				5.3173(2)	5.4388(2)	7.6051(3)		-0.0243	0.77	1.18
D1476	4	NaCl	18	2.8	25	5.4236(1)	-	-	0	-0.0333	0.64	1.35
		$NaMgF_3$				5.2089(3)	5.4163(4)	7.5031(6)		-0.21	0.61	2.03
D1476	5	NaCl	20	3.0	200	5.4238(1)	-	-	3	-0.177	0.73	1.21
		$NaMgF_3$				5.2365(3)	5.4086(3)	7.5200(5)		-0.738	0.31	2.37
D1476	6	NaCl	20	3.7	200	5.3852(2)	-	-	7	-0.2562	0.40	1.37
		$NaMgF_3$				5.2220(3)	5.3841(3)	7.5023(5)		-1.254	0.10	4.51
D1476	7	NaCl	20	4.4	200	5.3539(2)	-	-	13	-0.231	0.23	1.44
		$NaMgF_3$				5.2067(4)	5.3777(4)	7.4891(6)		-1.548	0.05	5.89
D1476	8	NaCl	20	4.8	200	5.3366(2)	-	-	17	-0.096	0.42	1.41
		$NaMgF_3$				5.1990(4)	5.3770(4)	7.4886(7)		-1.737	0.08	5.62
D1476	9	NaCl	20	5.0	200	5.3306(2)	-	-	24	-0.237	0.40	1.35
		$NaMgF_3$				5.1944(4)	5.3831(4)	7.4715(7)		-1.866	0.04	5.33
D1476	10	NaCl	20	5.1	200	5.3241(2)	-	-	30	-0.201	0.40	1.46
		$NaMgF_3$				5.1889(4)	5.3837(5)	7.4756(7)		-1.896	0.05	5.04
D1476	11	NaCl	20	5.3	200	5.3157(3)	-	-	36	-0.057	0.35	1.49
		$NaMgF_3$				5.1952(6)	5.3797(6)	7.482(1)		-1.959	0.05	4.97
D1476	12	NaCl	20	4.0	400	5.3784(2)	-	-	43	-0.12	0.55	1.39
		$NaMgF_3$				5.2455(3)	5.3854(3)	7.5305(5)		-1.281	0.07	4.21
D1476	13	NaCl	20	2.9	600	5.47432(9)	-	-	51	-0.0285	0.74	1.23
		$NaMgF_3$				5.3216(2)	5.4116(2)	7.6010(3)		-0.3624	0.08	4.11

85% $NaMgF_3$, 15% NaCl

Run	#	Phase	Load (tons)	$P_{V,T}$(GPa)	T(°C)	a(Å)	b(Å)	c(Å)	Standard strain %	t(GPa)	min m.r.d	max m.r.d
D1475	1	NaCl	0	0.0	25	5.6352(1)	-	-	0	-0.0021	0.66	1.29
		$NaMgF_3$				5.3576(1)	5.4798(2)	7.6625(2)		-0.0033	0.79	1.30
D1475	5	NaCl	20	3.3	25	5.4386(1)	-	-	0	-0.1122	0.87	1.12
		$NaMgF_3$				5.2362(3)	5.4319(3)	7.5458(5)		-0.516	0.32	3.12
D1475	6	NaCl	20	3.1	400	5.4748(1)	-	-	2	-0.1014	0.66	1.32
		$NaMgF_3$				5.3076(2)	5.4306(2)	7.6049(3)		-0.849	0.07	4.10
D1475	7	NaCl	20	3.3	400	5.46255(9)	-	-	5	-0.129	0.55	1.32
		$NaMgF_3$				5.3009(2)	5.4265(2)	7.5957(3)		-0.954	0.07	4.51
D1475	8	NaCl	20	3.9	400	5.4253(1)	-	-	12	-0.1683	0.46	1.49
		$NaMgF_3$				5.2828(2)	5.4134(2)	7.5764(4)		-1.137	0.03	5.40
D1475	9	NaCl	20	4.1	400	5.4117(1)	-	-	25	-0.1371	0.52	1.33
		$NaMgF_3$				5.2777(2)	5.4108(3)	7.5695(4)		-1.152	0.04	5.18
D1475	10	NaCl	20	4.4	400	5.3998(2)	-	-	29	-0.189	0.49	1.23
		$NaMgF_3$				5.2690(3)	5.4090(3)	7.5614(4)		-1.317	0.06	4.65
D1475	11	NaCl	20	4.4	400	5.3957(2)	-	-	34	-0.1848	0.53	1.28
		$NaMgF_3$				5.2681(2)	5.4085(3)	7.5588(4)		-1.347	0.07	4.62
D1475	12	NaCl	20	4.5	400	5.3937(2)	-	-	41	-0.1872	0.59	1.34
		$NaMgF_3$				5.2658(2)	5.4068(3)	7.5596(4)		-1.29	0.03	4.94
D1475	13	NaCl	20	4.6	25	5.3857(1)	-	-	44	-0.1611	0.54	1.33
		$NaMgF_3$				5.2442(2)	5.3983(3)	7.5343(4)		-1.209	0.04	4.86

80% $NaMgF_3$, 20% NaCl

Run	#	Phase	Load (tons)	$P_{V,T}$(GPa)	T(ºC)	a(Å)	b(Å)	c(Å)	Standard strain %	t(GPa)	min m.r.d	max m.r.d
D1313	1	NaCl	0	0.0	25	5.6319(1)	-	-	0	0.0033	0.83	1.19
		$NaMgF_3$				5.3524(3)	5.4760(3)	7.6560(5)		-0.051	0.88	1.14
D1313	3	NaCl	20	4.4	25	5.3911(1)	-	-	1	-0.1776	0.72	1.27
		$NaMgF_3$				5.2142(3)	5.4303(4)	7.5158(5)		-1.392	0.03	5.08
D1313	8	NaCl	20	5.3	25	5.3562(2)	-	-	7	-0.147	0.72	1.17
		$NaMgF_3$				5.1975(4)	5.4215(4)	7.5046(7)		-1.488	0.09	4.92
D1313	12	NaCl	20	4.9	200	5.3723(2)	-	-	19	-0.138	0.71	1.21
		$NaMgF_3$				5.2251(4)	5.4171(4)	7.5385(7)		-1.371	0.22	4.19
D1313	13	NaCl	20	4.0	400	5.4155(1)	-	-	20	-0.0831	0.75	1.19
		$NaMgF_3$				5.2776(3)	5.4190(3)	7.5717(6)		-1.068	0.04	5.26
D1313	14	NaCl	20	3.6	600	5.4628(1)	-	-	26	-0.0525	0.71	1.35
		$NaMgF_3$				5.3155(2)	5.4285(2)	7.6082(4)		-0.474	0.06	4.61
D1313	18	NaCl	20	2.9	100	5.4627(1)	-	-	24	-0.0531	0.78	1.21
		$NaMgF_3$				5.3149(3)	5.4281(3)	7.6096(5)		-0.4812	0.06	4.85
D1313	21	NaCl	20	2.0	25	5.49983(9)	-	-	25	-0.1368	0.73	1.21
		$NaMgF_3$				5.3023(2)	5.4279(2)	7.5910(3)		-0.468	0.18	4.61
D1313	22	NaCl	20	2.3	200	5.5040(1)	-	-	25	-0.1224	0.71	1.19
		$NaMgF_3$				5.3134(2)	5.4307(2)	7.6029(3)		-0.501	0.18	4.66
D1313	23	NaCl	20	2.6	400	5.50544(9)	-	-	25	-0.0315	0.70	1.16
		$NaMgF_3$				5.3273(2)	5.4349(2)	7.6176(3)		-0.465	0.15	4.54
D1313	24	NaCl	20	3.0	600	5.50629(8)	-	-	26	-0.0153	0.69	1.19
		$NaMgF_3$				5.3400(2)	5.4380(2)	7.6309(3)		-0.273	0.06	4.56

75% $NaMgF_3$, 25% NaCl

Run	#	Phase	Load (tons)	$P_{V,T}$(GPa)	T(°C)	a(Å)	b(Å)	c(Å)	Standard strain %	t (GPa)	min m.r.d	max m.r.d
D1187	1	NaCl	0	0.0	25	5.64757(7)	-	-	0	0.003	0.81	1.24
		$NaMgF_3$				5.3672(2)	5.4872(2)	7.6764(3)		-0.035	0.76	1.26
D1187	3	NaCl	3.6	0.0	25	5.64394(7)	-	-	0	-0.002	0.82	1.23
		$NaMgF_3$				5.3616(2)	5.4908(2)	7.6768(3)		-0.119	0.32	3.68
D1187	5	NaCl	7.5	1.4	25	5.5514(1)	-	-	0	-0.078	0.88	1.30
		$NaMgF_3$				5.3110(2)	5.4809(3)	7.6391(4)		-0.504	0.34	2.33
D1187	6	NaCl	20	3.4	100	5.4508(1)	-	-	0	-0.099	0.89	1.08
		$NaMgF_3$				5.2609(3)	5.4494(4)	7.5730(5)		-0.855	0.20	3.13
D1187	9	NaCl	20	4.4	100	5.4065(1)	-	-	6	-0.194	0.60	1.20
		$NaMgF_3$				5.2341(3)	5.4406(4)	7.5435(6)		-1.308	0.20	3.95
D1187	11	NaCl	20	4.8	100	5.3877(1)	-	-	11	-0.187	0.66	1.21
		$NaMgF_3$				5.2220(4)	5.4381(4)	7.5288(6)		-1.443	0.18	4.38
D1187	12	NaCl	20	5.0	100	5.3822(1)	-	-	14	-0.189	0.58	1.19
		$NaMgF_3$				5.2175(4)	5.4370(4)	7.5333(6)		-1.458	0.19	4.69
D1187	13	NaCl	20	5.1	100	5.3764(1)	-	-	18	-0.164	0.62	1.16
		$NaMgF_3$				5.2153(4)	5.4374(5)	7.5319(7)		-1.461	0.30	4.25
D1187	15	NaCl	20	5.2	100	5.3738(1)	-	-	27	-0.14	0.72	1.15
		$NaMgF_3$				5.2141(4)	5.4363(5)	7.5371(7)		-1.437	0.24	4.37
D1187	37	NaCl	20	5.2	100	5.3737(2)	-	-	30	-0.153	0.81	1.13
		$NaMgF_3$				5.2147(5)	5.4399(5)	7.5274(8)		-1.446	0.26	3.89
D1187	51	NaCl	20	5.2	25	5.3718(2)	-	-	32	-0.094	0.81	1.11
		$NaMgF_3$				5.2093(5)	5.4400(6)	7.5324(9)		-1.434	0.25	3.65
D1187	53	NaCl	5	2.0	25	5.5186(1)	-	-	36	-0.072	0.78	1.18
		$NaMgF_3$				5.2946(3)	5.4879(5)	7.6367(6)		-0.93	0.17	3.82

75% $NaMgF_3$, 25% NaCl

Run	#	Phase	Load (tons)	$P_{V,T}$(GPa)	T(°C)	a(Å)	b(Å)	c(Å)	Standard strain %	t(GPa)	min m.r.d	max m.r.d
D1188	1	NaCl	0	0	25	5.66849(8)	-	-	0	-0.005	0.75	1.42
		$NaMgF_3$				5.3871(2)	5.5084(2)	7.7061(3)		-0.099	0.75	1.31
D1188	2	NaCl	5	0.8	25	5.6086(1)	-	-	0	-0.067	0.86	1.19
		$NaMgF_3$	-		-	5.3471(3)	5.5051(3)	7.6758(4)		-0.747	0.08	4.12
D1188	4	NaCl	20	3.1	400	5.5067(1)	-	-	0	-0.050	0.76	1.13
		$NaMgF_3$	-		-	5.3202(4)	5.4739(5)	7.6395(7)		-0.657	0.15	3.92
D1188	9	NaCl	20	3.6	400	5.4729(1)	-	-	6	-0.113	0.77	1.18
		$NaMgF_3$	-			5.3021(3)	5.4653(5)	7.6262(6)		-1.080	0.14	4.24
D1188	12	NaCl	20	3.9	400	5.4582(1)	-	-	10	-0.121	0.84	1.11
		$NaMgF_3$	-		-	5.2963(4)	5.4634(5)	7.6153(7)		-1.185	0.20	4.05
D1188	15	NaCl	20	4.0	400	5.4494(1)	-	-	16	-0.125	0.89	1.12
		$NaMgF_3$	-		-	5.2916(1)	5.4634(6)	7.6115(8)		-1.239	0.18	3.81
D1188	18	NaCl	20	4.0	400	5.4495(2)	-	-	20	-0.104	0.76	1.14
		$NaMgF_3$	-		-	5.2883(5)	5.4635(6)	7.6181(9)		-1.227	0.19	4.09
D1188	20	NaCl	20	4.1	25	5.4380(1)	-	-	23	-0.031	0.95	1.09
		$NaMgF_3$	-		-	5.2718(4)	5.4597(5)	7.5886(7)		-1.089	0.23	3.67
D1188	22	NaCl	8	2.9	25	5.4892(2)	-	-	24	-0.104	0.86	1.13
		$NaMgF_3$	-		-	5.2868(4)	5.4883(6)	7.6322(8)		-1.242	0.17	4.00

50% $NaMgF_3$, 50% NaCl

Run	#	Phase	Load (tons)	$P_{V,T}$(GPa)	T(ºC)	a(Å)	b(Å)	c(Å)	Standard strain %	t(GPa)	min m.r.d	max m.r.d
D1244	1	NaCl	0	0.0	25	5.78195(8)	-	-	0	0.001	0.88	1.09
		$NaMgF_3$				5.4946(4)	5.6223(4)	7.8615(7)		-0.087	0.73	1.47
D1244	2	NaCl	20	3.5	200	5.58057(9)	-	-	-5	-0.149	0.66	1.56
		$NaMgF_3$				5.3890(5)	5.5609(7)	7.7457(9)		-0.444	0.58	1.89
D1244	6	NaCl	20	3.6	200	5.57448(8)	-	-	0	-0.145	0.72	1.40
		$NaMgF_3$				5.3986(5)	5.5534(5)	7.7567(7)		-0.63	0.13	4.04
D1244	14	NaCl	20	4.2	200	5.54761(8)	-	-	7	-0.147	0.90	1.21
		$NaMgF_3$				5.3806(5)	5.5762(6)	7.7330(8)		-0.813	0.33	4.05
D1244	21	NaCl	20	4.3	200	5.53951(8)	-	-	23	-0.152	0.91	1.10
		$NaMgF_3$				5.3753(5)	5.5787(6)	7.7247(8)		-0.858	0.33	2.99
D1244	23	NaCl	20	4.3	200	5.54299(9)	-	-	28	-0.155	0.87	1.11
		$NaMgF_3$				5.3825(5)	5.5795(7)	7.730(1)		-0.879	0.29	2.80
D1244	27	NaCl	20	4.1	200	5.54980(8)	-	-	39	-0.145	0.91	1.10
		$NaMgF_3$				5.3855(5)	5.5802(6)	7.7387(9)		-0.888	0.30	3.03
D1244	32	NaCl	20	3.9	200	5.56010(8)	-	-	50	-0.127	0.94	1.11
		$NaMgF_3$				5.3946(6)	5.5856(7)	7.745(1)		-0.867	0.36	2.78

50% $NaMgF_3$, 50% NaCl

Run	#	Phase	Load (tons)	$P_{V,T}$(GPa)	T(ºC)	a(Å)	b(Å)	c(Å)	Standard strain %	t(GPa)	min m.r.d	max m.r.d
D1315	1	NaCl	0	0.0	25	5.64613(7)	-	-	0	-0.015	0.80	1.26
		$NaMgF_3$				5.3636(4)	5.4905(4)	7.6806(6)		-0.165	0.44	2.50
D1315	4	NaCl	20	4.8	100	5.38912(7)	-	-	22	-0.1518	0.76	1.09
		$NaMgF_3$				5.2327(5)	5.4368(6)	7.5404(9)		-0.885	0.43	3.38
D1315	5	NaCl	20	4.5	200	5.40228(7)	-	-	23	-0.1299	0.76	1.07
		$NaMgF_3$				5.2464(5)	5.4336(6)	7.5564(9)		-0.744	0.32	3.40
D1315	6	NaCl	20	4.0	400	5.43175(7)	-	-	27	-0.0978	0.80	1.07
		$NaMgF_3$				5.2762(4)	5.4368(5)	7.5876(8)		-0.588	0.33	3.30
D1315	7	NaCl	20	3.7	600	5.47493(5)	-	-	32	-0.0429	0.74	1.22
		$NaMgF_3$				5.3178(3)	5.4374(3)	7.6261(5)		-0.108	0.20	3.25
D1315	10	NaCl	20	3.1	25	5.45841(5)	-	-	33	0.024	0.71	1.15
		$NaMgF_3$				5.2867(3)	5.4316(5)	7.5842(7)		-0.129	0.36	3.09
D1315	11	NaCl	20	3.2	200	5.46261(5)	-	-	33	0.0186	0.76	1.24
		$NaMgF_3$				5.2926(3)	5.4304(4)	7.5951(6)		-0.0309	0.29	2.94
D1315	12	NaCl	20	3.3	400	5.46790(5)	-	-	33	-0.0216	0.74	1.14
		$NaMgF_3$				5.3045(3)	5.4335(4)	7.6083(6)		-0.072	0.29	2.94
D1315	13	NaCl	20	3.7	600	5.47295(5)	-	-	33	-0.045	0.74	1.14
		$NaMgF_3$				5.3174(3)	5.4398(4)	7.6198(6)		-0.168	0.35	3.31
D1315	14	NaCl	16	3.0	25	5.46640(6)	-	-	32	0.0471	0.80	1.09
		$NaMgF_3$				5.2844(4)	5.4307(4)	7.5894(6)		0.234	0.61	1.91

30% $NaMgF_3$, 70% NaCl

Run	#	Phase	Load (tons)	$P_{V,T}$(GPa)	T(ºC)	a(Å)	b(Å)	c(Å)	Standard strain %	t(GPa)	min m.r.d	max m.r.d
D1243	4	NaCl	0	0.0	25	5.77275(7)	-	-	0	-0.00024	0.66	1.26
		$NaMgF_3$				5.4862(8)	5.6176(9)	7.851(1)		-0.0159	0.48	1.55
D1243	7	NaCl	20	3.4	200	5.57587(7)	-	-	-8	-1.1808	0.59	2.65
		$NaMgF_3$				5.395(1)	5.541(1)	7.730(2)		-0.642	0.32	1.72
D1243	11	NaCl	20	4.3	200	5.53253(6)	-	-	1	-0.1608	0.78	1.34
		$NaMgF_3$				5.3815(9)	5.552(1)	7.693(2)		-0.984	0.10	4.74
D1243	15	NaCl	20	4.9	200	5.50624(6)	-	-	19	-0.1929	0.70	1.31
		$NaMgF_3$				5.3599(8)	5.536(1)	7.674(1)		-0.825	0.32	3.37
D1243	19	NaCl	20	5.1	200	5.49531(6)	-	-	34	-0.1761	0.68	1.29
		$NaMgF_3$				5.3521(9)	5.541(1)	7.670(2)		-0.693	0.24	2.28
D1243	23	NaCl	20	5.1	25	5.49800(6)	-	-	44	-0.1293	0.80	1.14
		$NaMgF_3$				5.3416(8)	5.535(1)	7.667(1)		-0.54	0.24	3.09

30% $NaMgF_3$, 70% NaCl

Run	#	Phase	Load (tons)	$P_{V,T}$(GPa)	T(ºC)	a(Å)	b(Å)	c(Å)	Standard strain %	t(GPa)	min m.r.d	max m.r.d
D1316	1	NaCl	0	0.0	25	5.62357(6)	-	-	0	-0.0615	0.90	1.13
		$NaMgF_3$				5.3470(6)	5.4751(7)	7.650(1)		-0.183	0.73	1.45
D1316	4	NaCl	20	3.9	25	5.40454(6)	-	-	0	-0.144	0.58	1.41
		$NaMgF_3$				5.243(1)	5.420(1)	7.531(2)		-0.672	0.32	3.61
D1316	5	NaCl	20	5.6	25	5.33644(5)	-	-	21	-0.1728	0.51	1.26
		$NaMgF_3$				5.1969(8)	5.398(1)	7.480(1)		-0.609	0.39	2.52
D1316	6	NaCl	20	5.1	200	5.35287(5)	-	-	26	-0.1551	0.51	1.27
		$NaMgF_3$				5.2197(8)	5.3987(9)	7.502(1)		-0.612	0.34	2.84
D1316	7	NaCl	20	4.4	400	5.38453(5)	-	-	29	-0.126	0.52	1.31
		$NaMgF_3$				5.2563(8)	5.4058(9)	7.539(1)		-0.534	0.30	3.09
D1316	8	NaCl	20	4.1	600	5.42540(5)	-	-	32	-0.0477	0.57	1.24
		$NaMgF_3$				5.2928(7)	5.4118(9)	7.572(1)		-0.174	0.21	3.12
D1316	11	NaCl	20	3.8	100	5.41004(5)	-	-	34	0.0129	0.59	1.32
		$NaMgF_3$				5.2547(6)	5.4015(9)	7.533(1)		-0.039	0.27	2.84
D1316	12	NaCl	20	3.8	200	5.41328(5)	-	-	34	-0.00066	0.64	1.55
		$NaMgF_3$				5.2631(7)	5.403(1)	7.540(1)		-0.045	0.25	2.97
D1316	13	NaCl	20	3.8	400	5.41796(6)	-	-	34	-0.0504	0.42	1.36
		$NaMgF_3$				5.2773(8)	5.408(1)	7.555(1)		-0.213	0.21	2.98
D1316	14	NaCl	20	4.1	600	5.42418(6)	-	-	34	-0.0468	0.46	1.24
		$NaMgF_3$				5.2962(8)	5.4084(8)	7.561(1)		-0.198	0.31	2.62

25% $NaMgF_3$, 75% NaCl

Run	#	Phase	Load (tons)	$P_{V,T}$(GPa)	T(ºC)	a(Å)	b(Å)	c(Å)	Standard strain %	t(GPa)	min m.r.d	max m.r.d
D1186	3	NaCl	0	0.0	25	5.67312(5)	-	-	0	0.0018	0.83	1.30
		$NaMgF_3$				5.3903(6)	5.5150(7)	7.711(1)		-0.03	0.82	1.25
D1186	5	NaCl	7	1.2	25	5.59000(4)	-	-	-22	-0.0264	0.51	2.19
		$NaMgF_3$				5.3503(6)	5.4954(5)	7.6710(9)		-0.03	0.38	3.18
D1186	8	NaCl	20	3.7	400	5.47125(5)	-	-	-11	-0.1206	0.54	2.44
		$NaMgF_3$				5.2892(7)	5.4502(9)	7.616(1)		-0.246	0.33	2.05
D1186	12	NaCl	20	3.2	400	5.50200(6)	-	-	-2	-0.0753	0.66	1.77
		$NaMgF_3$				5.3193(8)	5.480(1)	7.665(1)		-0.258	0.44	1.93
D1186	14	NaCl	20	3.0	400	5.51867(5)	-	-	2	-0.0447	0.59	2.01
		$NaMgF_3$				5.3402(6)	5.4729(8)	7.6645(9)		-0.141	0.10	2.53
D1186	16	NaCl	20	3.2	400	5.50431(4)	-	-	5	-0.057	0.70	1.46
		$NaMgF_3$	-			5.3328(5)	5.4655(7)	7.6577(8)		-0.195	0.28	2.58
D1186	18	NaCl	20	3.4	400	5.4936(4)	-	-	11	-0.06	0.83	1.28
		$NaMgF_3$	-			5.3273(5)	5.4590(6)	7.6536(7)		-0.177	0.29	2.51
D1186	23	NaCl	20	3.3	400	5.4939(4)	-	-	26	-0.0654	0.94	1.07
		$NaMgF_3$				5.3237(5)	5.4621(6)	7.6509(7)		-0.15	0.27	2.82
D1186	24	NaCl	20	3.3	400	5.49600(5)	-	-	30	-0.0609	0.84	1.25
		$NaMgF_3$				5.3202(4)	5.4657(7)	7.6498(8)		-0.00018	0.11	3.29
D1186	28	NaCl	1	0.2	25	5.66062(5)	-	-	53	0.0945	0.77	1.42
		$NaMgF_3$				5.3807(5)	5.5154(6)	7.7087(8)		0.165	0.58	1.65

Figures

The following inverse pole figures (IPFs) show texture development as strain was increase in $NaMgF_3$ and NaCl during deformation experiments described and discussed in Chapter 4. Crystallographic preferred orientation is represented in IPFs by plotting the compression direction relative to crystallographic planes. The density of poles to planes in a given orientation are indicated with color as multiples of random distribution (m.r.d.). An m.r.d. = 1 (light blue) denotes random orientation. All IPFs for $NaMgF_3$ are plotted with a scale from 0 to 4.9 m.r.d., and all IPFs for NaCl are plotted with a scale from 0.5 to 1.9 m.r.d. These IPFs are equal area projections.

100% $NaMgF_3$

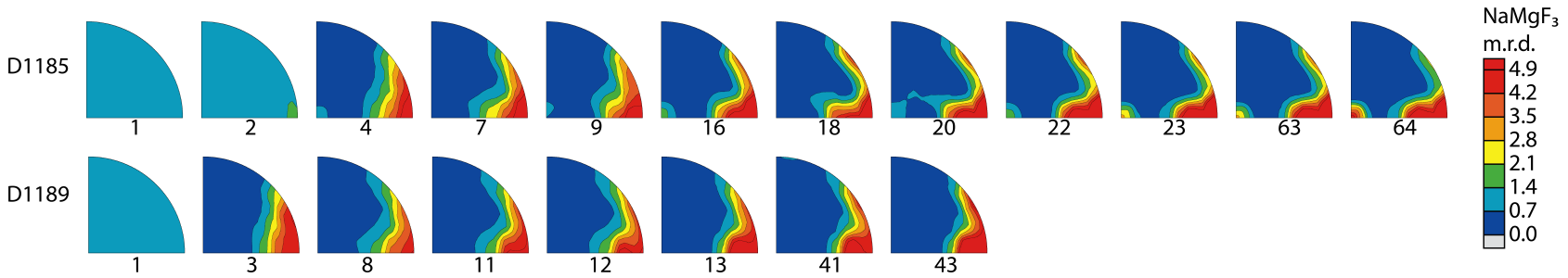

85% $NaMgF_3$, 15% NaCl

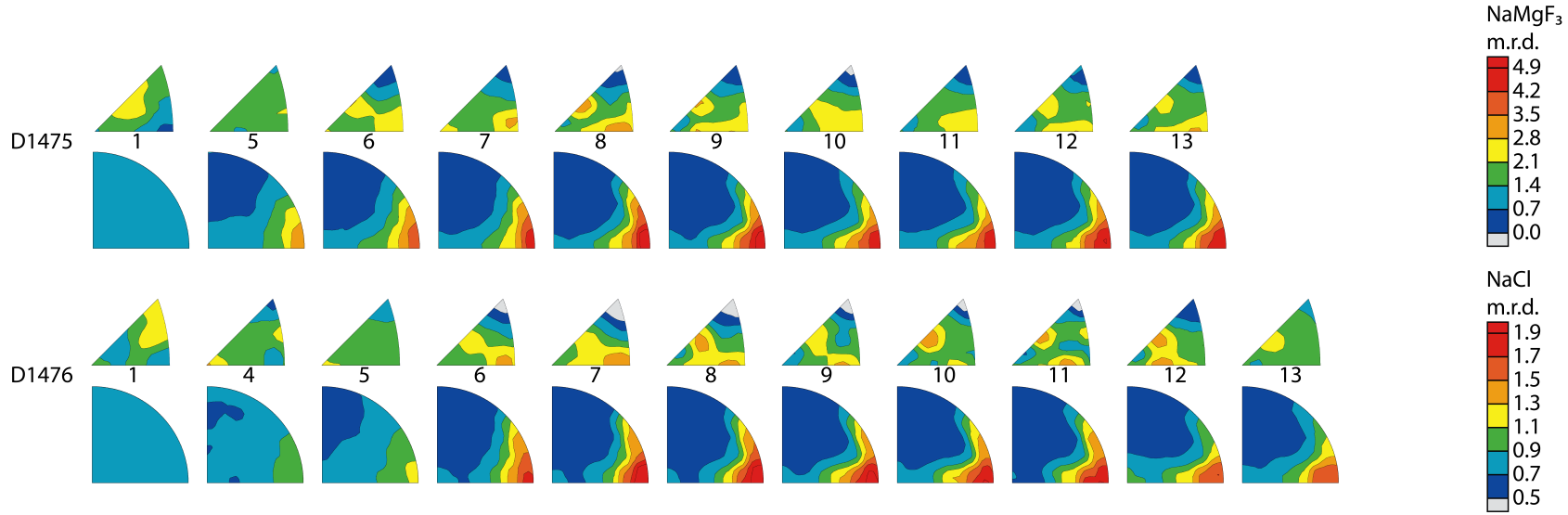

80% $NaMgF_3$, 20% NaCl

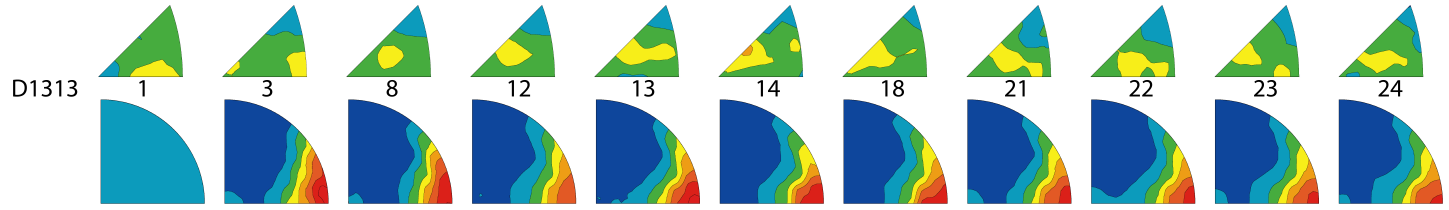

75% $NaMgF_3$, 25% NaCl

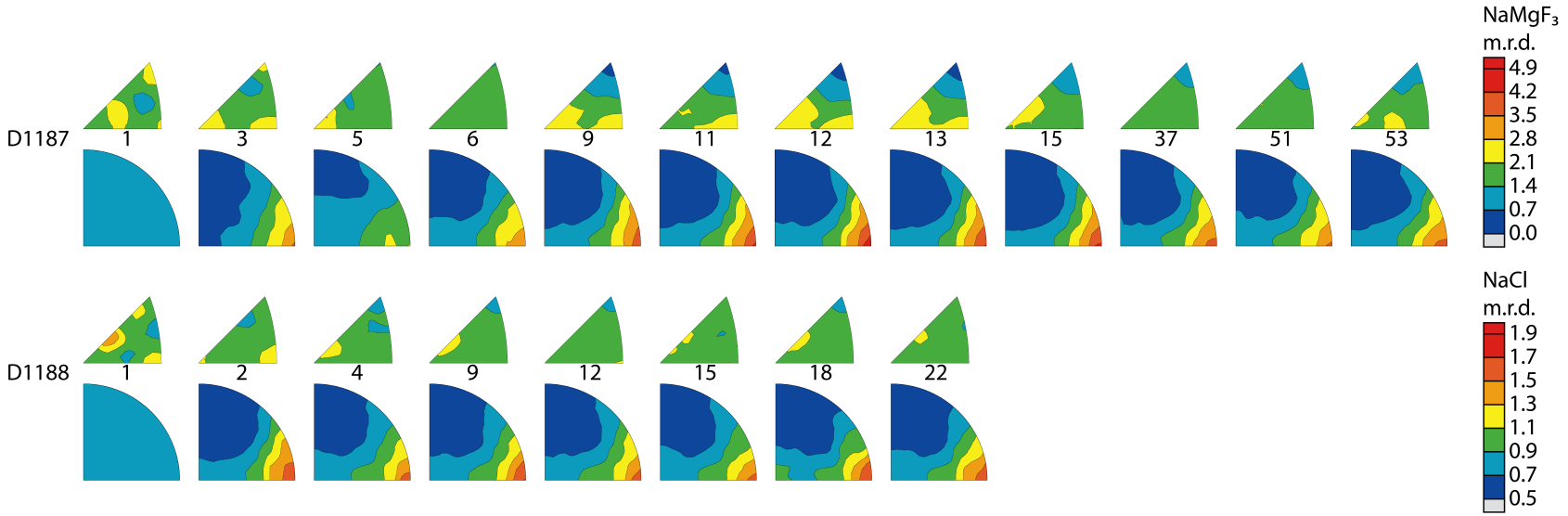

50% $NaMgF_3$, 50% NaCl

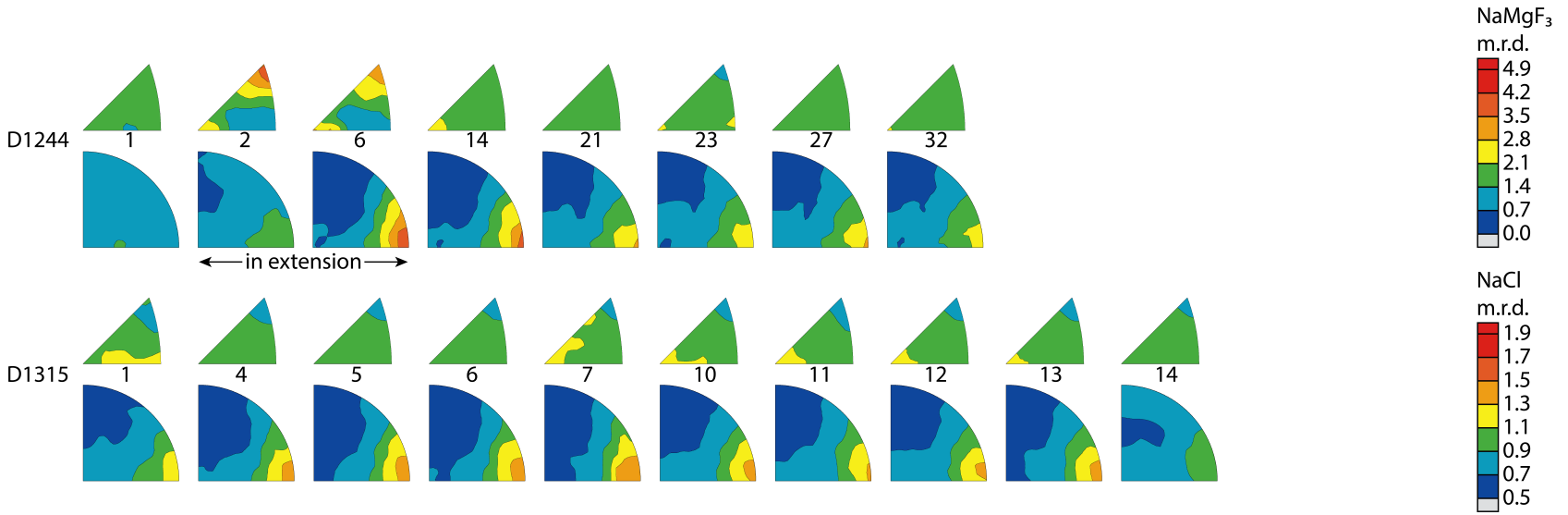

30% $NaMgF_3$, 70% NaCl

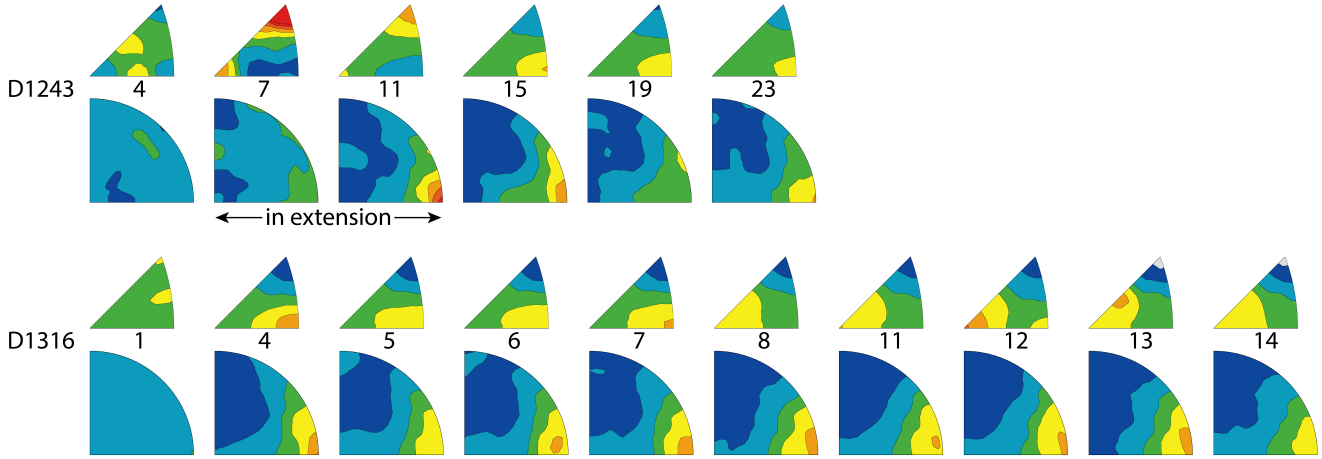

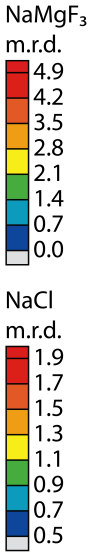

25% $NaMgF_3$, 75% NaCl